ANNEALING BEHAVIOR OF HEAVILY COLD DEFORMED, EQUIATOMIC, FERROMAGNETIC Fe-Pd INTERMETALLICS

by

Anirudha R. Deshpande

BE, University of Pune, 1999

MS, University of Pittsburgh, 2004

Submitted to the Graduate Faculty of

School of Engineering in partial fulfillment

of the requirements for the degree of

Doctor of Philosophy

University of Pittsburgh

2005

UNIVERSITY OF PITTSBURGH

SCHOOL OF ENGINEERING

This dissertation was presented

by

Anirudha R. Deshpande

It was defended on

October 20, 2005

and approved by

Dr. John A. Barnard, Professor, Department of Materials Science and Engineering

Dr. Judith C. Yang, Associate Professor, Department of Materials Science and Engineering

Dr. S. Mao, Professor, Department of Mechanical Engineering

Dr. David E. Laughlin, Professor, Department of Materials Science and Engineering

Dr. Timothy J. Klemmer, Research Scientist, Seagate Technology

Dr. J.M.K. Wiezorek, Associate Professor, Department of Materials Science and Engineering
Dissertation Director

ANNEALING BEHAVIOR OF HEAVILY COLD DEFORMED, EQUIATOMIC, FERROMAGNETIC Fe-Pd INTERMETALLICS

Anirudha R. Deshpande, PhD

University of Pittsburgh, 2005

Reversibly ordering Fe-Pd intermetallics for equiatomic composition exhibit high temperature stable, disordered FCC phase and low temperature ($< T_c$) stable $L1_0$-ordered phase. In this system FCC to $L1_0$ ordering phase transformation has been associated with development of lamellar microstructural morphology known as 'polytwin' microstructure. Previously polytwin microstructure has been replaced by equiaxed grained morphology of $L1_0$-ordered phase that exhibits enhanced magnetic properties. A combined reaction (CR) of FCC to $L1_0$ ordering phase transformation concomitant with annealing of defects introduced in metastable FCC phase has been utilized to attain equiaxed grained $L1_0$-ordered microstructure. Such CR have also been utilized in other systems that undergo an ordering phase transformation. With exception of some studies, most of these prior investigations have utilized framework of conventional annealing (recovery, recrystallization and grain growth) that has been developed for disordered dilute solid solutions that do not undergo an ordering phase transformation (e.g. annealing of Cu), to understand evolution of microstructure during CR. A clear distinction between conventional annealing (cold deformation of ordered alloy followed by recovery, recrystallization and grain growth in ordered deformed matrix) and combined reaction (an ordering phase transformation concomitant with annealing of defects introduced in disordered parent phase) has not been realized. Creation of a clear distinction between both of these modes of transformation in model

Fe-Pd system is the main motivation of this study. Disordered FCC parent phase (prior to CR) and $L1_0$-ordered phase (prior to conventional annealing) have been deformed by cold rolling to comparable % reduction in thickness. Both of these annealing transformations have been conducted at same temperature. The microstructural mechanisms that lead to generation of equiaxed grained microstructures of $L1_0$-ordered phase in both of these transformations have been investigated. Vital differences in these transformations such as prior cold deformed state, texture evolution during transformation, kinetics of transformation etc. have been recognized. Similarities in these transformations such as mechanisms for crystal defects formation, texture evolution during grain growth have also been identified. Existing theories and modifications thereof have been used to rationalize observed similarities and differences between both of these modes of transformation.

TABLE OF CONTENTS

LIST OF FIGURES

PREFACE

There are multiple people who need to be thanked for helping me with this endeavor. Firstly I would like to thank Dr. Wiezorek, for providing me with this wonderful opportunity to pursue my interest in this field. He has been a great mentor and I think myself to be fortunate to have found such a great advisor. I would also like to thank the National Science Foundation for providing funding for this research program. The help provided by Dr. Huiping Xu with initial TEM and SEM experiments is greatly appreciated. I would also like to thank Cole van Ormer and Al Stewart for their help with various microcharacterization techniques. I would also like to thank members from BAMPRI (Dr. Hua, Dr. Cho, Wen Gao) for allowing me to use their experimental equipments. The Pitt-MSE graduate students all provided invaluable help over years and I thank them all. I would also like to express my gratitude to Dr. Soffa, for he has been a great teacher and has helped me develop a sound theoretical base. I would also like to thank Dr. J.R. Blachere for his insight and help with regards to texture analysis part of this project. I would also like to express my gratitude to my committee members, Dr. Barnard, Dr. Yang, Dr. Laughlin, Dr. Klemmer and Dr. Mao for taking time off their busy schedules to attend my thesis defense. Finally I would like to thank my family, friends and especially my parents for stoically bearing the long separation and supporting me all along in this rather arduous but intellectually extremely satisfying experience.

1.0 INTRODUCTION

Processing of metallic materials using cold deformation and heat-treatment, such as annealing, has been critical to the development of many applications that form the backbone of the modern industrialized society. Cold deformation changes the microstructure of the material and affects its physical properties. Such changes are desirable in many instances but can also lead to development of a detrimental microstructural state. The microstructural state in the cold deformed condition consists of a non-equilibrium fraction of crystal defects, such as point defects, dislocations, deformation twins etc. The presence of these crystal defects can affect properties and can significantly reduce or enhance the technological value of a metallic material. Annealing is a heat treatment following deformation processing, which induces solid state process that can be used to eliminate the non-equilibrium content of crystal defects introduced during cold deformation. It is a thermally activated microstructural transformation process that leads to the generation of a microstructure consisting of relatively stress free, new grains of potentially different scale morphology and texture as compared to prior to annealing. The process of annealing comprises of three distinguishable stages of solid state transformation phenomena, namely recovery, recrystallization and grain growth. The combination of cold work and annealing can be used to a) break down the solidification microstructure, b) refine the grain size and c) establish / change or eliminate textures. These phenomena associated with cold

working and annealing have been systematically studied in metallic systems and are fairly well understood for dilute solid solutions of elemental metals and common commercial alloys.

Intermetallics form an interesting class of materials. Members of this class of metallic materials exhibit properties, such as good creep resistance, good magnetic / electrical / optical behavior, and have significant technological value. Similar to other metallic materials the processing of intermetallics also often requires cold deformation. The cold deformation of intermetallics is known to alter their microstructure and hence properties. The effect of cold deformation and subsequent annealing on microstructure and properties in intermetallics is more involved as compared to the more conventional metallic systems. The chemically ordered structure possessed by intermetallic compounds and alloys is partly responsible for the increased complexity relative to their disordered crystalline counterparts. Given this complexity, insufficient systematic understanding of the annealing of cold deformed, ordered intermetallics has been developed to date.

While some ordered intermetallic systems form congruently upon freezing from the melt, many of these systems are in a chemically disordered solid crystalline state at a temperature higher than the critical ordering temperature. These latter systems are referred to as reversibly ordering systems. Often the high temperature disordered state in reversibly ordering intermetallic systems can be preserved at room temperature by sufficiently rapid quenching and can be cold deformed. For annealing temperatures T smaller than the ordering temperature T_c, the ensuing annealing process after this cold deformation in disordered condition involves a disorder → order phase transformation and the annealing of the defects associated with prior cold deformation (e.g. recovery, recrystallization and grain growth). Alternatively, the ordered phase can be cold deformed and the ensuing annealing induced processes involve only the annihilation of excess

crystal defects from the cold deformation to produce new recrystallized ordered grains. The solid state transformation during annealing at $T < T_c$ after cold-deformation of the disordered solid solution is a combined reaction (CR) of ordering phase transformation and annealing. The solid state transformation after cold deformation in the ordered state is a conventional annealing process. Prior studies have been cognizant of this difference in the microstructural transformations. However, systematic understanding of the similarities and differences between both of these modes of microstructural transformation have been lacking. Hence, one of the main aims of this study is to address the paucity of systematic knowledge of the annealing behavior of cold-deformed intermetallics by using a suitable binary model system.

The reversibly ordering[1] model system of interest in this study is the binary Fe-Pd system. The relevant section of the binary phase diagram for this system is shown in figure 1.1[2]

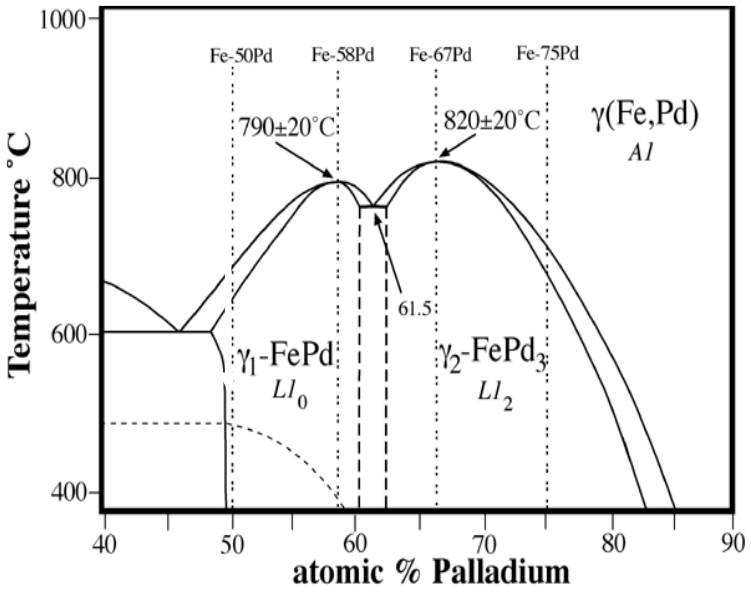

Figure – 1.1 Relevant section for the binary Fe-Pd phase diagram

The alloy with an equiatomic composition is the focus of this study. It exhibits a FCC (γ) phase as the high temperature stable phase, whereas the tetragonal $L1_0$-ordered (γ_1) phase is the stable phase at temperatures lower than 647°C ($T_c \approx 920$ K). The equiatomic composition has been chosen as the phase diagram shows a single phase field (γ_1) for this particular composition at temperatures lower than T_c. Three other compositions of FePd systems are shown in figure-1.1, namely 58 at% Pd, 67at% Pd and 75 at% Pd. The FePd systems of off-stoichiometric Fe-58at% Pd and Fe-67at%Pd exhibit congruent ordering from the disordered FCC phase to the relevant ordered intermetallic phases, $L1_0$ - ordered γ_1 – FePd and $L1_2$ – ordered γ_2 – $FePd_3$ respectively, at fairly similar temperatures. The stoichiometric AB_3 – compound γ_2 – $FePd_3$ is formed for 75 at% Pd from the FCC phase at a similar temperature as the AB compound. Hence, these compositions are suitable for additional and comprehensive studies of the effects of composition and crystal structure on the annealing of ordered intermetallics using a single binary system. Here, only the equiatomic $L1_0$ – ordering system is studied in detail.

The unit cell of the $L1_0$-ordered structure is shown in figure-1.2. The ordered $L1_0$ phase can be envisaged as a layered structure consisting of alternating stacking of pure Fe and pure Pd planes of the type (002). The equilibrium c/a ratio of this tetragonal unit cell is 0.966. Using this conventional unit cell of the $L1_0$-structure its relationship to the close-packed, face-centered cubic (FCC) structure is apparent.

The ductility of the $L1_0$-ordered and the FCC disordered phases in the Fe-Pd system for the equiatomic composition is adequate to plastically deform these materials to large plastic strain at room temperature and subsequently anneal them. These plastically deformed alloys can then undergo microstructural transformation by either a CR (annealing of the disordered, deformed phase) or conventional annealing (annealing of ordered, deformed phase).

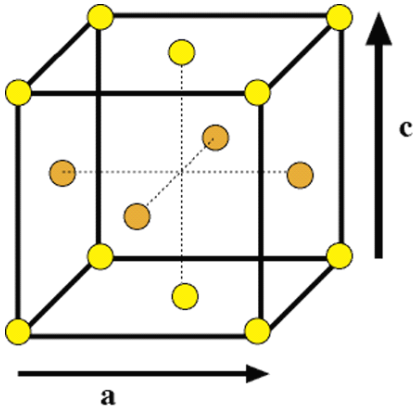

Figure – 1.2 Unit cell of the tetragonal $L1_0$ phase

Thus, the solid state transformations of CR and conventional annealing are accessible to microstructural studies in these alloys. Many other intermetallic systems and especially most other ferromagnetic $L1_0$-ordered intermetallic systems lack room temperature ductility. Therefore, the FePd system forms a suitable model system for the investigation of the evolution of microstructure during annealing in $L1_0$-ordered systems.

γ_1 - FePd intermetallics are an important member of the family of technologically interesting intermetallics, such as CoPt, FePt, TiAl, and MnAl, that can produce the $L1_0$ phase at room temperature. The $L1_0$ phase in the FePd alloys exhibits a high uniaxial magnetocrystalline anisotropy with an 'easy' magnetization axis parallel to [001], a large theoretical B-H product and good corrosion and mechanical properties[3,4]. This combination of properties renders FePd based $L1_0$ intermetallics very attractive for a range of permanent magnet and thin film applications[4] . The technologically interesting properties, such as the magnetic properties, in FePd and other $L1_0$-ordered intermetallics are extremely sensitive to microstructure. The understanding of the

evolution of microstructure during annealing is important to optimize properties of these intermetallics.

Thus, in this study it is intended to develop a detailed understanding of the annealing behavior of cold deformed equiatomic Fe-Pd by systematic comparison of the evolution of the microstructure in the CR mode and the conventional annealing mode. Cold deformation has been achieved using cold rolling. Isothermal annealing heat treatments at temperatures lower than T_c have been conducted to achieve CR transformation and conventional annealing solid state reaction in the deformed, disordered FCC state and deformed, ordered state respectively. The microstructure sensitive property of intrinsic magnetic coercivity, H_c , has been measured in the cold deformed condition and after the annealing treatments. Microstructural evolution during both of these modes of solid state transformations has been studied using a variety of characterization techniques involving X-ray diffraction and electron microscopy. The similarities and disparities between the mechanisms leading to different microstructural states in the solid state reaction during annealing at $T < T_c$ have been highlighted. Moreover, by elucidating the underlying mechanisms active at the microstructural level, this study contributes to the relatively undeveloped field of conventional annealing of cold deformed, ordered intermetallics.

2.0 BACKGROUND

2.1 COMBINED REACTION TRANSFORMATIONS

2.1.1 Introduction

Solid state reactions occur under the influence of thermodynamic driving forces. Reactions, such as recrystallization and diffusional phase transformations, have a characteristic thermodynamic driving force associated with them. In many thermomechanically processed metallic alloy systems more than one driving force and more than one type of solid-state reaction are present, which can strongly affect the microstructural evolution during thermally activated processing[5]. Under such circumstances, it is possible that more than one type of solid state reaction changes the microstructural state of the system. Microstructural rearrangement or transformation facilitated by a process for which the overall driving force is a function of more than one possible elementary solid state reaction are referred to as combined reactions (CR)[6].

CRs are frequently encountered in the field of physical metallurgy. Typical examples are precipitation hardening in cold worked stainless steels and martensitic transformations in shape memory alloys[5]. Recently combined reactions of diffusion controlled precipitation and annealing of cold deformed Al-Zn-Mg and Al-Zn-Mg-Cu alloys have also been investigated[7]. Due to the interplay of the multiple driving forces for the different individual solid state reactions, the kinetics of these CR processes are altered from those of the individual reactions. Possible

synergistic effects can exist amongst the various driving forces. Moreover, due to the different functional dependence of the kinetics of each process on thermal activation, there could be coordinates in temperature-time space for which one reaction could be favored as compared to another. Such scenarios can lead to simultaneous or sequential combined reactions[5]. An important hallmark of a CR is the microstructure that develops as a result of the process. The microstructural development can provide insight regarding the possible mode of combined reaction (e.g. sequential vs. simultaneous) and also about the kinetics of the process[5,6].

2.1.2 Sequential and Simultaneous Combined Reactions

The kinetics of a CR are governed by the tendency of a system to maximize the rate of dissipation of excess free energy. The kinetics of any solid state reaction would be a function of the driving force (for the individual reaction) and the mobility of atoms (in case of diffusion assisted transformations)[8]. Thus depending upon the relative magnitudes of both of these parameters for the elemental processes facilitating the various solid state reactions involved in the interplay during CR transformation, either sequential reactions or simultaneous reactions can occur. While the theoretical framework developed for instance by Hornbogen[5] is useful, most quantitative estimates based on it assume mean field approximations, and therefore may not be suitable to entirely correctly predict the observed transformation behavior. Nevertheless, these treatments provide a useful background for a first approximation theoretical analysis of the possible reaction pathways.

Experimentally derived time-temperature-transformation (TTT) diagrams provide a more accurate description of the system behavior. In temperature-time space, reaction kinetics can be appropriately depicted using a TTT diagram. These diagrams can help us identify the onset and

completion of various reactions that are possible under the influence of appropriate thermodynamic driving forces. As an example, a TTT diagram for a process involving recrystallization (R in the figure) and phase transformation (D in the figure) is shown in figure-2.1[5].

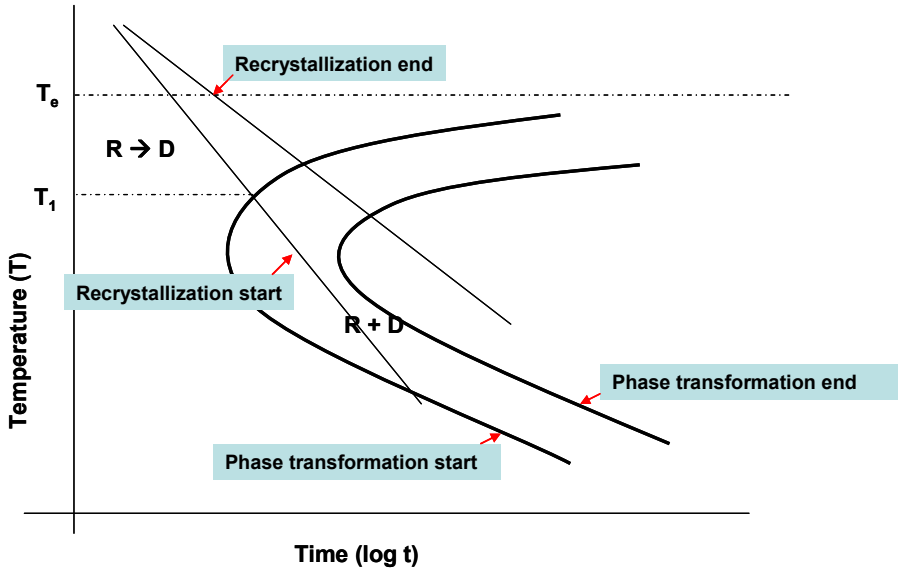

Figure-2.1 A TTT diagram for a process involving recrystallization and phase decomposition.

Figure- 2.1 indicates that the process of recrystallization has faster kinetics for isothermal treatments at temperatures between T_e and T_1. As a result it would precede the phase transformation reaction. Thus for temperature in that range a sequential CR would produce a microstructure where phase transformation would be observed within stress free recrystallized grains. At temperatures lower than T_1 the kinetics for both reactions are comparable. This would lead to a reaction where the phase transformation and recrystallization are occurring simultaneously due to a combined driving force of larger magnitude than for the individual reactions. The microstructure produced in this simultaneous mode of CR would presumably

consist of phase transformation traversing multiple grains that undergo recrystallization at the same instance.

Sequential and simultaneous CRs are predicted to produce morphologically different microstructures[5,7]. Moreover, the kinetics of completion of the CR reaction are also different. A complete distinction between a sequential versus simultaneous CR should therefore be theoretically possible. However, in real systems, especially those produced by cold-deformation, the spatial distribution of the driving forces for the different solid state reactions is not uniform. Consequently, in a certain locale of the microstructure the CR could be sequential, whereas in others it could be simultaneous. Thus, the distinction between a sequential versus a simultaneous CR could be frustrated by these non-uniformities in driving forces. Nevertheless, the theoretical framework described by Hornbogen[5] for the CR transformation can be used to understand the 'average' or mean field approximation behavior of the system and allows speculations and possible conclusions about preeminence of the sequential versus the simultaneous modes of CR transformation.

2.2 CONVENTIONAL ANNEALING AFTER COLD DEFORMATION – PROCESSES AND MECHANISMS

This section presents a brief summary of the classical understanding of the processes of recovery, recrystallization and grain growth as applied to disordered deformed solid solutions that do not undergo an ordering transformation.

The three stages of annealing typically distinguished are the processes of recovery, recrystallization and grain growth[9]. Recovery refers to all those thermally activated processes of defect rearrangements in the deformed microstructure, which do not involve the sweeping of the

deformed structure by migrating high-angle grain boundaries. Thus, during recovery the deformed polycrystalline aggregate retains its identity, while the density of crystal defects (mostly dislocations and vacancies) and their distribution changes. Recovery has been associated with the decrease in number of line and point defects present in the deformed material. The annihilation of dislocations with opposite signs gliding on the same glide planes, vacancy assisted climb of edge dislocations leading to polygonization, annihilation of excess vacancies with grain boundaries and line defects acting as vacancy sinks are some of the mechanisms which are associated with this process[10].

The phenomenon of recrystallization refers to the process by which stress free, equiaxed grains are produced from a heavily stressed microstructural state. Recrystallization has been extensively studied for elemental metals and dilute alloys based on them. Still, the theories of recrystallization have been debated extensively in the literature[11]. Central to all these theories has been the postulate that a stress free grain would be 'nucleated' or formed in the region of high deformation content. Previous studies[12,13,14,15] have clarified that the mechanism of 'nucleation' of a recrystallized grain is intimately linked with the structure of the deformed metal and specifically with the degree of heterogeneity of orientation within each deformed grain. In line with these observations some theories of recrystallization have been proposed[16,17,18,19]. The main ideas in these theories include the following models or concepts:

1) A classical nucleation (or fluctuation) phenomenon involving a heterogeneous or homogeneous mode;

2) Local growth of a polygonized region in the deformed sub-structure to eventually produce a viable nucleus;

3) Coalescence of neighboring sub-grains by the annihilation of dislocations constituting the sub-boundaries between them;

4) Strain-induced boundary migration (SIBM) model, in which a sub-grain within a deformed region grows into its neighbor, forming a bulge which has the orientation of the source grain and is largely free of dislocations.

Of these four conceptual models that have been proposed, the classical nucleation theory has been discredited, as the driving force for recrystallization is not sufficient to account for the energy required to produce a high angle grain boundary. The last three theories involve the rearrangement of dislocation sub-structure (recovery) as a pre-requisite to produce viable high-angle boundaries and do not require the formation of a truly new orientation grain or nucleus in the cold-worked material. Rather, they are based on the further evolution of specific defected regions already present after deformation. Given the complexity involved in the analysis of the phenomenon of recrystallization, one or all theories in tandem can be sufficient to explain the experimental observations. However, the details are still discussed controversially[20].

Various kinetic models have been used to quantify the rate of the process of recrystallization[20,21] . The Johnson-Mehl-Avarami-Kolmogorov (JMAK) model seems to be the most popular model. This model expresses the volume fraction recrystallized as a function of time by the relation

$$X_v = 1- \exp (-Bt^k) \qquad 2.1$$

Here, B and k are constants depending on the material and thermomechanical processing parameters (e.g. T, ε_{cw}).

The annealing phenomenon of recrystallization is complete once the new, essentially strain-free grains have grown sufficiently to impinge on one another. At this point the driving force for recrystallization, the stored strain energy of cold work, has been expended.

If annealing is continued after recrystallization is essentially complete, grain growth dominates the microstructure altering process. The driving force for grain growth arises from the reduction in excess interfacial energy associated with grain boundaries. The process of grain growth is affected by a number of factors, such as the impurity content at the grain boundaries, the orientation relationships across the grain boundaries etc. Grain growth is a phenomenon facilitated by boundary diffusion. Thus, the nature (chemical order, atomic structure, morphology) of the GBs or interfaces plays a very important role in determining growth kinetics. Structurally and compositionally different segments of GBs exhibit different rates of mobility. This would manifest itself in the resultant three-dimensional grain structure that would be obtained during the process of grain growth. It is expected that the largest grains are bound by highly mobile interfaces and that smaller grains that have been unable to grow are bound by low mobility interfaces[22,23,24,25].

Processes of recovery usually lead to annihilation of excess defect content in the matrix grains. Thus, high local concentrations of strain energy, conducive to promote recrystallization can become scarce, therefore affecting recrystallization kinetics. Moreover, the process of recovery can also affect growth, as it can alter the defect content across a high angle grain boundary. Hence, it can be inferred that the elementary processes in annealing are not mutually exclusive, but rather they are interdependent or coupled and may occur simultaneously. The interplay between all these solid state reactions has to be considered, which has made the theoretical modeling of annealing phenomenon quite complex.

2.3 THE ORDERING PHASE TRANSFORMATION AND ASSOCIATED MICROSTRUCTURAL EVOLUTION IN $L1_0$-ORDERED FePd

In the binary Fe-Pd system, for equiatomic composition, the ordered $L1_0$ phase forms from a disordered, high temperature stable, FCC solid solution via a thermodynamically first order phase transformation. This phase transformation can be achieved by quenching the high temperature stable FCC phase to room temperature followed by isothermal annealing treatments at temperatures below the critical ordering temperature, $T_c \approx 920$ K (647°C)[26]. This processing scheme induces ordering to the equilibrium phase and is referred to as conventional processing. The FCC to $L1_0$ ordering proceeds by nucleation and growth of nanoscale ordered domains in the FCC matrix as has been schematically depicted in figure-2.2.

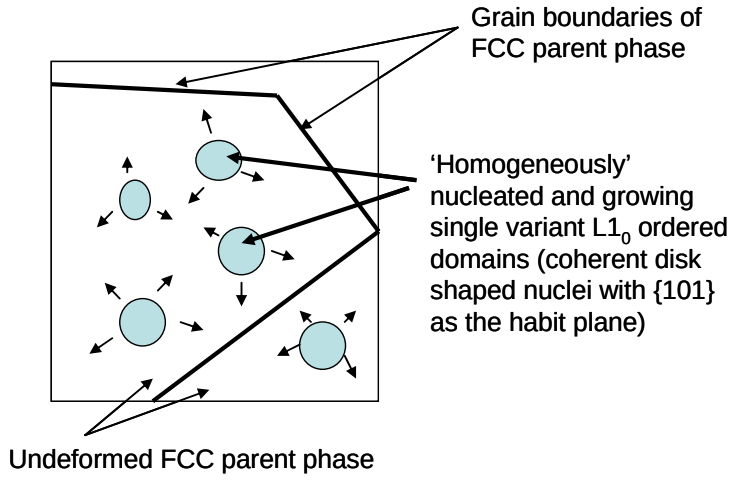

Figure-2.2 Schematic depicting the nucleation and growth of $L1_0$-ordered domains in the FCC matrix during conventional transformation.

During the ordering phase transformation any one of the three cube axes of the parent phase can be altered to yield the c-axis of the tetragonal product phase. Consequently this phase

transformation can lead to three variants of the $L1_0$ phase with three different orientations of the c-axis corresponding to three cube axes of the parent phase. The simultaneous nucleation and growth of all three variants of the tetragonal product phase leads to considerable strain in the matrix. The system tries to reduce the associated strain energy by forming self accommodating arrays of twins with the dodecahedral planes {101} as the conjugation planes. The accommodation is such that the c-domains on one side of the {101} interface compensates for the strain field associated with the c-domains on the other side of the interface. The resultant lamellar microstructure is referred to as the 'polytwinned' microstructure and is shown in figure-2.3[27].

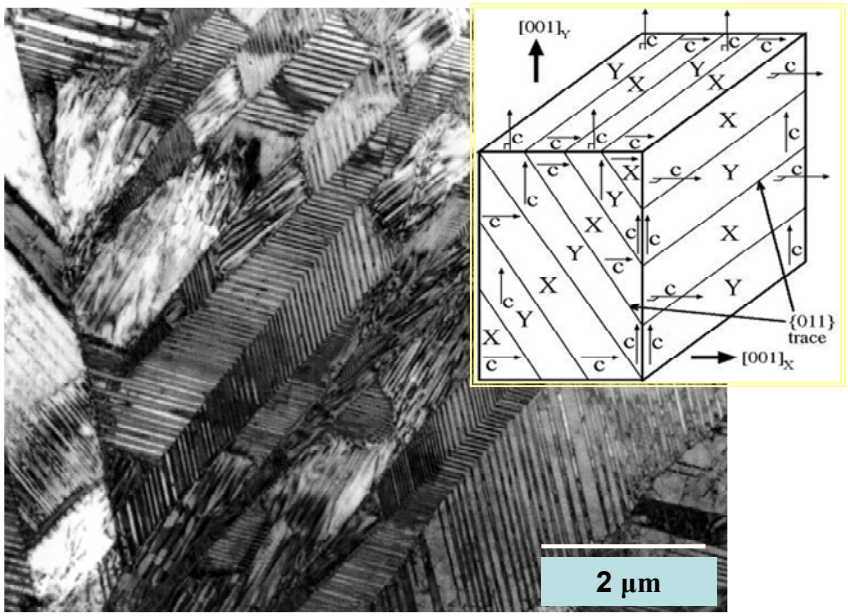

Figure – 2.3 Multi beam – bright field TEM micrograph depicting polytwinned microstructural morphology. Inset- The arrangement of c-axes within the polytwin lamellae.

The selection of the dodecahedral planes {101} as the twin conjugation planes has been rationalized in earlier studies[2]. It has been proven that if the adjacent domains are fitted together

along crystallographically equivalent geometrically identical {101} planes, it can result in formation of a coherent interface with lowest possible shear strain energy contribution to the overall energy penalty in creating the interface[28]. The equilibrium thickness of the polytwin plates has also been determined by considering a competition between the strain and surface energies associated with these plate like structures. It has been proven that the equilibrium spacing (d) would be a material constant given by

$$d^2 = r_0 * D \qquad 2.2$$

Here D is the thickness of the aggregate of these plates and r_0 is a material dependent parameter given by

$$r_0 = \gamma_s / (\lambda * \varepsilon_0^2) \qquad 2.3$$

Here γ_s is the surface energy, λ is the appropriate elastic modulus and ε_0 is the transformation strain.

The polytwin microstructural state has been associated with the rather disappointing technical hard magnetic properties of the conventionally processed FePd[29]. Alternative thermomechanical processing schedules have been investigated to alter the microstructural state. One such schedule involves considerable plastic deformation of the metastable FCC phase prior to annealing at temperatures below T_c[30]. The large density of crystal defects introduced into the material during plastic deformation alters the microstructural evolution during isothermal annealing. Annealing of the plastically deformed FCC phase produces microstructural changes that involve a CR of two processes: 1) The recovery and recrystallization phenomena associated with the annealing of defect structures produced during cold deformation and 2) the phase transformation of disordered FCC to ordered $L1_0$ phase. Interplay between both of these solid-state reactions during annealing

can be utilized to considerably alter the microstructural state of the alloy that enables the suppression of the emergence of the detrimental polytwinned microstructure[31].

For certain conditions this CR produces a microstructure that consists of single variant, $L1_0$-ordered, essentially equiaxed grains. This type of microstructure has been found to significantly enhance the hard magnetic properties of $L1_0$-ordered FePd intermetallics as compared to the polytwinned microstructure[32].

It has been previously shown that the FCC to $L1_0$ ordering transformation during CR is facilitated by a massive ordering mode[30,31]. In this massive ordering mode, the nucleation and growth of single variant new $L1_0$-ordered grains occurs preferentially along deformation heterogeneities and prior grain boundaries of the deformed FCC matrix. Figure-2.4 schematically depicts the massive ordering transformation observed in deformed metastable FCC phase.

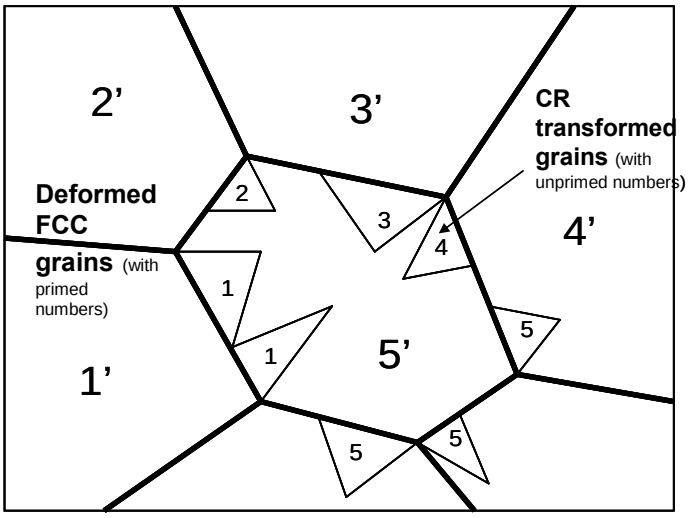

Figure-2.4 Schematic depicting the massive ordering transformation enabling the FCC to $L1_0$ ordering transformation in deformed equiatomic FePd.

The FCC / $L1_0$ interphase interfaces of these newly nucleated $L1_0$-ordered grains sense essentially two different driving forces.

The driving force for the ordering process that is a function of annealing temperature[33]

$$\Delta G_{FCC \rightarrow L1o} \approx \Delta H_{FCC \rightarrow L1o} (T_c - T_{anneal}) / T_c \qquad 2.4$$

and

the driving force for the process of recrystallization that is essentially the stored strain energy of cold work, given by[10]

$$\Delta G_{rx} = \mu b^2 \Delta\rho / 2. \qquad 2.5$$

Where $\Delta\rho$ is the excess dislocation density stored after cold deformation, μ is the shear modulus and b is the Burgers vector.

On sufficient thermal activation and under the influence of these two driving forces the FCC / $L1_0$ interphase interfaces are able to propagate. The moving interphase interfaces would consume the defected FCC matrix in front of them and deposit new, relatively defect free $L1_0$-ordered lattice behind them. This mode of transformation is thus able to sweep out the defect content introduced in the microstructure during deformation and at the same time achieve a completely $L1_0$-ordered microstructure that consists of nearly equiaxed grains.

The microstructural state obtained after the completion of ordering via the massive ordering mode appears morphologically to be similar to the recrystallized microstructure obtained after annealing of deformed disordered solid solutions that do not show an ordering transformation (e.g. annealing of cold deformed Cu). This morphological similarity between recrystallized microstructures and massively ordered CR transformed microstructures has lead to the rather confusing and at times misleading approaches in the literature of applying the recrystallization nomenclature to the discussion of the CR transformation in reversibly ordering intermetallics

systems[34]. Some studies have been cognizant of the differences between these microstructural transformations[30]; however no systematic efforts have been made to distinguish one from another. The absence of such systematic effort in creating a distinction is one of the motivations for this investigation.

The two different mechanistic modes of ordering (conventional mode and CR mode or massive mode) have been introduced and discussed in this section. Both of these modes of ordering can compete kinetically during the microstructural transformation during annealing after cold deformation in the FCC state. It can be envisaged that the system has the option of achieving the ordering transformation by either of these two modes. However, in the presence of sufficient stored strain energy of cold work and sufficient undercooling, with a sufficiently high mobility of atoms, the massive ordering mode can kinetically dominate the transformation.

2.4 CR TRANSFORMATION AND CONVENTIONAL ANNEALING IN INTERMETALLICS – AN OVERVIEW OF PRIOR WORK

In this section a brief summary is presented of the previous work in these two general fields. The questions that have been answered and the ones that have been left insufficiently attended have also been reviewed.

2.4.1 Cold Deformation and Microstructural Evolution during Combined Reaction.

The combined reaction (CR) of ordering and recrystallization has been previously studied in various systems, such as the $L1_2$ ordering Cu_3Au[35], Co_3Ti[36], Ni_3Fe[37], the $L1_0$ ordering CuAu[38,39], NiPt[40], CoPt[41], and the weakly thermodynamically first order B2 ordering FeCo-Cr[42]. It has also been studied in the Fe-Pd system[43]. With an exception of one study[30] all these prior studies have

used the formalism of conventional annealing to describe microstructural changes occurring during annealing after cold-deformation; the CR, in these alloys. A common theme of all of these previous studies has been the retardation of the morphological transformation kinetics in the combined reaction mode (referred to as recrystallization in these studies) with respect to recrystallization in the disordered FCC alloys. Two schools of thought have emerged that would potentially explain this behavior.

1. Networks of dislocations would be created during cold deformation in the disordered condition. Since the disordered phase has a FCC structure, glissile dislocations with Burgers vectors (of the type a/2<110>) would be present. During the CR mode, if the ordering reaction occurs before the recrystallization, it can lead to a change in the character of the dislocations. Some members of the form a/2 <110>, such as a/2[011] and a/2[101], would no longer constitute Burgers vectors of perfect unit dislocation in the ordered structure, but rather equate to imperfect partial dislocations with Burgers vectors that must produce APBs. Possible unit dislocation Burgers vectors contained in the octahedral type planes of the $L1_0$-ordered structure are shown in figure 2.5. Hence, upon ordering prior to recrystallization 2/3 of the unit dislocations in the deformed FCC structure would become superpartial dislocations trailing APBs. The process of recovery precedes recrystallization. The recovery of a microstructure comprising APB dragging superpartials would be expected to be difficult as compared to that of a microstructure consisting only of ordinary or perfect unit dislocations. Thus, the ordered structure would be predicted to recover at a much slower rate and therefore recrystallization kinetics would also be slower. This model of inheritance of the dislocation structures from the deformed disordered condition into the ordered unrecrystallized condition has been proposed previously[38] and constitutes a rather

traditional view for the retardation of microstructural transformation kinetics associated with materials undergoing the CR.

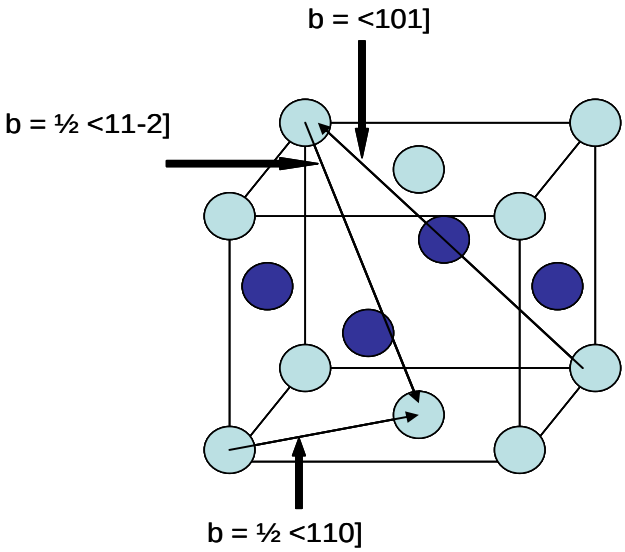

Figure - 2.5 Possible b vectors for unit dislocations in $L1_0$-ordered FePd.

It can rationalize the observed relatively fast CR kinetics in the $L1_0$ system as compared to $L1_2$ or B2 systems. For instance, during $L1_0$ ordering 1/3 of the unit dislocations introduced by deforming the FCC phase are retained as perfect unit dislocations in the ordered crystal, whereas this is not true in $L1_2$ or B2, where all of the perfect unit dislocations in the disordered phase would be rendered to imperfect partial dislocations in the respective ordered phases. However, this model is unable to explain the microstructural transformations during CR that occur after heavy plastic deformation in the disordered phase. CR reactions after heavy plastic deformation have been demonstrated to produce a completely ordered microstructure consisting of essentially only equaixed $L1_0$ grains[32].

2. The second school of thought has been based on the experimental determination of a disordered region near the grain boundaries of ordered grains in the CR transformed $L1_2$ -ordered Cu_3Au[35]. Extremely small (~2nm wide) ordered domains were observed in the disordered grain boundary regions. Based on an energetics argument it was concluded that the ordered domains would exert a 'drag force' on the grain boundary and slow the kinetics during CR transformation. The impingement of these small ordered domains in the grain boundary region during growth would generate antiphase domain boundaries (APBs). The observation of such boundaries was cited as another proof of this mechanism. This rationale for the retardation of kinetics was however discredited in ordered intermetallics such as Ni_3Al that have a high APB energy.

Antiphase domain boundaries have been observed to emerge during the CR transformation in $L1_0$ FePd. Based on these observations prior reports[30] have credited the 'drag force' model (discussed in details in ref # 1) with the retardation in the transformation kinetics. There have however been no direct observations of the ordered domains in the grain boundary responsible for this drag effect. Neither are there any definite experimental proofs of the disordered nature of the grain boundaries. A critical condition for the applicability of the APB drag model is the existence of a narrow ribbon of chemically disordered material at and in the immediate vicinity of the mobile transformation boundary or grain boundary. Only if the apparent width of this boundary layer exceeds a critical dimension required to nucleate ordered phase within the disordered boundary layer would it be possible to develop the drag force from APB formation. Interestingly, antiphase boundaries, as observed in previous reports[30], can also emerge due to occurrence of growth accidents as a mobile high angle grain boundary moves.

Thus, the details of the mechanism or mechanisms responsible for the 'retardation of recrystallization' in cold-deformed ordering systems have not been fully elucidated. In this

regard the possibilities of simultaneous CR reactions of recrystallization and ordering versus sequential CR reactions of ordering followed by recrystallization (or vice-versa) need to be thoroughly investigated. It needs to be emphasized that a clear distinction between the possibility of the massive ordering phase transformation facilitated CR mode and the recrystallization process as observed in conventional annealing has not been achieved in most of these previous studies. Consequently, inappropriate use of terminology from the conventional annealing phenomena of solid state transformation into the CR mode of transformation has lead to an ill-defined framework for analyzing microstructural evolution during annealing of cold deformed alloys that show an ordering transformation.

Another aspect of the CR transformations of equiatomic FePd has been the emergence of a crystallographic texture after the reaction is complete. The components in this texture have been found to be similar to the rolling texture components developed after cold deformation, but have a reduced intensity. It has been previously established that the local stress state in the deformed matrix would favor the nucleation of a particular variant of the $L1_0$ phase[44]. Thus the 'oriented nucleation' theory[45] , in which the new nucleus of the product phase has a certain preferred orientation with respect to the deformed matrix, can be suitably applied to the massive mode of phase transformation that occurs during CR. After the completion of the CR transformation the system would further try to reduce its free energy via grain growth. It has been previously established in FCC metals that the grain boundaries that favor faster grain growth kinetics (and therefore maximize the rate of dissipation of free energy) would be different from the grain boundaries at the stage of nucleation. Moreover, twinning has been established as a mechanism by which the crystal orients itself to produce grain boundaries with highest mobility. It has also been reported that multiple twinning steps (≤ 5) are required to finally obtain grain boundaries

with the highest mobility in FCC metals[46,47]. Prior investigations in $L1_0$ FePd have reported the presence of twinning during CR. A competition between the 'drag force' mechanism in reducing the grain boundary velocity and twinning to form grain boundaries with highest mobilities has been cited as a reason for the subsequent randomization of the CR texture[30]. However, the details of this competition mechanism have not been completely elucidated.

The mechanisms for the emergence of other crystal defects such as {111} microtwins has also been previously reviewed in this system[30]. The classic Dash and Brown mechanism[48], which attributes the nucleation of a microtwin to the collection of stacking fault packets at the mobile grain boundary, has been used to rationalize the presence of microtwins in CR processed FePd[30]. The Dash and Brown approach, however, lacks in mechanistic details and has been modified by Mahajan et al.[49]. Their model entails the nucleation of Shockley partial loops on consecutive {111} planes by growth accidents on propagating {111} steps, which are associated with a migrating grain boundary. Lateral growth of faults has been attributed to the repulsive interaction between Shockley partials constituting the twin boundary. {111} steps have been observed in a migrating grain boundary in other $L1_0$-ordered intermetallics such as MnAl[50]. The generation of microtwins in accordance with the Mahajan model has been observed in massively ordered MnAl. It would be of interest to see whether this model can be extended to explain fault generation in CR processed FePd as well.

The heterogeneous nucleation and growth of single variant $L1_0$ grains at deformation heterogeneities, such as grain boundaries of the disordered deformed grains, shear bands and micro bands, has been previously observed [30,32] . By increasing the density of such defects, the propensity for heterogeneous nucleation of single variant $L1_0$ grains can be greatly increased. Such a nucleation controlled CR transformation has been previously observed in heavily cold

deformed disordered Fe-Pd[51]. It can lead to a microstructure consisting essentially entirely of single variant $L1_0$-ordered grains with a submicron average grain size. It has also been observed[32] that such microstructures have nearly five fold improved magnetic property (e.g. coercivity) as compared to the conventionally transformed $L1_0$-ordered polytwin microstructure. Thus, to summarize, some of the previous studies have been cognizant of the differences in CR transformation and conventional annealing in ordered intermetallics. However, systematic comparison between both of these modes of transformation has not been attempted.

2.4.2 Cold Deformation and Microstructural Evolution during Conventional Annealing

Deformation behavior of $L1_0$-ordered intermetallics with a polytwinned microstructural morphology has been previously investigated. The most extensive studies have been on the $L1_0$-ordered phase (γ) in the Ti-Al binary system[52]. The presence of a yield strength anomaly in the γ phase has sparked an interest in the mechanical behavior of these alloys[53]. The yield strength anomaly refers to an abnormal increase in the yield strength during plastic deformation at higher temperatures. It has been reported previously that a yield strength anomaly also exists in the $L1_0$-ordered FePd[54] and $L1_2$-ordered Ni_3Al[55], but is not observed in some other $L1_0$ systems such as FePt, CuAu [52,53] . The yield strength anomaly has been attributed to the presence of certain non-planar dislocation 'lock' configurations created due to inability of the non-planar dissociated superdislocation structures to cross slip[54,55] . The presence of the yield strength anomaly in both TiAl and FePd may hint toward similar mechanisms being operative during deformation of these ordered intermetallics.

The deformation of the polytwinned FePd at room temperature is relatively well understood in comparison with the ordered alloy with an equiaxed grain structure and will be discussed briefly

in the following section. Dislocation glide and twinning on octahedral planes have been reported as the mechanisms responsible for plastic deformation (in tensile condition) in this polytwinned state[54]. The three kinds of perfect unit dislocations possible in an ordered structure have been introduced in figure-2.5. Deformation twinning can be envisaged as at least three successive shears of the type 1/6<112] on the appropriate adjacent octahedral planes of the $L1_0$ – ordered structure. It has been observed that the plastic flow in this polytwinned microstructure is dominated by the glide of ordinary dislocations (OD)[54]. The individual c-domain interfaces in the polytwinned structure have been identified to act as barriers to the passage of these ODs[56]. These polytwin boundaries act as obstacles because the dislocations have to change their Burgers vector when crossing from one twin band into another. With increasing strain, ODs were found to pile up at the c-domain interfaces resulting in subsequent dissociation into Shockley partials that could propagate into the contiguous c-domains. Detailed investigations of shear transfer across the polytwinned (PT) interfaces have provided new insights into the various dislocation reactions possible that lead to deformation in this microstructure[56]. So called boundary reactions such as the following, have been identified at the PT interfaces –

$b1 = b2 + \Delta b$,

Where b1 is the Burgers vector of the mechanical twin shear in one lamella (b of type 3 x a/6<112>), b2 is the transferred shear in the receiving lamella (e.g. b of type a/2<110]) and Δb is the residual burgers vector debris (a sessile SD of type a/2[101]).

Using such reactions the observed content of superdislocations, superpartials, twinning dislocations and ordinary dislocations has been previously rationalized[57].

With a change in the mode of deformation from tensile to compression plus shear (cold rolling) a change in the resultant microstructural morphology has been observed. Profuse mechanical

twinning has been observed in cold rolled specimens[58]. It has been rationalized by the higher (total 4) number of twinning systems active during compressive deformation (ideally with stress acting along [001]) as compared to lower (only 2) active during tensile deformation [58].

Given the relatively simple geometrical arrangement of the c-lamellae the analysis of the possible deformation mechanisms in the polytwinned microstructure has been manageable. To extend the understanding developed in the polytwinned microstructure to the equiaxed grain structure additional knowledge of grain boundary character, grain size, defect structures within the ordered grains etc. would be required. Shear transfer reactions as developed previously[56] could then possibly be extended to this equiaxed structure in a modified format. Also, the crystallographic constraint imposed by the PT-interfaces on the plasticity mechanism activated in PT-polycrystals of FePd might be removed in the microstructures with essentially equiaxed $L1_0$ grains. Hence, quite different deformation behavior, more directly related to the dislocation properties of the $L1_0$-ordered FePd phase may result. To date this topic has not been studied due to the difficulty in avoiding the formation of the PT microstructure.

The deformed ordered state would be a starting stage for the microstructural evolution during subsequent recrystallization and requires a thorough understanding. The driving force for recrystallization stems from the stored energy of cold work and a critical minimum driving force would be required to initiate recrystallization. Unfortunately due to an inability to deform considerably in the ordered state, recrystallization studies in the ordered state have been rather rare. Very early studies[59] in fact did not observe recrystallization on annealing after small deformation (10% in compression in Ni_3Al) and suggested that it might be impossible to recrystallize an ordered material. Later studies [60, 61] managed to achieve recrystallization and

showed this to occur at a slower rate than for a disordered material. Two approaches have been adopted to explain the rather slow kinetics of recrystallization in ordered alloys –

1. The recrystallizing grain boundary has a different atomic structure in the ordered condition as compared to the grain boundary structure in disordered alloys. A lower mobility of the boundary in the ordered condition in addition with the lower lattice diffusivity in the ordered lattice have been held responsible for the slower recrystallization kinetics.

2. The interactions between dislocations and defects in the ordered lattice may inhibit dislocation rearrangements during recovery and delay or prevent formation of new grains. This could lead to slower recrystallization kinetics.

Elucidation of the mechanisms responsible for the retardation of kinetics of recrystallization has been attempted previously. In a study on $(Co,Fe)_3V$, Cahn et al[62] have shown that the presence of long range order leads to a slowing of recrystallization kinetics by nearly three orders of magnitude. The precise reasons for the slower kinetics have not been established. It was however brought to light that the concurrent recovery with recrystallization greatly affected the overall kinetics.

The effect of the nature of the ordering transformation on the annealing phenomenon has also been investigated. Recrystallization studies in cold deformed β brass (CuZn) that has a B2 structure have been previously conducted[63]. It was reported that the recovery and recrystallization kinetics in this system were unaffected by the presence of the ordered structure and did not show any retardation. This observation is in direct contrast with other $L1_0$ and $L1_2$-ordered systems that have shown retardation in kinetics of recrystallization[59,60]. The disorder → B2 ordering reaction in the Cu-Zn system is a higher order phase transformation. The nature of the change in the order parameter as the disordering temperature is approached would be

different in these B2 ordered intermetallics as compared to the $L1_2$ or $L1_0$ ordering systems that show a first order phase transformation. A gradual change in the LRO parameter would be observed over a temperature range for the B2 system, whereas the $L1_0$, $L1_2$ systems would show a much more precipitous change at the transformation temperature. It has been proposed that the differences in order parameters for similar T / T_c would reflect in the ability of dislocations to rearrange. Dislocation motion, for a particular T / T_c, has been observed to be easier in the B2 structure as compared to the other ordered systems leading to much faster recovery and thus recrystallization kinetics.

Thus, to summarize, there have been some studies aimed at understanding the conventional annealing behavior of cold deformed ordered intermetallics. However, such studies have not been conducted in the FePd system. The cold deformation behavior of the polytwinned $L1_0$-ordered FePd is relatively well understood as compared to the cold deformation of the equiaxed microstructure. There is currently very little understanding of the recovery, recrystallization and grain growth that would be observed during annealing of cold deformed $L1_0$-ordered FePd with equiaxed grain structure. The understanding of the annealing phenomena in other ordered systems also appears to be currently underdeveloped. Thus, this study aims to address the paucity of knowledge in the field of annealing of cold deformed ordered intermetallics. Moreover a direct comparison between the CR mode of transformation and conventional annealing of deformed $L1_0$-ordered FePd is also intended. Such a comparison would enable the creation of vital distinctions between these two modes of transformation that is currently underdeveloped in the literature.

3.0 MOTIVATION

As discussed in the prior section, attempts have been made to understand the underlying mechanisms that lead to changes in the microstructural state during CR and conventional annealing transformations in ordered intermetallic systems. Some systematic understanding of the CR transformation has been developed to date. The effects of parameters, such as the amount of prior cold deformation, the temperature of annealing etc on the microstructural evolution have been studied in the CR transformation of equiatomic FePd[30,32]. However, the details of mechanisms that lead to defect structure evolution in CR transformation still remain to be comprehensively understood. As discussed previously the magnetic properties of these CR processed $L1_0$-ordered FePd intermetallics depend upon the microstructure and defect structure. A five-fold improvement in the coercivity of these intermetallics has been previously observed[32] when, using the CR route, equiaxed grain microstructure with a submicron average grain size in polycrystals was obtained. The mechanisms that lead to defect structures evolution during CR processing need to be elucidated to achieve a controlled enhancement in microstructure sensitive properties.

The conventional annealing of cold-deformed $L1_0$-ordered FePd intermetallics has not been previously attempted. Neither has there been a systematic study of the annealing phenomena in other ordered intermetallics with the possible exception of Ni_3Al. Due to the expected sluggishness of kinetics of annealing in the ordered state, this process can also potentially be

used to achieve a considerably refined microstructure. Thus, the process of conventional annealing has significant potential in creating microstructures with enhanced magnetic properties. In the conventional annealing process, similar to the CR transformation, crystal defects would evolve. The nature of the mechanisms for the evolution of these defects are currently unknown. Both defect structure and mechanisms of defect genesis need to be elucidated to attain better microstructure control and therefore a controlled property enhancement. As stated previously, $L1_0$-ordered FePd intermetallics are a good model system. Therefore, the understanding gained on the mechanisms of defect formation in this system can potentially be applied to an entire class of $L1_0$-ordered intermetallics that are technologically interesting.

It can be seen from the prior work in this field that to date an insufficient effort has been made to purposefully distinguish between CR transformation and conventional annealing in the ordered state. This general lack of clarity in previous reports may have stifled the growth of basic knowledge in this field. A comprehensive study that is mindful of these differences and would be able to compare and contrast the microstructural evolutions between both of these modes of microstructural transformation is timely. This study would greatly aid in creating a framework useful for future studies and would also serve as a good resource for mechanisms of microstructural transformation during annealing of cold deformed, ordered intermetallics. Thus, addressing the surprising lack of systematic understanding of the two different phenomena of CR and conventional annealing is the main motivation for this study.

4.0 OBJECTIVES

Prior sections have developed the current status of the understanding in this general field and have also highlighted the questions that need to be answered to make progress. In this section definite objectives will be developed that would form the foundations of this study.

There are two parts to this study –

1. Investigation of microstructural evolution during CR.

2. Investigation of microstructural evolution during conventional annealing.

The objectives pertaining to each of these parts are discussed in the following paragraphs.

4.1 MICROSTRUCTURAL EVOLUTION DURING CR

1. Development of an understanding of the microstructural mechanisms responsible for evolution of crystal defects such as APBs, microtwins, stacking faults, annealing twins etc. An emphasis would be laid on extending / modifying and extending the models accepted for generation of these defects in FCC based materials during annealing.

2. Understand the evolution of crystallographic texture during the CR reaction. Since CR involves an ordering reaction concomitant with the annealing phenomena, the crystallographic texture evolution would be expected to be different in this process as compared to conventional

annealing. Texture analysis would thus provide an understanding of the effect of the ordering phase transformation on overall microstructural development.

3. Understand the process of grain growth after CR reaction. Grain growth constitutes a process by which the excess interfacial energy present in the system is reduced. Crystallographic defects such as twins, APBs can also evolve during the process of grain growth. Grain growth can also lead to a generation of new crystallographic texture in the microstructure. It has been established previously that grain size / texture and defect content within these CR transformed $L1_0$-ordered grains affect the hard magnetic properties such as coercivity. Thus the understanding of the processes active during grain growth could open new avenues for magnetic properties enhancement.

4.2. MICROSTRUCTURAL EVOLUTION DURING CONVENTIONAL ANNEALING

1. Understand the cold deformed state in the polycrystalline $L1_0$-ordered alloy with equiaxed morphology. The deformed condition is the starting stage for microstructural transformations during annealing. The nature and distribution of crystal defects introduced during cold deformation would govern the kinetics of the subsequent annealing phenomena. Thus a thorough understanding of this state is essential.

2. Understand the mechanisms leading to the three distinguishable phenomena of recovery, recrystallization and grain growth during annealing of the ordered, cold deformed alloy. These phenomena are expected to be facilitated by dislocation rearrangements similar to those observed in FCC metals. However, the presence of ordered structure with certain dislocations (e.g. superdislocations and superpartials) not observed in FCC metals is expected to alter the kinetics

and the resultant microstructural morphology. These effects of the ordered structure on the annealing behavior are intended to be explored in detail.

3. Understand the evolution of an annealing texture from the prior cold deformed state in the ordered alloy. This texture evolution analysis in tandem with the texture evolution studies during CR would shed light on the effect of ordering process on the annealing behavior of the cold deformed alloy. It would also provide experimental proof for theories of 'oriented nucleation' during CR that have been previously proposed.

4. Understand the mechanisms leading to generation of crystal defects during conventional annealing.

Thus in this study two different routes of microstructural transformation would be identified and investigated separately and will allow direct comparison. The similarities and disparities in both of these routes are intended to be highlighted. Therefore, in this study, it is intended to create a clear distinction between the different solid state transformations of CR and conventional annealing.

5.0 EXPERIMENTAL PROCEDURE

5.1 ALLOY PREPARATION

The equiatomic composition alloy was produced at Ames National Laboratory in Iowa by the Materials Preparation Center (MPC). High purity (99.99%) iron plugs were added to the required amount of high purity palladium granules (99.95%), both of which had been acquired from Alfa Aesar, to produce the equiatomic mixture. Vacuum arc melting was employed to melt the alloy followed by casting on a water-cooled copper hearth. This procedure yielded a button of approximate dimensions 45mm x 45mm x 13mm. Compositional homogeneity of the button was ensured using the EDAX compositional microanalysis in the SEM through the cross section laterally and normal to the thickness.

5.2 HEAT TREATMENTS

To ensure controlled non-oxidizing atmosphere for heat treatments all the samples were encapsulated in quartz tubes. The same encapsulation procedure was followed for all samples. In this procedure, the samples, along with a tantalum foil as an oxygen-getter, were placed in the quartz tube that was sealed at one end. The tube was then thinned down with a torch, approximately 10 cm away from the closed end. The open end was then attached to a vacuum

system and pumped down to approximately 20 millitorr before back-filling with high purity argon to a pressure of approximately one-half atmosphere. The valve to the vacuum system was reopened and again pumped to 20 millitorr. This flushing procedure was repeated 4-5 times before back-filling with argon and then sealing off the tube. It was ensured that the tantalum foil and the sample are not in physical contact whilst the heat treatment was in progress.

5.3 HOMOGENIZATION AND DISORDERING ANNEALING TREATMENT

As-cast buttons were cut perpendicular to the chill surface with a slow speed saw so that each slice had two nearly parallel surfaces. These specimens were then subjected to cold rolling to break down the cast structure. A thickness reduction to approximately 45% was achieved with the slices always going through the rollers length-wise and always in the same direction with the parallel surfaces of the samples touching the rollers. The deformed specimens were then encapsulated, and placed in a furnace at a temperature of 950˚C, which is within the disordered phase field of the FePd phase diagram. After 8 hours at this temperature the quartz tubes were quenched into ice-brine solution, resulting in a relatively rapid quench to preserve the disordered phase.

5.4 CR AND CONVENTIONAL ANNEALING – PROCESSING STRATEGY

The homogenized equiatomic FePd samples with the metastable disordered FCC phase were subjected to two different processing schemes to a achieve CR and conventional annealing. These schemes have been depicted schematically in figure-5.1

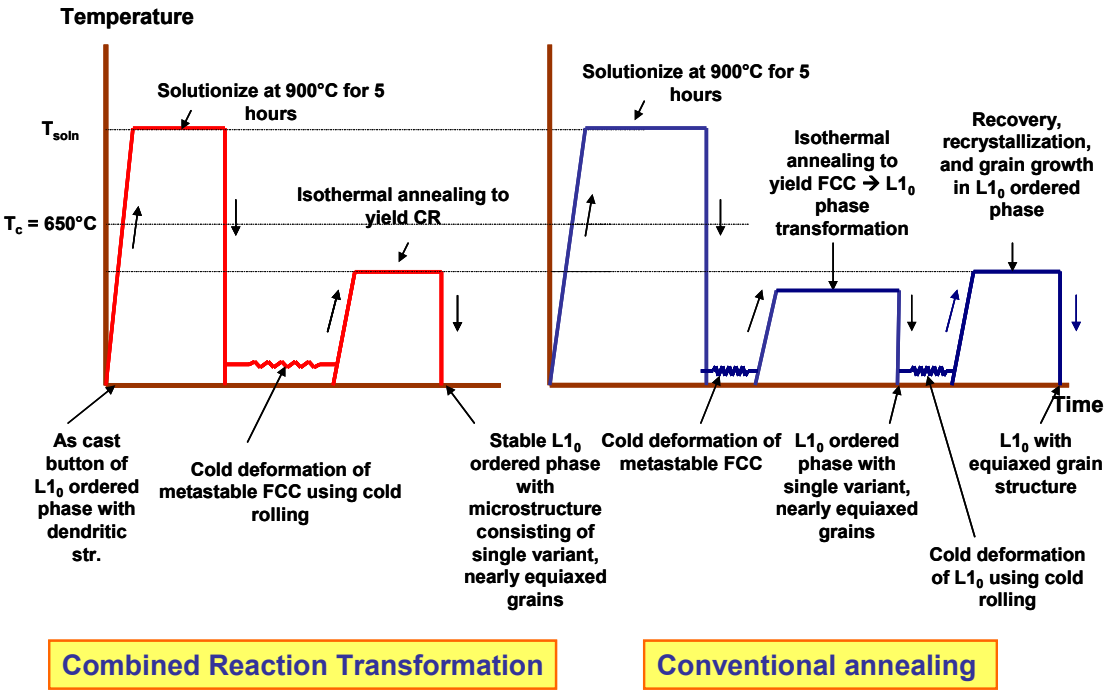

Figure-5.1 Schematic depicting the processing scheme for the two different modes of transformation.

In order to achieve CR mode of transformation the homogenized disordered FCC phase was cold rolled to 97% reduction in thickness. This cold deformed metastable FCC phase was then CR annealed at 600°C for times ranging from 0.5 hour to 24 hours. The CR annealing temperature of 600°C was used as previous studies[51] have reported that at this annealing temperature a completely equiaxed grain $L1_0$-ordered microstructural morphology can be generated via a simultaneous CR of ordering and annealing of defects. The samples were quenched into ice-brine after the annealing treatments were complete.

Cold deformation of the $L1_0$-ordered microstructure with an equiaxed grain morphology was intended to be achieved prior to conventional annealing. To obtain an equiaxed microstructural state prior to cold deformation, the CR route was utilized. The metastable FCC phase was cold

rolled to 80% reduction in thickness followed by CR annealing at 525°C for 45 hours. This annealing treatment yielded a microstructure that consisted of approximately 90 vol% of the equiaxed grain morphology. The remaining 10% comprised $L1_0$-ordered domains that had undergone coarsening (but did not form a well defined polytwin microstructure). An example of this starting $L1_0$-ordered microstructure has been depicted in figure-6.34 (pg 87). This nearly completely equiaxed $L1_0$-ordered microstructure was then cold rolled to 90% reduction in thickness (with incremental increases of 20%, 50%, and 75%). After cold deformed to 90% reduction in thickness this alloy was conventionally annealed at 600°C for times ranging between 0.5 hour to 24 hours.

The annealing heat treatment temperature was maintained the same (600°C) during CR transformation and conventional annealing transformation. Moreover the amount of (%) reduction in thickness applied to the samples prior to both of these transformations were also comparable (97% and 90% prior to CR and conventional annealing respectively).

5.5 X-RAY DIFFRACTION

X-ray analysis was performed using a computer operated Phillips X'pert system operating at 40kV, 30mA and with CuKα radiation. Cold rolled and annealed samples with dimensions of 10mm x 10mm x 0.018mm were prepared with the rolling direction in plane. The 'powder diffraction' technique was used for phase and c/a ratio characterizations (the symmetric Bragg-Brentano geometry for XRD). The powder diffraction unit consisted of a collimating slit with a width equivalent to an angular range of 0.25˚; a multi-purpose sample stage and a curved graphite monochromator were used to scan for the Bragg angles of the various crystal phases.

These scans were typically run with a step size of 0.02˚ and the dwell time per step of 0.8 seconds.

The Philips X'pert XR-diffractometer in the texture analysis mode has been used to conduct global texture studies. The texture unit involved a collimated point source, an open Eulerian cradle and parallel beam optics. The geometry for the texture determination is shown in figure-5.2 with the sample starting off in the powder diffraction geometry with a fixed θ_B corresponding to a specific set of planes {hkl}.

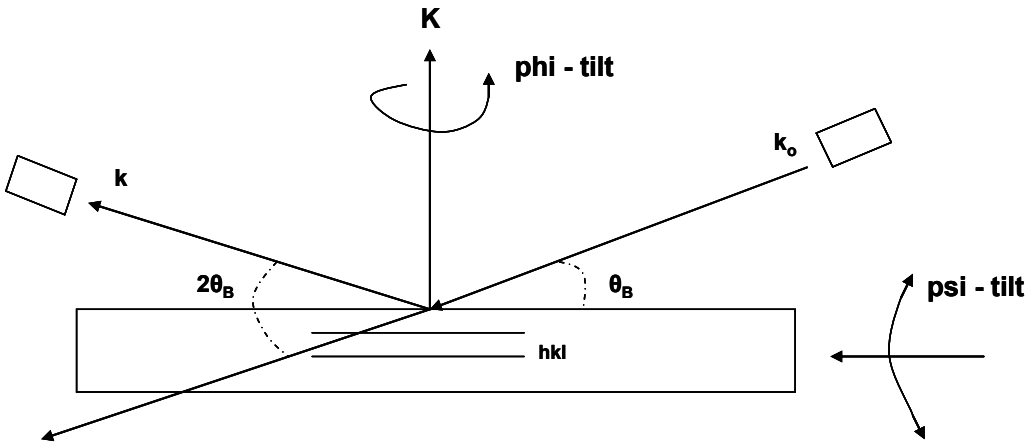

Figure-5.2 X-ray diffraction experimental setup for texture analysis with k_o – the incident beam, k – diffracted beam and $K = k-k_o$

The scans were made as the sample was rotated around its normal, from phi = 0° to 360° in a continuous mode and tilted between psi = 0° to 85° (increments of 5°) about the axis defined by the intersection of the source/detector and the sample surface. The time required to obtain a pole figure for each of the {hkl} was approximately 20 mins. Background and defocusing errors were also obtained in this geometry for each of the {hkl}. Background and defocusing errors corrected pole figures {111}, {200}, {220} and {113} were used for the determination of orientation

distribution function (ODF) in the deformed FCC condition. Five diffraction peaks were used, including {111}, {200 / 020}, {002}, {202/022} and {311/131}, for calculation of ODFs in the ordered condition. Ghost-corrected ODFs were calculated with the proprietary Philips software of the X'pert system, which is based on the WIMV algorithm[64], using crystal symmetry and unit cell dimensions of the $L1_0$-ordered FePd.

5.6 ELECTRON MICROSCOPY

TEM observations were conducted in the rolling plane on samples in the deformed and the annealed state. 3mm diameter discs were drilled using a slurry-drill and SiC abrasive. These discs were further polished to 30 μm in thickness and electron transparent foils were prepared using an E.A. Fishione twin-jet electropolisher in an electrolyte of acetic acid 82%, perchloric acid 9%, and ethyl alcohol 9% by volume. The electropolishing was conducted using an ice bath to cool the electrolyte to approximately 0˚C. A voltage of 30V and a jet speed of five were used. Transmission electron microscopy was conducted on the TEM, JEOL JEM-2000FX operating at 200 kV and utilizing a GATAN double tilt specimen holder. High resolution transmission electron microscopy was conducted at the National Center for Electron Microscopy (NCEM, Berkley-CA). A Phillips CM 200 FEG microscope with a GATAN Imaging filter operating at 200 kV was utilized. Zero-loss filtered imaging was employed. Frequently an objective aperture was used to limit information transfer to spatial frequencies associated with (hkl) up to 200.

The sample preparation for scanning electron microscopy included essentially similar steps as outlined earlier. There was however no need for thickness reduction of the 3 mm diameter discs and the polishing effect of the electropolisher was sufficient to provide good contrast in the

backscattered electron (BSE) and the secondary electron (SE) modes. SEM investigations were conducted on a field-emission gun equipped Philips XL30 SEM, with facilities for BSE, SE contrast imaging and X-ray microanalysis using the EDAX composition analysis program. Orientation Imaging Microscopy (OIM) investigations were conducted in the electron back-scatter patterns (EBSP)[65] mode in SEM, utilizing the TSL software.

5.7 MAGNETIC MEASUREMENTS

Magnetic property measurements were conducted on 3mm diameter discs with known mass. Magnetic hysteresis loops were measured using a Lakeshore model 7300 vibrating sample magnetometer. Fields approaching 15kOe were applied to the samples using a Walker laboratory electromagnet and a model 668 Lakeshore power supply. IDEAS – VSM version 2 software was used for magnetic data collation and plotting of the hysteresis loops.

6.0 RESULTS

The motivation for this study is to compare and contrast the two distinct modes of solid state transformations of CR and conventional annealing in equiatomic Fe-Pd. The results of this study are presented in this chapter, such that they would form the kernel for discussion in the next chapter. The results for each of these solid state transformations are individually briefly discussed in this chapter, whereas their juxtaposition for comparison is intended in the next chapter.

6.1 COLD DEFORMATION IN DISORDERED FCC (γ) Fe-Pd

Figure-6.1 is a Multi-beam bright field, plan view TEM micrograph depicting the cold deformed FCC (γ) FePd. This is the starting microstructure prior to CR transformation. The contrast variations depicted in this multi-beam bright field TEM micrograph can be associated with the large density of crystal defects introduced during cold rolling. The diffraction pattern in figure-6.2 has been obtained from this cold deformed microstructure. The individual rings observed in this diffraction pattern can be indexed using the lattice parameter and structure factor for disordered FCC (γ) FePd. The presence of strain in the microstructure is evident from the arcing observed in this diffraction pattern. Moreover, the absence of any intensity in the diffraction

pattern corresponding to the superlattice reflections (such as 001,110 etc.) indicates the disordered FCC crystal structure of the deformed microstructure.

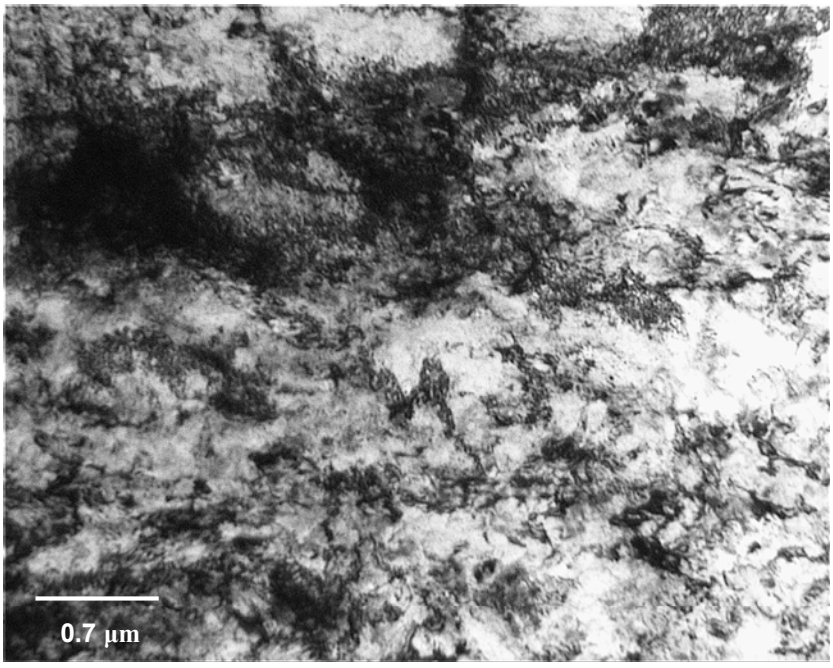

Figure-6.1 Multi-beam bright field TEM micrograph depicting the microstructure after cold rolling to 97% reduction in thickness in the disordered FCC (γ) FePd.

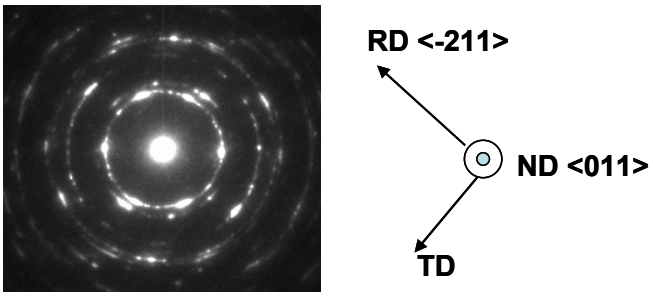

Figure-6.2 Large area diffraction pattern depicting rings corresponding to the fundamental reflections in FCC FePd. The rolling direction and the transverse direction have also been identified based on the knowledge of emergence of a brass texture after cold rolling in FCC condition (ref – figure 6.4)

Figure-6.3 is a Plan view SEM micrograph obtained in the crystallographic orientation sensitive Backscatter electron (BSE) mode depicting the cold deformed microstructure at a smaller magnification as compared to the TEM micrograph of figure-6.1. Regions that appear to have similar BSE contrast features can be discerned in this micrograph. Such regions are most likely the 'pancake like' cell structures that develop during cold rolling. The emergence of such pancake like structures would be most evident in cross section TEM investigation of cold deformed FCC FePd. Previous investigations[30] have convincingly illustrated the development of such cell structures in cross sectional TEM observations.

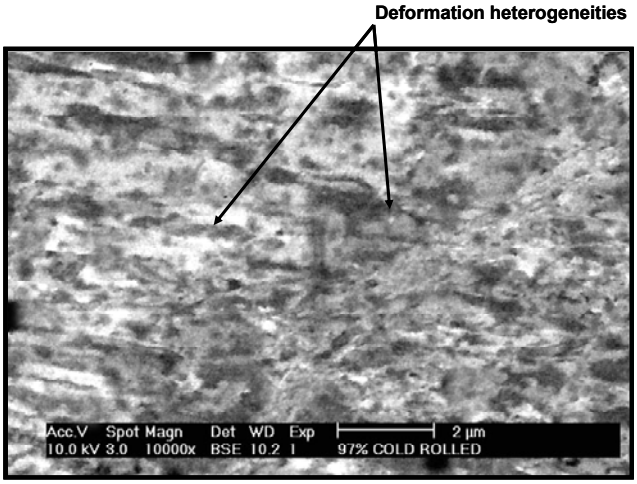

Figure-6.3 SEM micrograph in the BSE mode depicting the cold deformed FCC (γ) FePd.

The presence of a large number of deformation heterogeneities can also be discerned from the micrograph in figure-6.3. From figures-6.1 and 6.3 it can be concluded that there are spatial variations in the crystal defects density in the cold deformed microstructure. The effects of such spatial variations on the CR transformation have been previously investigated[31]. Preferential nucleation and growth of CR transformed $L1_0$-ordered grains has been observed to occur at

certain deformation heterogeneities. In the next section it is intended to contrast this characteristic of the CR transformation with the recovery and recrystallization processes that occur during conventional annealing.

The deformation of the FCC (γ) FePd is facilitated by glide of ordinary dislocations (with b of type 1/2<110>) and Shockley partial dislocations (with b of type 1/6<112>) on {111}[30]. The crystallographic constraints on the deformation mode would lead to development of a crystallographic texture as deformation (by cold rolling) proceeds. To understand the development of crystallographic texture (henceforth referred to simply as 'texture'), orientation distribution functions (ODFs) obtained using X-ray diffraction have been utilized.

The ODF is a mathematical tool that can be used to represent textures[66]. The three axes of the cold rolled specimen (Normal direction ND, Transverse direction TD and Rolling direction RD) can be brought into correspondence with the crystal axes by performing three consecutive rotations. These three rotation angles are referred to as the Euler angles (phi1, phi and phi2). The three dimensional plot of these three angles in an orientation space provides the tool to represent all possible types of textures in cubic materials. Thus, the ODF is calculated in a three dimensional space with the three Euler angles representing the three orthogonal axes of this space. To make the 3D space accessible for analysis, usually it is sectioned along one of the three axes. The most common method has been sectioning the space along phi2 axes while depicting the variation in the ODF with respect to the two remaining axes (phi and phi1)[67].

Figure-6.4 is a phi2 constant section plot of the ODF obtained after cold rolling the FCC (γ) FePd to 97% reduction in thickness. Each square represents a phi2 = constant angle section and it depicts the variation in intensity of the ODF with respect to the two remaining axes.

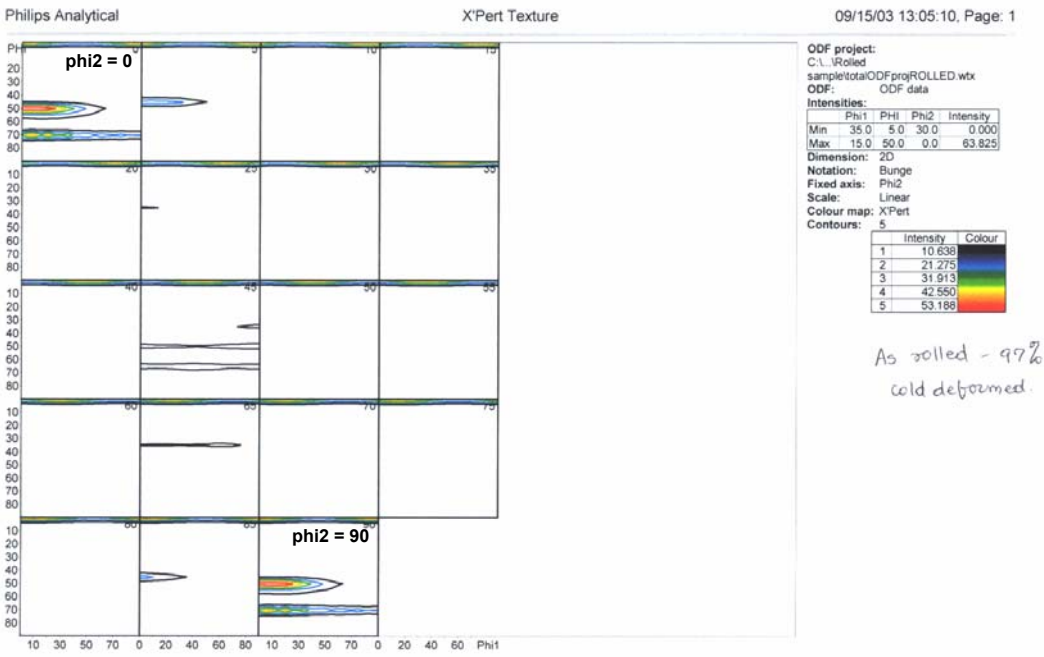

Figure-6.4 A phi2 constant section of the ODF after 97% reduction in thickness during cold rolling in FCC condition.

As can be seen from this ODF plot, intensity maxima appear in the phi2 = 0° and phi2 = 90° constant sections (near phi = 45° to 50° and phi1 = 0° to 45°). The presence of such intensity maxima would indicate the development of a strong texture during the process of cold rolling. This result is in agreement with prior observations[30] that have observed similar texture evolution after 80% reduction in thickness via cold rolling in the FCC (γ) FePd. A well accepted nomenclature exists for the texture components that evolve during the process of cold rolling of cubic materials[67]. Utilizing this nomenclature for the cold deformed FCC (γ) FePd it seems appropriate to identify and address the observed texture signature as the 'Brass component' ({011} are within the rolling plane and <-211> are along the rolling direction). Such a texture component would be expected to evolve during cold rolling of low to intermediate stacking fault

energy FCC materials[67]. Thus the presence of the Brass component in the ODF of the cold rolled FCC (γ) FePd supports previous assertions that categorize FCC (γ) FePd as a low to intermediate stacking fault energy material[57].

6.2 COMBINED REACTION TRANSFORMATION

6.2.1 Texture Evolution during CR Transformation

Combined reaction transformation at 600°C (< T_c ~ 650°C) after 97% reduction in thickness in the FCC (γ) FePd has been experimentally investigated. CR-annealing at 600°C involves the annealing of defects introduced in the FCC phase concomitant with the FCC to $L1_0$ ordering phase transformation. Previous studies[32] have reported that the $L1_0$ ordering phase transformation is complete after 3 hours of annealing at 600°C after 97% reduction in thickness in FCC condition. Moreover, it was also reported that the microstructure consisted nearly entirely of equiaxed $L1_0$-ordered grains (~95% fraction consisting of nearly defect free $L1_0$-ordered grains, while the remainder was comprised of the fraction transformed by the conventional mode yielding ordered domains along with crystal defects inherited from the deformed FCC phase). Figure-6.5 is a SEM micrograph obtained in the BSE mode that depicts the morphology of the equiaxed $L1_0$-ordered grains obtained when CR annealing is complete after 3 hours at 600°C.

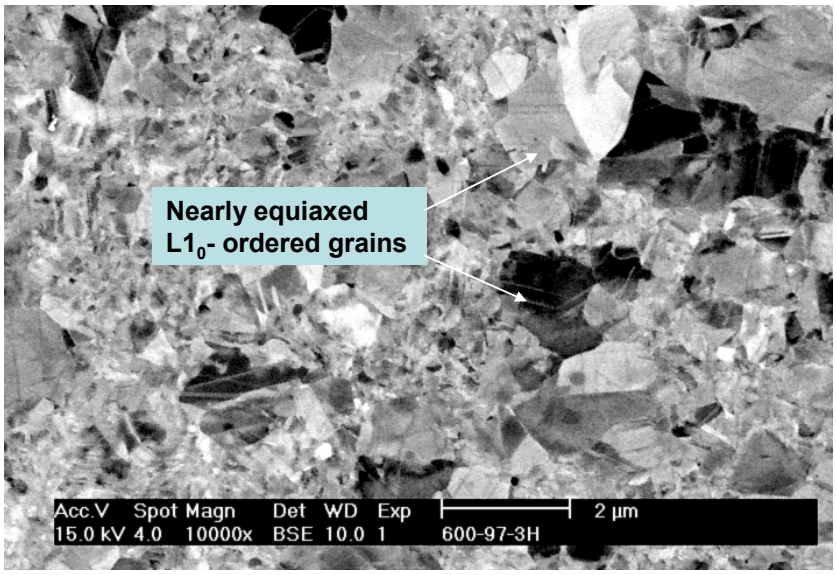

Figure-6.5 SEM micrograph in the BSE mode depicting the microstructure after completion of ordering during annealing at 600°C.

Figure-6.6 is a phi2 constant section of the ODF obtained from the sample that has been CR-annealed for 4.5 hours at 600°C after 97% reduction in thickness in the FCC phase. This is the condition when the CR transformation is complete and the small fraction of the ordered domains and residual crystal defects has been consumed by the $L1_0$-ordered grains. A strong intensity can be observed in the phi2 = 0° and phi2 = 90° constant sections of this ODF. A comparison between the texture components in the cold deformed FCC phase (figure-6.4) and the CR transformed $L1_0$-ordered phase (figure-6.6) reveals similarities in texture signatures. It can be concluded that the main texture or fiber orientation component observed in the cold deformed FCC phase (Brass component) is retained in the CR transformed $L1_0$-ordered phase even when the microstructure changes from a cold deformed FCC phase to a $L1_0$-ordered phase consisting entirely of equiaxed grains. The maximum intensity in the texture signature (50 times random) is stronger in the cold deformed condition as compared to the CR transformed condition (17 times random). Nevertheless, there is an unequivocal similarity between the texture signatures.

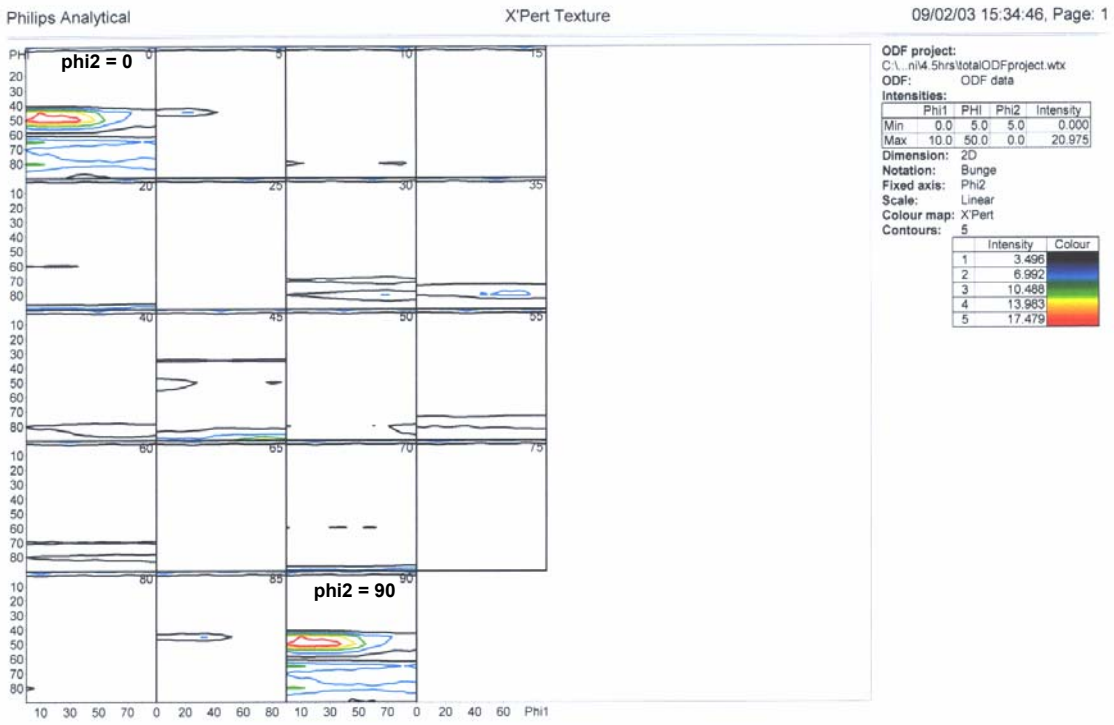

Figure-6.6 A phi2 constant section of the ODF after CR annealing for 4.5 hours at 600°C.

The annealing of disordered deformed FCC solid solutions that do not undergo an ordering transformation (e.g. annealing of cold deformed Cu) involves only recovery, recrystallization and grain growth. The process of recrystallization in disordered deformed solid solutions that do not show an ordering transformation can produce equiaxed microstructures that are morphologically similar to that depicted in figure-6.5. However, recrystallization proceeds by creation of essentially stress-free grains with new orientations in the deformed matrix. A recrystallization texture, distinctively different from cold-rolling texture, would be expected to develop[16-19]. This is in contrast with the considerable retention of texture observed during CR transformation of the cold-rolled FCC (γ) FePd to $L1_0$-ordered (γ_1) FePd. Thus, while morphologically similar microstructures are established in recrystallized FCC solid solutions and CR-transformed $L1_0$-

ordered FePd, significant differences in crystallographic grain orientations exist. This implies significantly different microstructural pathways and mechanisms by which these microstructures are attained during annealing after cold-deformation.

TEM investigations have been conducted to ascertain the microstructural origin of texture similarities in cold deformed FCC phase and CR transformed $L1_0$-ordered phase. Figure-6.7 is a bright field TEM micrograph depicting the microstructural state at an intermediate stage in CR transformation (0.5 h at 600°C after 97% reduction in thickness in FCC condition via cold rolling). The ordering transformation in the CR mode proceeds by nucleation of single variant $L1_0$-ordered grains at deformation heterogeneities in deformed FCC matrix and their growth (figure-6.7). The heterogeneous nucleation sites for $L1_0$–ordered grains forming by CR mode of transformation include prior FCC grain boundaries, shear bands and microbands[51].

Figure-6.8 is a multi-beam bright field TEM micrograph obtained from the same sample as figure-6.7. The strain contrast observed in this micrograph results largely from the high density of dislocations introduced during cold rolling with some contribution from coherency strains associated with the presence of nanoscale coherent $L1_0$-ordered precipitates. The micrograph in figure-6.8 is obtained with the electron beam direction close to [110] zone axis and the superlattice spots in the accompanying diffraction pattern indicate the presence of $L1_0$ -ordered phase in the deformed FCC matrix. To identify the morphology of $L1_0$-ordered phase controlled tilting TEM experiments have been conducted.

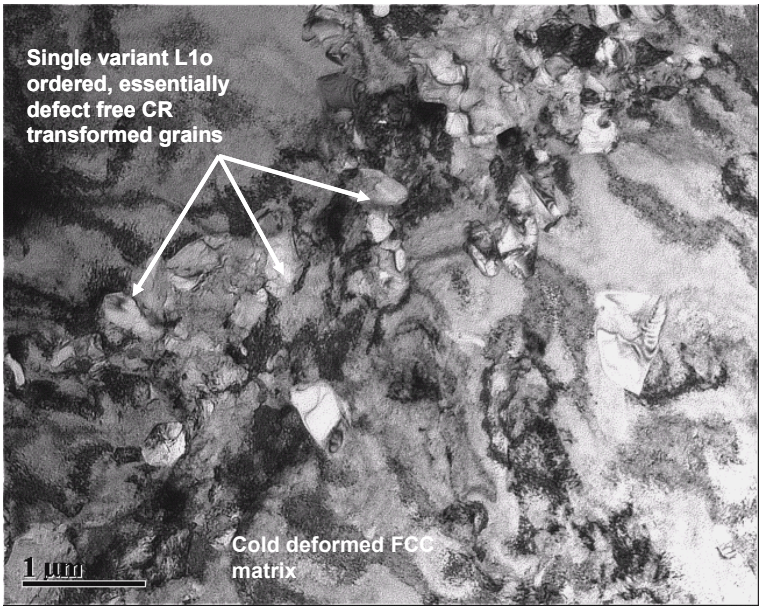

Figure-6.7 Multi-beam bright field TEM micrograph depicting the nucleation and growth of $L1_0$ -ordered grains at preferential locations in the cold deformed FCC phase.

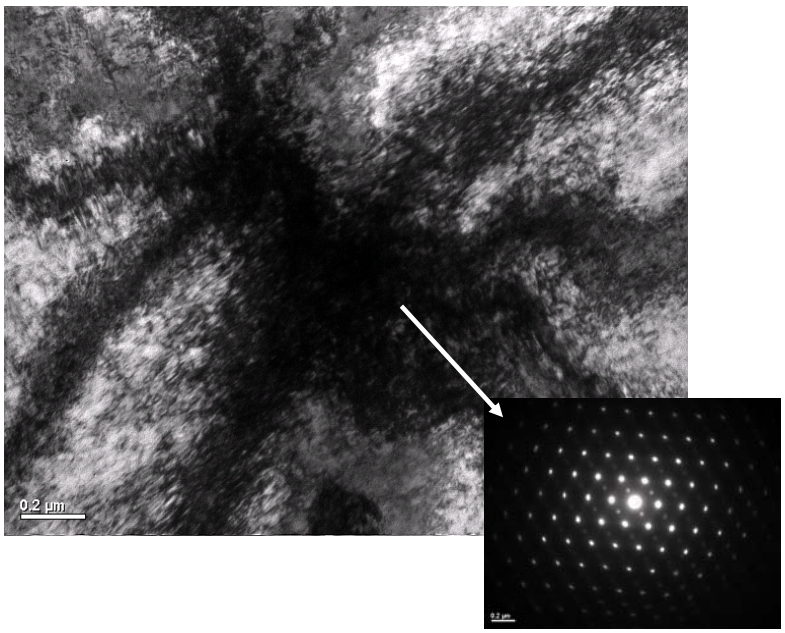

Figure-6.8 Multibeam bright Field TEM micrograph from deformed FCC matrix. Inset-diffraction pattern with [110] as zone axis.

Figure-6.9 is a bright field TEM micrograph from the same area as in figure-6.8 after tilting about 13° clockwise about [1-11] as the rotation axis with diffraction patterns from regions 'Y' and 'X' as inset-1 and inset-2.

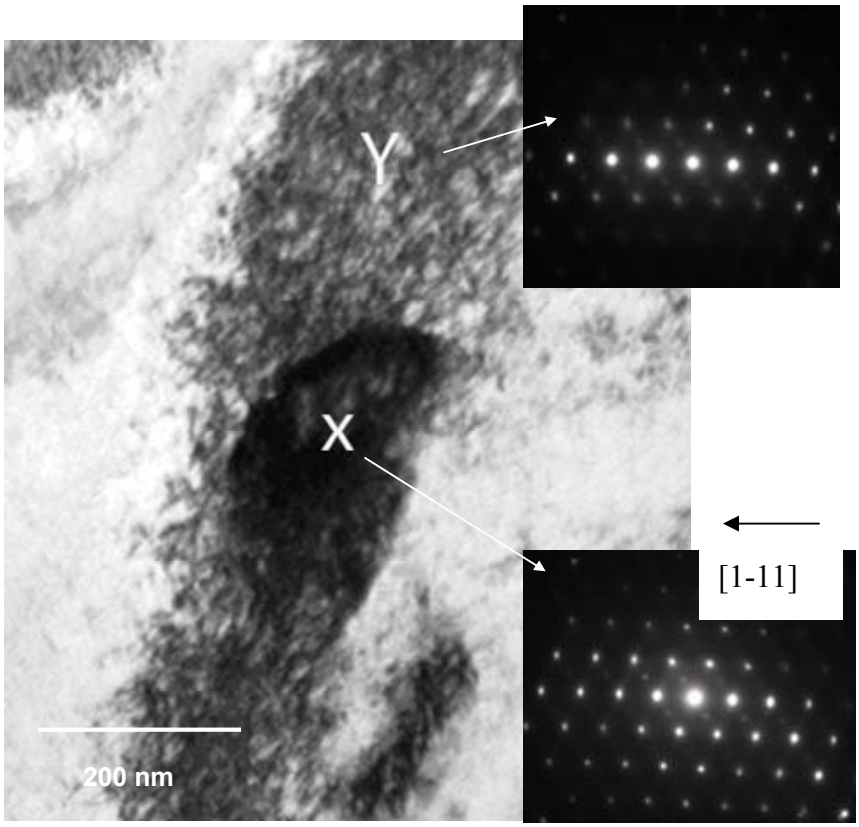

Figure-6.9 Bright Field TEM micrograph depicting CR transformed $L1_0$-ordered grain (labeled X) and the surrounding deformed FCC matrix (labeled Y) after 13° sample tilt about [1-11]. Inset-1 diffraction pattern near [110] zone axis (label Y). Inset-2 diffraction pattern on [110] zone axis (label X).

Microstructural features, such as that delineated by label 'X' in figure-6.9 become discernible after small tilts. The diffraction patterns, insets in the figure have been obtained from regions 'X' and 'Y' for identical acquisition and illumination conditions. The region 'X' is oriented close to a [110] zone axis and $L1_0$-ordered, while region 'Y' is oriented farther off the [110] zone axis

and exhibits weaker superlattice spot intensity. Thus, it appears reasonable to conclude that the region labeled 'X' is a new CR transformed $L1_0$-ordered grain. Emergence of small $L1_0$-ordered domains in the deformed FCC matrix could lead to the weaker superlattice spots in the diffraction pattern from region 'Y'.

The microstructural state after the ordering transformation is complete is dominated by single variant $L1_0$-ordered grains with essentially equiaxed morphology that have formed by CR mode ordering (figure-6.5). The $L1_0$-ordered domains forming by the conventional ordering mode in the interior of the deformed FCC matrix grains are necessary precursors for the polytwin structure and, appear to be consumed by the larger heterogeneously nucleated single variant $L1_0$-ordered grains that form during CR transformation. Hence, it would be reasonable to propose that the texture of the CR-transformed $L1_0$-ordered FePd is dominated by the latter $L1_0$ phase grains, which often exhibit low-angle boundaries with parent-phase FCC-grains. Thus, the interphase interfaces that bound the CR-transformed grain ('X') with respect to the FCC-matrix (e.g. 'Y') are low angle boundaries.

TEM observations in this study identified frequently the low angle boundary nature of interphase interfaces. TEM observations are localized and may not be representative of the entire microstructure. OIM in SEM utilizes EBSPs, can integrate large fields of view and can be simultaneously sensitive to a large number of orientations[68,69.] OIM may be utilized to evaluate the statistical significance of the observations made by TEM[70]. Figure-6.10 is an OIM map of the sample annealed for 0.5 h at 600°C after 97% reduction in thickness in the FCC condition. Colored regions in the map of figure-6.10a are different grains of the deformed FCC matrix (e.g. labels V, W) and white regions are CR transformed $L1_0$-ordered grains (e.g. label U).

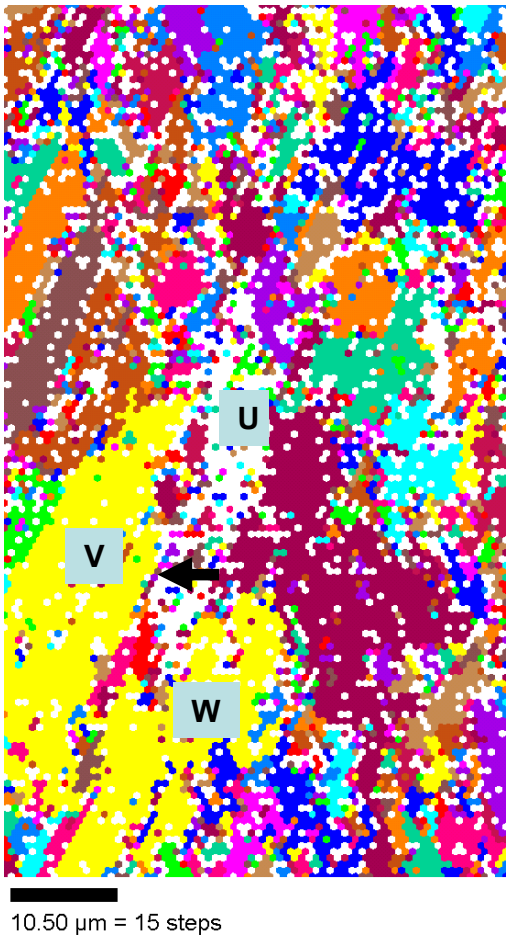

Figure-6.10a

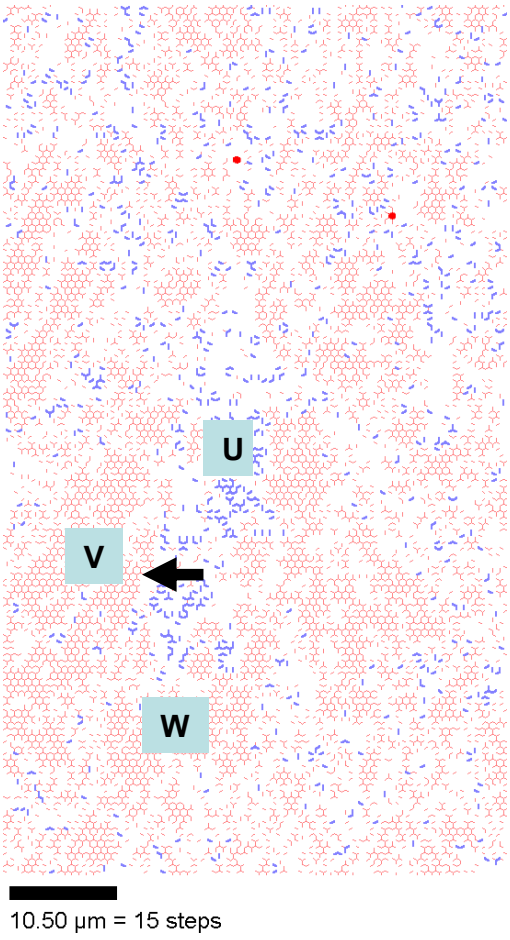

Figure-6.10b

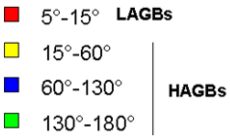

Figure-6.10a OIM map obtained after 0.5 hour at 600°C and reduction in thickness by 97% depicting the deformed FCC grains (multicolored regions). The white regions are CR transformed $L1_0$-ordered grains.

Figure-6.10b OIM map depicting the generation of different types of grain boundaries within the deformed FCC grains and the CR transformed $L1_0$-ordered grains.

It must be noted that the step size of 0.7 µm used for OIM data collection limits spatial resolution in this data set. Nevertheless, the OIM data is consistent with prior SEM and TEM observations.

A large fraction of new CR transformed $L1_0$-ordered grains appear to nucleate and grow on the prior FCC grain boundaries (label U in figure-6.10a). Figure-6.10b shows a map of the locations and distributions of sub - grain, grain and interphase boundaries in this partially CR transformed microstructure. Within the deformed FCC grains a large number of low angle boundaries can be observed (e.g. pink colored boundaries surrounding labels V, W). The darkest shade of red has been assigned to boundaries that have exact 15° rotation across them. Boundaries with rotation angles less than 15° are assigned lighter shades of red, similar to pink or light red boundaries depicted in figure-6.10b.

The large fraction of low angle boundaries within the deformed FCC grains is consistent with recovery processes operating in the deformed FCC matrix during CR-annealing producing a subgrain or mosaic structure. Some high angle boundaries are observed within the CR transformed fraction (label U, figure-6.10b). These are grain boundaries generated by impingement of $L1_0$ ordered grains that have nucleated on different FCC grains and grew. FCC / $L1_0$ interphase interfaces similar to that depicted by the solid arrow in figures-6.10a and 6.10b can also be identified from these OIM maps. The interphase interface labeled with the solid arrow is a low angle boundary (figure-6.10b). Using stereological image analysis the grain boundary misorientation distributions have been determined from the OIM maps. The analysis yielded 76% (± 2%) FCC / $L1_0$ interphase interfaces as low angle boundaries with rotation angle across the boundary more than 5° but less than 15°. About 16% (± 2%) were identified as boundaries with rotation angle of less than 5°. Only 8% (± 2%) of interphase interfaces have been identified as high angle boundaries (rotation angle more than 15°). Thus, a very large fraction of interphase interfaces (≈ 92 % by number fraction) that are low angle boundaries develops as CR reaction proceeds. This statistically significant observation is in good agreement

with the detailed local TEM observations. Such a strong prevalence of interphase interfaces with low angle orientation relationship developing during CR ordering would lead to similar orientations in new CR transformed 'product' microstructures and the deformed FCC phase 'parent' microstructures and is suitable to rationalize a similarity in texture signatures observed before and after CR transformation.

6.2.2 Formation of Defects during CR Transformation

6.2.2.1 Formation of Twins during CR Transformation The TEM micrograph in figure-6.7 depicted the nucleation and growth of $L1_0$-ordered grains at preferential locations in the microstructure. In this partially CR transformed microstructure, the new $L1_0$-ordered grains were seen to be surrounded by FCC regions that contain large density of dislocations. Figure-6.11 is a bright field TEM micrograph obtained from a similarly partially CR transformed microstructure.

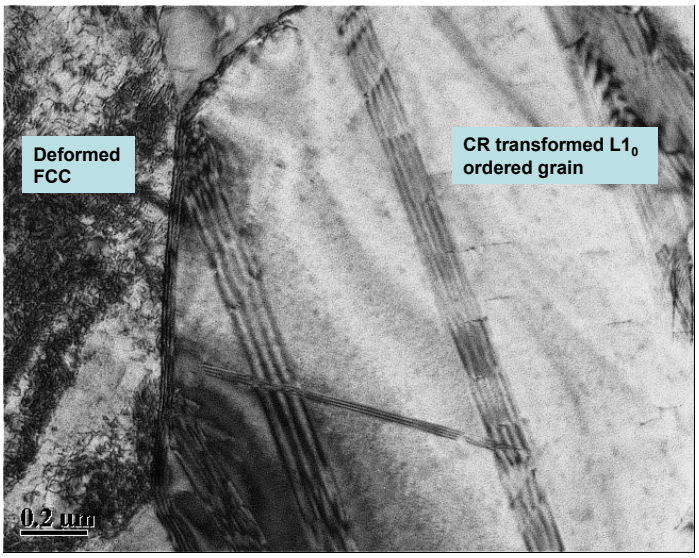

Figure-6.11 Multi-beam bright field TEM micrograph depicting the emergence of stacking faults at the grain boundary.

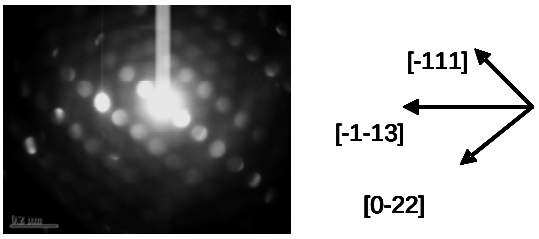

Figure-6.12 Selected area diffraction pattern near a [211] zone axis obtained from the CR transformed grain in figure-6.11

A large density of crystal defects can be seen in front of the CR transformed grain boundary. Fringe contrast possibly associated with stacking fault packets emerging from the grain boundary can also be observed in this bright field TEM micrograph[71]. The contrast changes along the length of the fringe and each change appears to be associated with a step. Figure-6.12 is a SA diffraction pattern obtained from the CR transformed grain depicted in figure-6.11. It can be seen that the CR transformed grain is diffracting with the zone axis being close to [211].

Figure-6.13 is a dark field TEM micrograph obtained using the g = [-111] diffraction vector from the SADP in figure-6.12. It can be deduced from figure-6.13 that stacking faults that give rise to such fringe contrast originate at the grain boundary. Moreover the contrast changes along the length of the fringe confirm the presence of a series of overlapping stacking faults. Figure – 6.14 is a high magnification conventional dark field TEM micrograph obtained using the same diffraction vector as figure-6.13. Dislocation loops (most probably Shockley partials with b = 1/6 <112>) that are bounding these stacking faults and the steps associated with them can also be discerned from this micrograph.

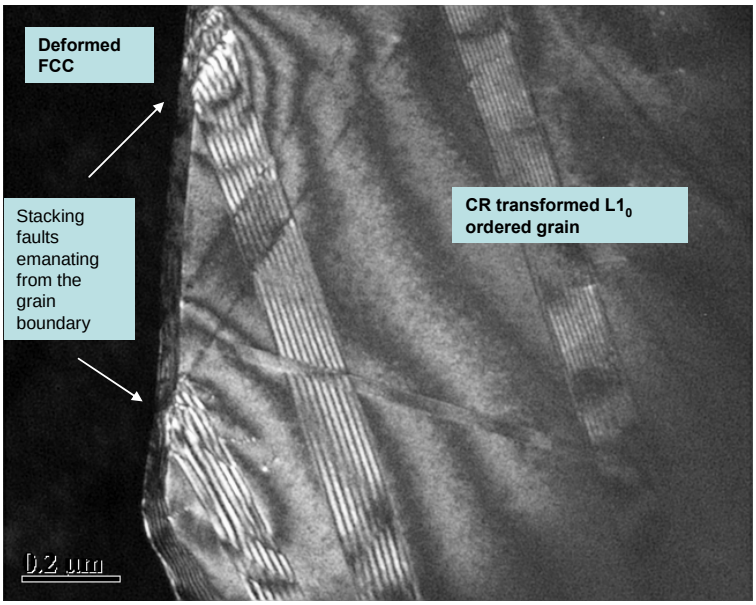

Figure- 6.13 Dark field TEM micrograph depicting the emergence of stacking fault packets from the grain boundary of the CR transformed grain.

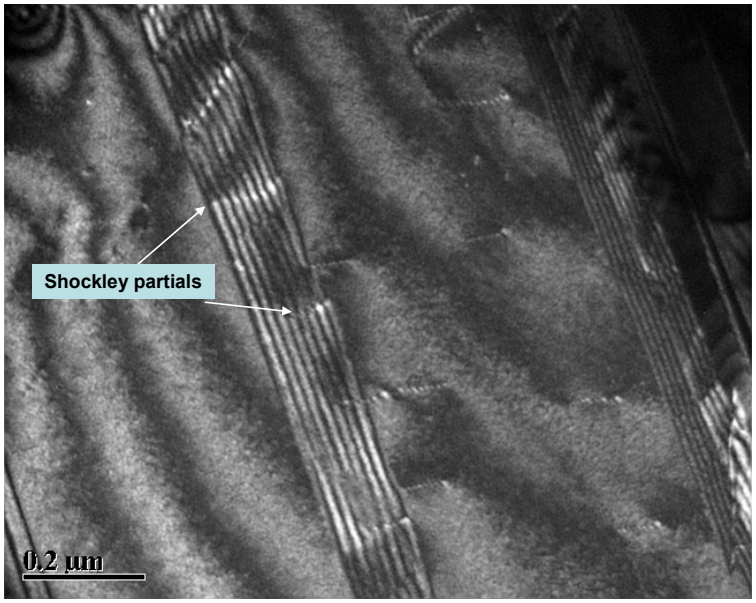

Figure- 6.14 Dark field TEM micrograph depicting the dislocation loops bounding the stacking faults that are emanating from the grain boundary.

Figure-6.15a is a high resolution TEM micrograph obtained from the partially CR transformed microstructure (0.5 hours at 600°C after 97% reduction in thickness via cold rolling in FCC condition). The emergence of a large number of defected twins is also evident in this micrograph (markings 'x', 'y', 'z' all represent twins, the bending of lattice planes near a defect in the vicinity of the twin marked 'x' is depicted in figure 6.15b). Figure-6.16 is a Fast Fourier Transform (FFT) obtained from around the region marked 'x'. The intensity maxima (white spots) depicted in this FFT represent atomic periodicities in the HREM micrograph. From the FFT the relative arrangements of the different {111} in the matrix and twin can be identified. The {111} plane normals in the matrix and twin have been identified. From the arrangement of these plane normals it can be deduced that a 180° rotation across the common <111> can bring the matrix and twin lattices into correspondence. Thus, it seems reasonable to conclude that these are 180° true order twins[72]. Such 180° true order twins have been observed to emerge rather frequently in the partially CR transformed microstructure. Figure-6.17 is an HREM micrograph that depicts one more example of the emergence of these true order twins in the partially CR transformed microstructure (0.5 hours at 600°C after 97% reduction in thickness in FCC condition). These observations thus support the conventional TEM observations that suggest that the twins observed in the partially CR transformed microstructure are defected, consisting of often overlapping packages of SFs.

Figure-6.18 is a multi-beam bright field TEM micrograph depicting the partially CR transformed microstructure. Defected twins emanating from the mobile grain boundary segments are seen to be abundantly present. In addition twin variants nucleating on certain facets of the CR transformed grains are also observed.

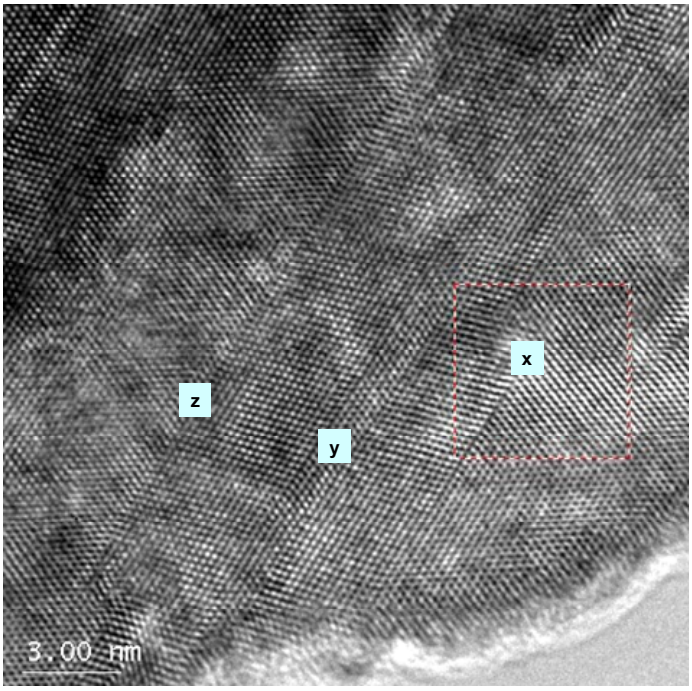

Figure-6.15a HREM micrograph depicting the emergence of a large number of faulted twins in the partially CR transformed microstructure.

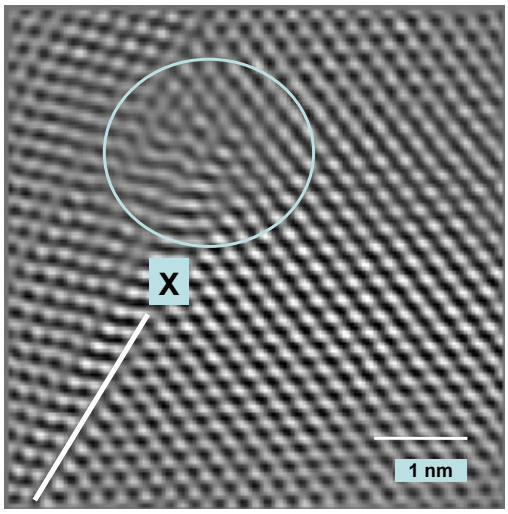

Figure-6.15b HREM micrograph depicting the bending of lattice planes in the vicinity of the twin marked ‘x’ in figure-6.15a

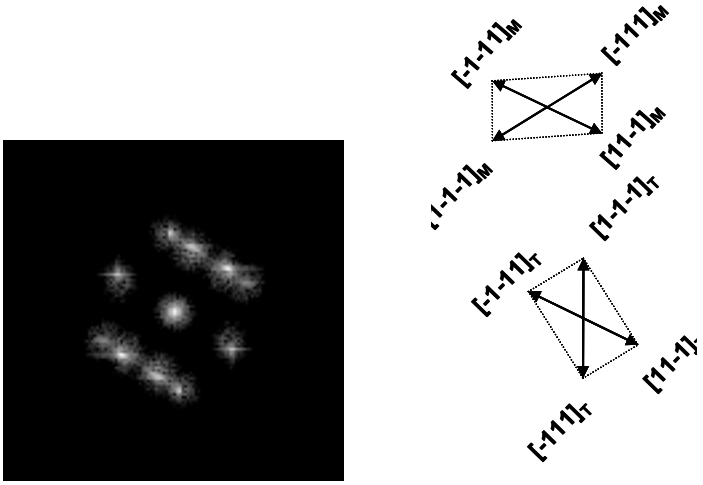

Figure – 6.16 Fast Fourier Transform obtained from the region marked ‘x’ in figure - 6.15a. The twin and the matrix are both diffracting with [101] as the zone axis.

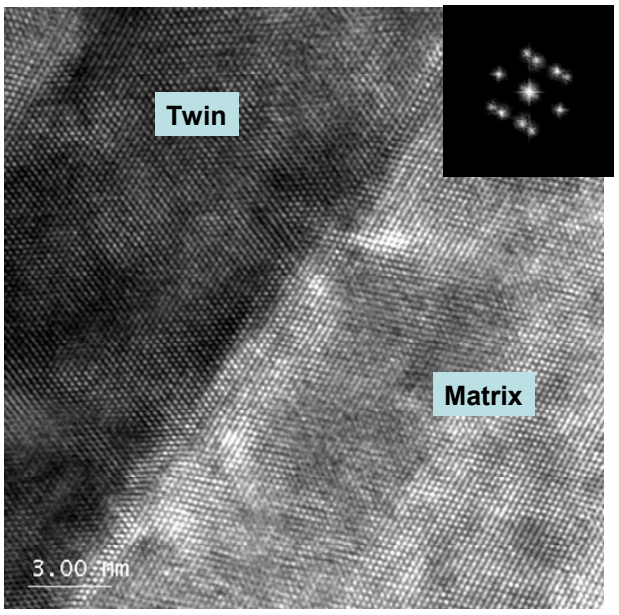

Figure- 6.17 HREM micrograph depicting the twin interface. Inset-FFT obtained from this twinned region.

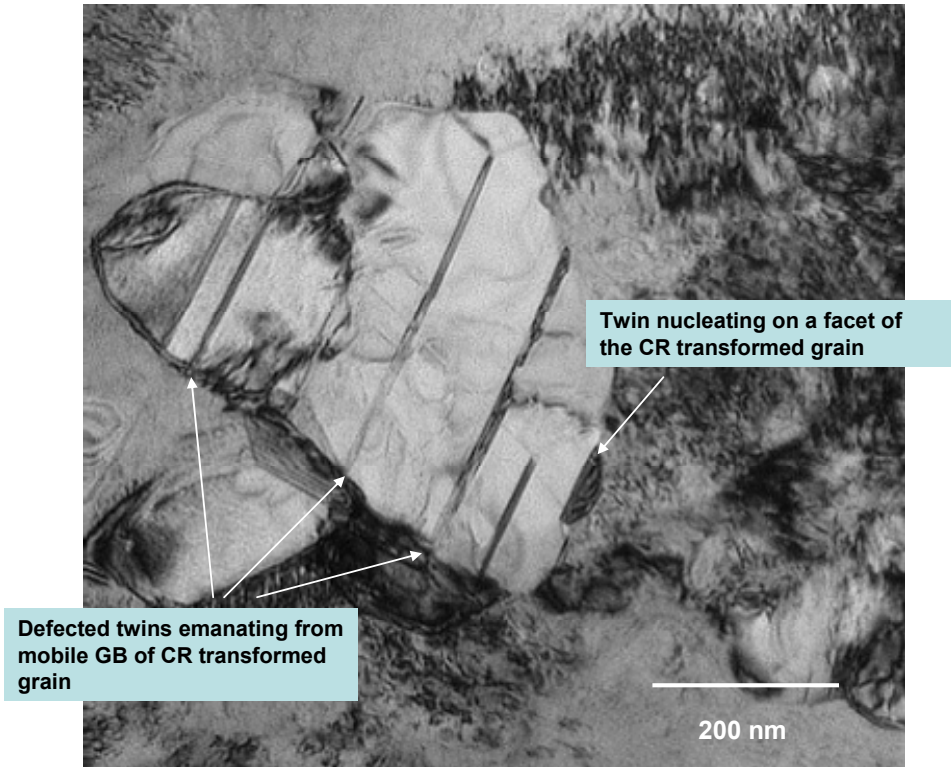

Figure-6.18 Bright field TEM micrograph depicting the generation of different types of twins in partially CR transformed microstructure.

Figure-6.19 is a bright field TEM micrograph depicting the details of the nucleation and growth event on a facet of the CR transformed grain. The diffraction patterns in the inset can be used to identify the interface as a {111} type planar interface. In addition the presence of a 180° rotation across the common <111> can also be discerned from these diffraction patterns. The mirror symmetry across the interface is evident from the orientations of [020] in the CR transformed grain (matrix) and the newly nucleated and growing variant (twin). Such topotectic nucleation[73] and growth events that lead to matrix and twin relationship between CR transformed grains have also been frequently observed in the partially CR transformed microstructure.

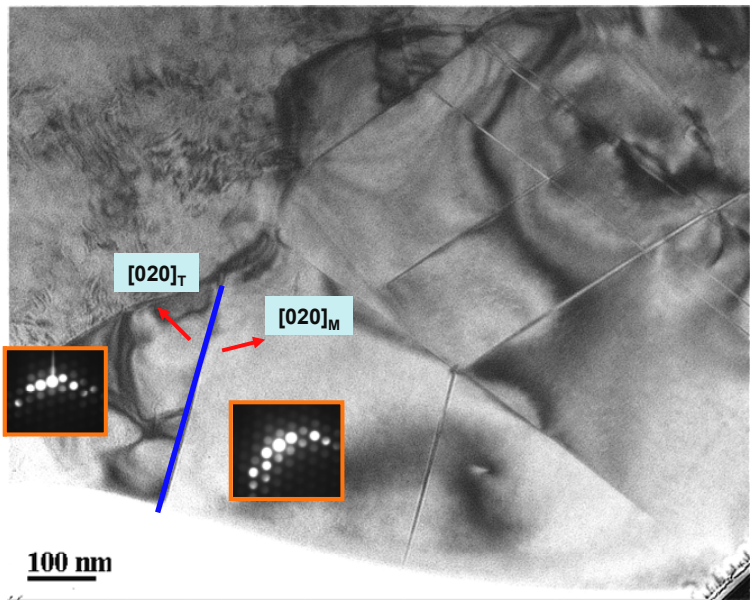

Figure- 6.19 Bright field TEM micrograph depicting the topotectic nucleation and growth of a twin variant in partially CR transformed microstructure.

The defected twins and twins formed due to topotectic nucleation and growth are the most frequently observed morphologies of twins during the CR transformation. In all of the observations made it could be determined that the twins had a 180° rotation relationship across a common <111> and thus were true order twins. The presence of the 120° or the 60° rotation variants (pseudo twins)[72] could not be experimentally confirmed.

6.2.2.2 Formation of Anti-Phase Boundaries during CR Transformation Figure-6.20 is a schematic depicting some of the possible unit dislocations in the FCC phase and unit and partial dislocations in the $L1_0$-ordered phase. Due to atomic ordering only 1/3rd of the unit dislocations from the FCC phase (of the type b = 1/2 <110]) are inherited as unit dislocations in the $L1_0$-ordered phase. The other dislocations (e.g. of the type b = 1/2 <101]) would lead to disruption of atomic order and are referred to as superpartial dislocations. These dislocations would generate

an antiphase boundary[74] (a boundary separating $L1_0$-ordered regions in which the sites that were formerly occupied by Fe atoms are now occupied by Pd atoms and vice-versa).

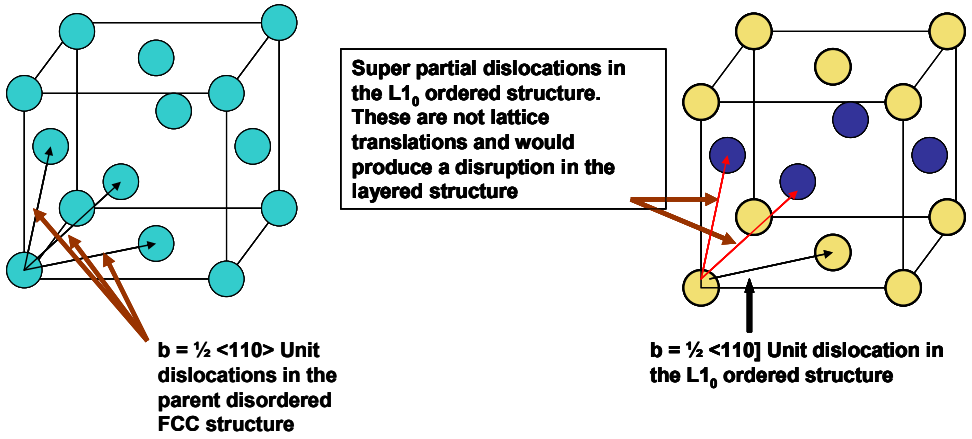

Figure-6.20 Unit cells of the FCC phase and the $L1_0$-ordered phase depicting unit dislocations in the disordered phase and superpartial dislocations in the ordered phase.

The FCC to $L1_0$ ordering in the CR transformation is facilitated by the massive ordering mode. This mode involves the nucleation and growth of single variant $L1_0$-ordered grains at deformation heterogeneities in the deformed parent FCC phase. The conventional ordering mode that involves the 'homogeneous' nucleation and growth of single variant $L1_0$-ordered domains in the FCC matrix competes with this massive ordering mode. From the microstructural observations (e.g. figure-6.5) it can be concluded that the massive ordering mode dominates the microstructural transformation to yield a microstructure consisting nearly entirely of equiaxed grains. Nevertheless, approximately about 5 vol. % of the microstructure transforms by the conventional ordering mode.

Figure-6.21 is a dark field TEM micrograph obtained using the superlattice g = [001] from the region that has transformed by the conventional ordering mode. The illuminated regions are the

$L1_0$-ordered nanoscale domains that have emerged during the FCC to $L1_0$ ordering phase transformation[31]. During their growth these ordered domains would impinge upon each other. Such impingements can lead to the formation of superpartial dislocations (e.g. b = 1/2 [001] or b = 1/6 <211]). These superpartial dislocations would thus separate crystals that have the Fe and Pd site occupancies reversed. The boundary between these crystals would be an antiphase boundary. Since this boundary separates ordered domains that have site occupancies reversed it is also referred to as an antiphase domain boundary (APDB)[2].

Figure-6.22 is a bright field TEM micrograph depicting the generation of APDBs in the fraction that has transformed by the conventional ordering mode. The lamellar polytwin structure attained under the influence of strain minimization is also evident in this microstructure.

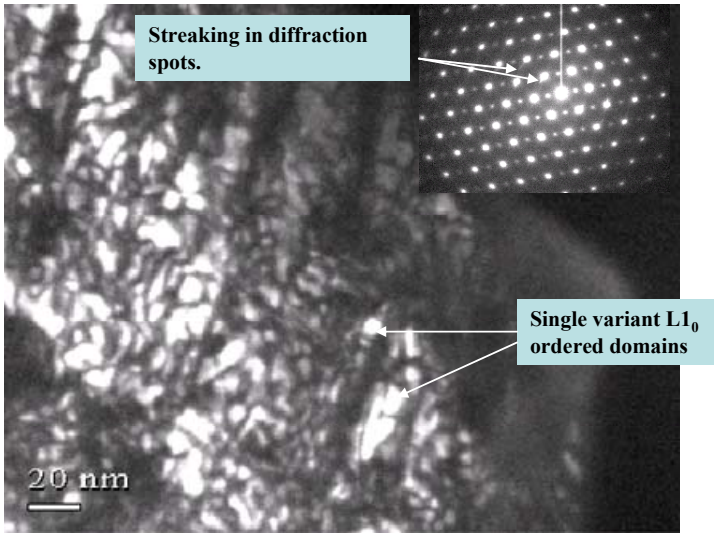

Figure-6.21 Dark field TEM micrograph depicting the ordered domains that emerge during conventional transformation. Inset - diffraction pattern near a [110] zone axis, streaking in the diffraction spots indicates the presence of strain in the microstructure.

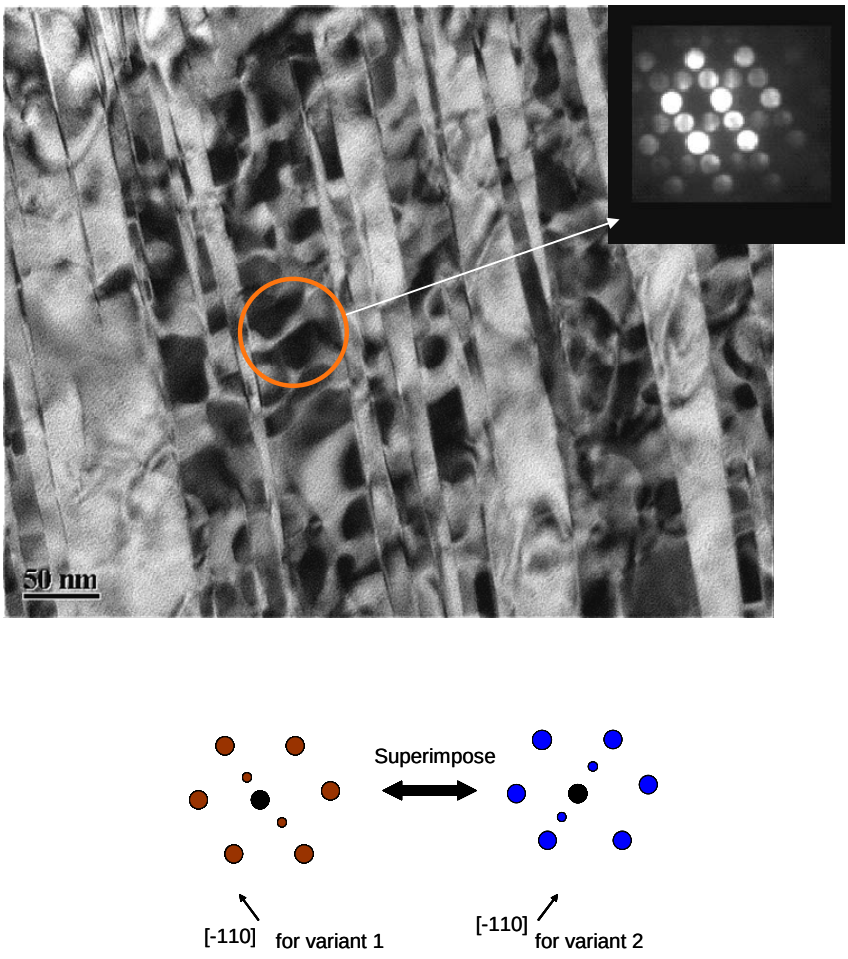

Figure-6.22 Bright field TEM micrograph depicting the generation of APDBs in the conventionally transformed fraction. Inset – diffraction pattern depicting the two ordered variants diffracting with [111] as the zone axis.

APBs have also been observed in the CR transformed grains. Figure-6.23 is a dark field TEM micrograph obtained using the superlattice g = [001] diffraction vector. APBs can also be seen to be emerging from grain boundary of this CR transformed $L1_0$-ordered grain. In addition APBs that are within the grain and do not appear to be connected to any internal surfaces have also been imaged. The mechanisms for the formation of these morphologically different types of APBs segments are most probably different. A growth accidents mechanism leading to formation of superpartial dislocations at the grain boundary seems the most plausible mechanism for the

formation of APBs at the grain boundary. The inheritance of ordinary dislocations from the disordered FCC phase that transform to superpartial dislocations in the $L1_0$-ordered phase seems a reasonable mechanism to be proposed for the generation of the second type of APBs.

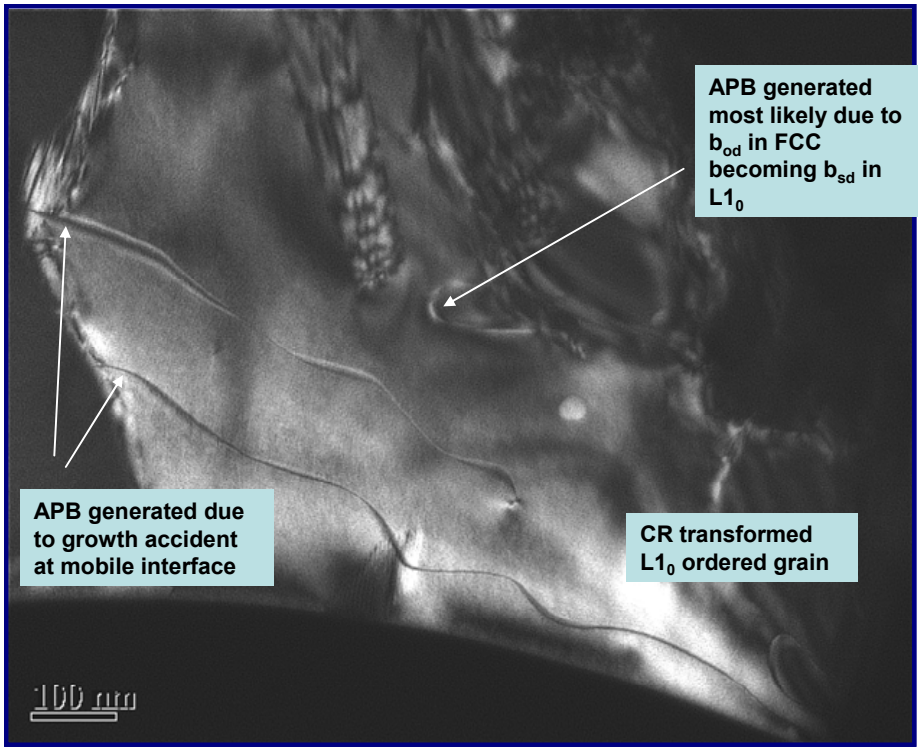

Figure-6.23 Dark field TEM micrograph (obtained using g = [001]) depicting the generation of APBs at the grain boundary and within the CR transformed grain.

6.2.3 Formation of Defects during Grain Growth after CR Transformation

Figure-6.24 is a phi2 constant section of the ODF after 6 hours of annealing after 97% reduction in thickness in the FCC condition. Compared with the texture signature in the fully $L1_0$-ordered CR-transformed microstructure after 4.5 hours (figure-6.6), which was consistent with a broadening and weakening of the cold rolling texture, additional microstructural changes occurred during the additional 1.5 hours (6h-4.5h) of annealing. The texture signature (phi2 =

45° constant section) represented in this section is consistent with twinning becoming a significant mechanism for microstructural transformation. Also, the retention of the cold-deformation / rolling texture observed after the CR transformation is complete (3 hours) is no longer prominent. This is consistent with prior studies in FCC metals that have shown that new orientations emerge as the system tries to maximize the rate of grain growth by forming highly mobile grain boundary segments via twinning[47]. However, it must be noted that the microstructural changes manifest from a comparison of the textures in figures 6.6 and 6.23 are occurring in polycrystalline aggregate of the $L1_0$-ordered phase.

In general the process of twinning leads to the development of new orientations in the coarsening microstructure during latter stages of annealing. The different types of twin morphologies that can emerge during annealing of FCC metals have been reviewed previously. The mechanistic details underlying the generation of these twins have also been elucidated in FCC metals[48,49]. However, the different morphologies of twins and mechanisms for their formation have not been investigated in detail for $L1_0$-ordered FePd that is closely related to the FCC structure.

Figure-6.25 is a bright field TEM micrograph depicting the generation of different types of twins during grain growth of the $L1_0$-ordered phase derived by the CR transformation from the cold deformed FCC phase. Morphologically these twins appear to be similar to the twins observed in FCC metals. It is possible to distinguish lamellae of microtwins and larger twin-related grains (e.g. T,M) in the microstructures that are experiencing grain growth.

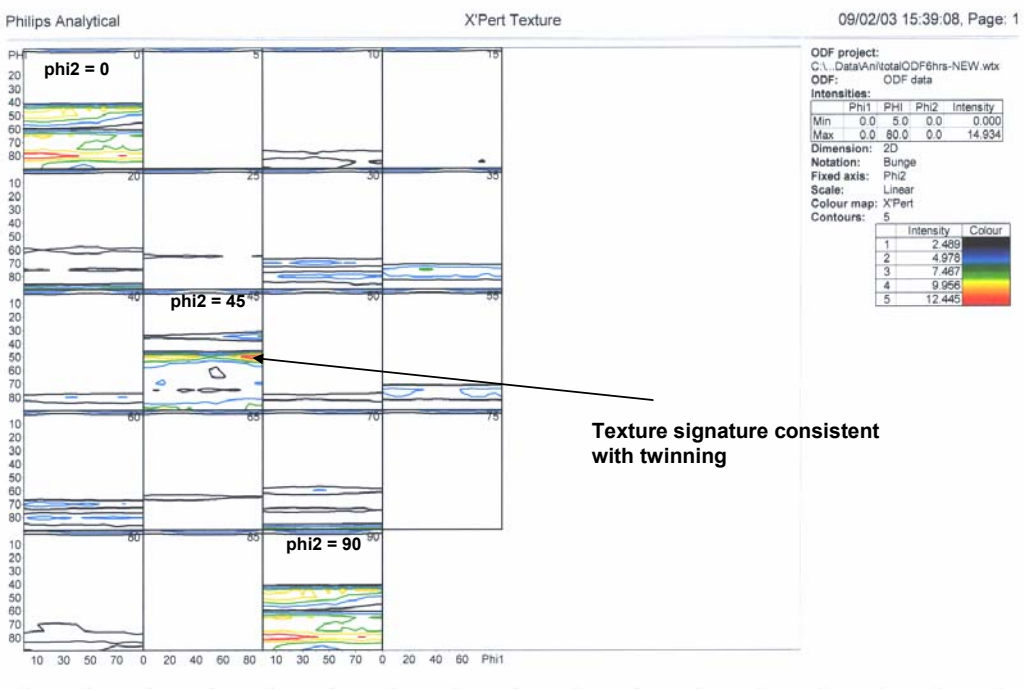

Figure-6.24 A phi2 constant section of the ODF after 6 hours of CR annealing.

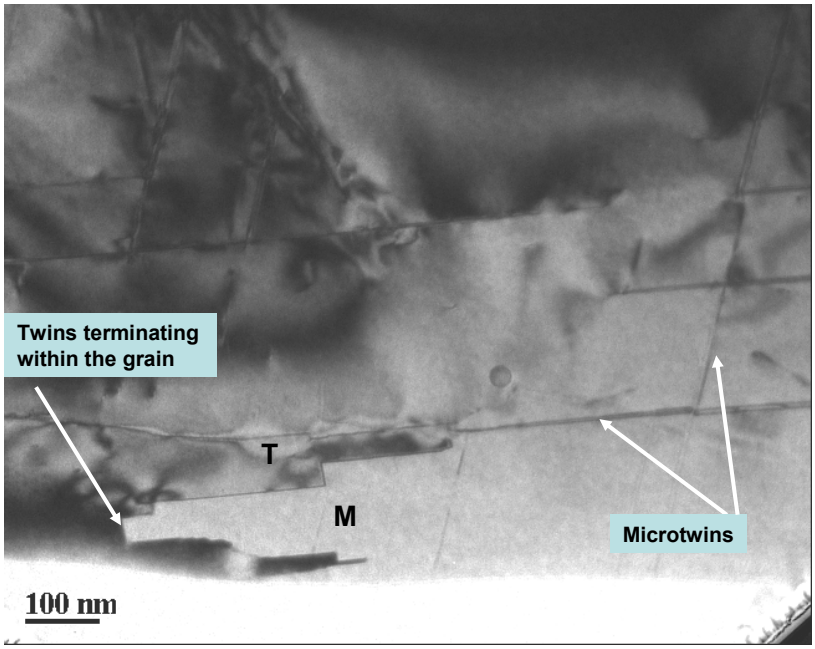

Figure-6.25 Bright field TEM micrograph depicting the generation of different types of twin morphologies during grain growth after CR transformation.

Figure-6.26 is a bright field TEM micrograph depicting microtwin lamellae that have widths of a few nanometers. The bright field TEM micrograph has been obtained such that the diffracting crystal is near a [101] zone axis orientation relative to the transmitted electron beam. The strain associated with crystal defects should produce contrast features in this bright field TEM micrograph (e.g. figure – 6.11). In the absence of such strain associated contrast features it can be concluded that these microtwin lamellae are relatively defect free as compared to the defected microtwins and packages of adjacent SFs observed in partially CR transformed microstructures.

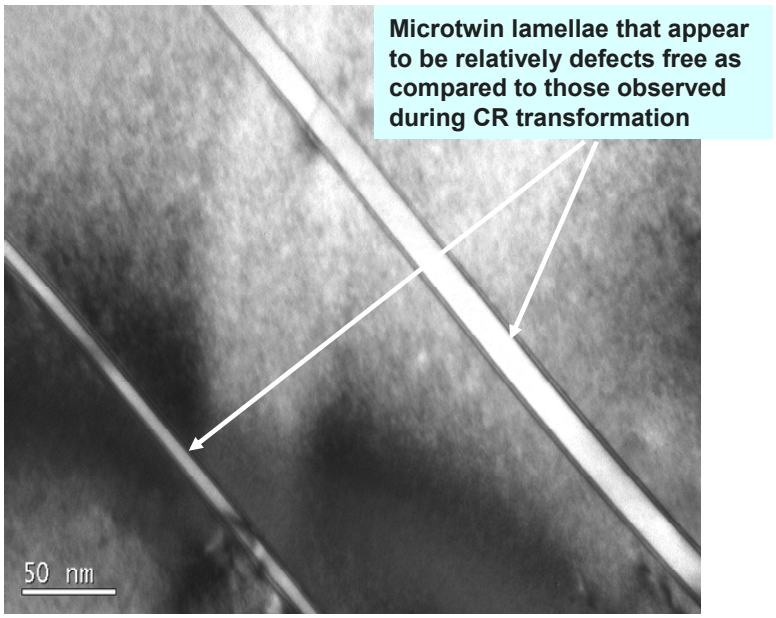

Figure-6.26 Bright field TEM micrograph depicting the generation of twins that have widths of a few nanometers.

Figure-6.27 is a high resolution TEM micrograph depicting the generation of twins during grain growth. Inset is the FFT obtained from the region in the vicinity of the twin interface. The relative orientations of the different <111> and the [-1-10], [110], [001] and [00-1] have been identified in the matrix and the twin. As has been seen in figure-6.15 (HREM of partially CR

transformed microstructure) the presence of defects can lead to bending of atomic planes in the vicinity of the defect. The HREM micrograph in figure-6.27 does show such bent atomic planes (marked with open circles). However the frequency with which such lattice defects are observed appears to be much less as compared to the partially CR transformed sample. This observation is also supported by the low magnification conventional TEM observations of the grain growth microtwins that are largely devoid of any strain contrast from dislocations (figure-6.26), other than the occasional 'growth ledge'. Thus, based on these observations it may be qualitatively concluded that the twins observed to form during grain growth are much less defected as compared to twins observed to form during CR transformation.

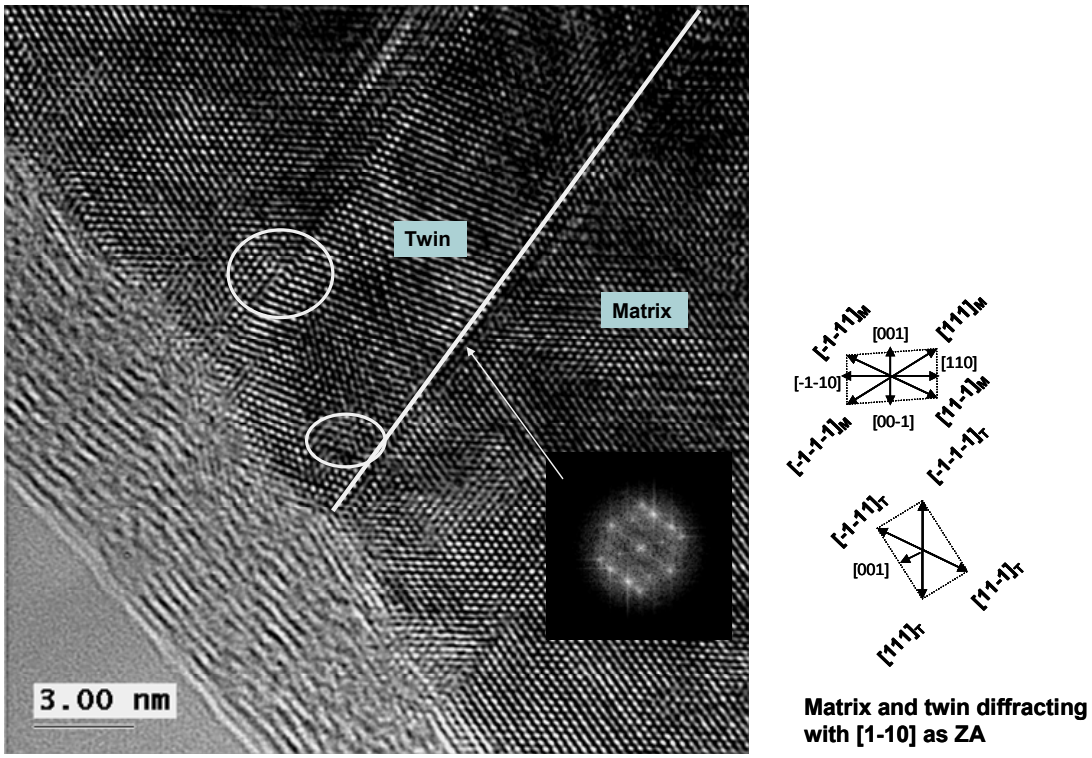

Figure- 6.27 High resolution TEM micrograph depicting the generation of twins during grain growth. Inset-FFT obtained from the regions separated by a coherent twin interface.

Figure-6.28 is a bright field TEM micrograph depicting the generation of octahedral- {111} type ledges in the grain boundaries of the $L1_0$-ordered grains that are undergoing grain growth. During grain growth the atomic attachments would preferentially occur on the close packed {111} ledges. It can be envisaged that such preferential atomic attachments could lead to growth accidents on these octahedral planes. The observation of such {111} ledges is at least consistent with the use of the growth accidents model to explain the process of micro-twinning during grain growth and will be discussed in greater detail in the next chapter.

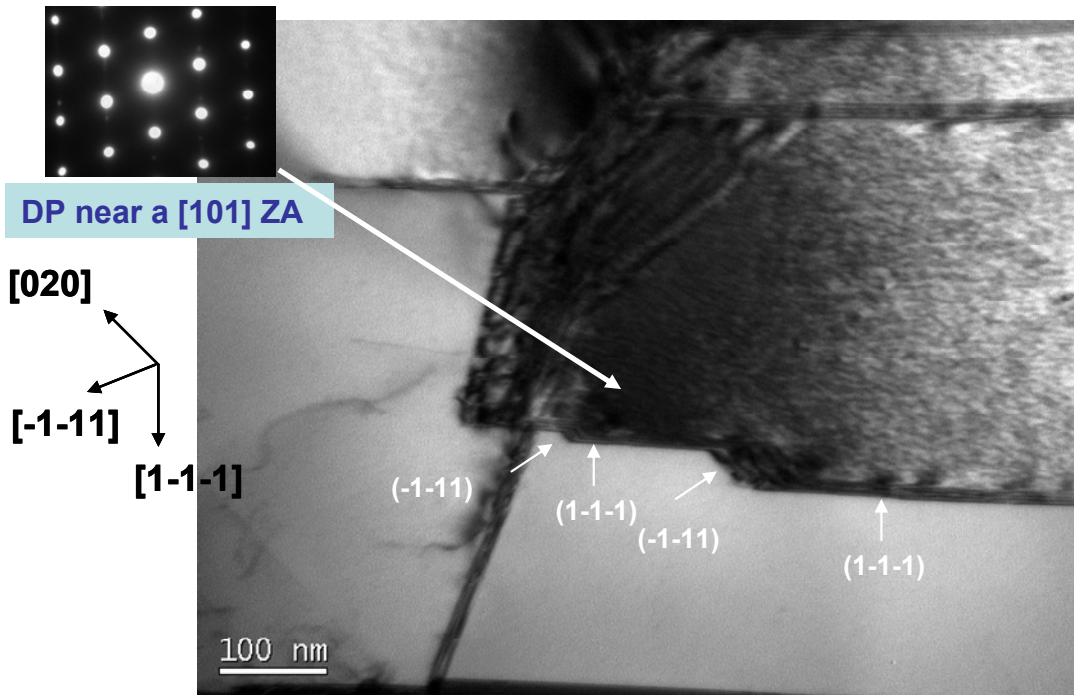

Figure-6.28 Bright field TEM micrograph depicting the generation of {111} ledges on grain boundaries of $L1_0$-ordered grains that are undergoing grain growth. Inset-diffraction pattern near a [101] zone axis obtained from this grain.

Figure-6.29 is a bright field TEM micrograph depicting twin structures observed during grain growth of the CR transformed grains. The SAD pattern in the inset has been taken from this

twinned region. From the SADP it can be deduced that the twin and the matrix are diffracting with [101] as the zone axis. The SADP has also been used to confirm that these are true-order twins of the $L1_0$-ordered FePd. The octahedral {111}-planar interface (with low defect density) separates the twin and the matrix grains. Figures-6.30a and 6.30b are dark field TEM micrograph obtained using the $g = [1\text{-}1\text{-}1]_M$ and $g = [1\text{-}1\text{-}1]_T$ diffraction vectors. These micrographs clearly confirm the matrix and twin relationship between the two grains. The relatively immobile coherent twin boundary segment and the more mobile non-coherent grain boundary segments can also be discerned in these micrographs. Extremely narrow microtwins that have similar orientation as the matrix can also be seen to occasionally shoot out from the non-coherent segment of the twin grain boundary.

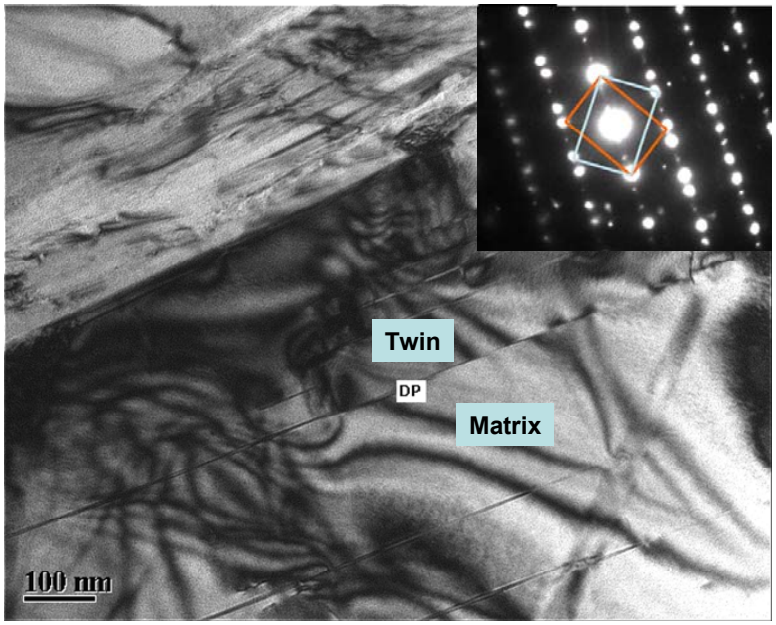

Figure-6.29 Bright field TEM micrograph depicting twins. Inset-diffraction pattern with rectangles marking the diffraction patterns for twin and matrix.

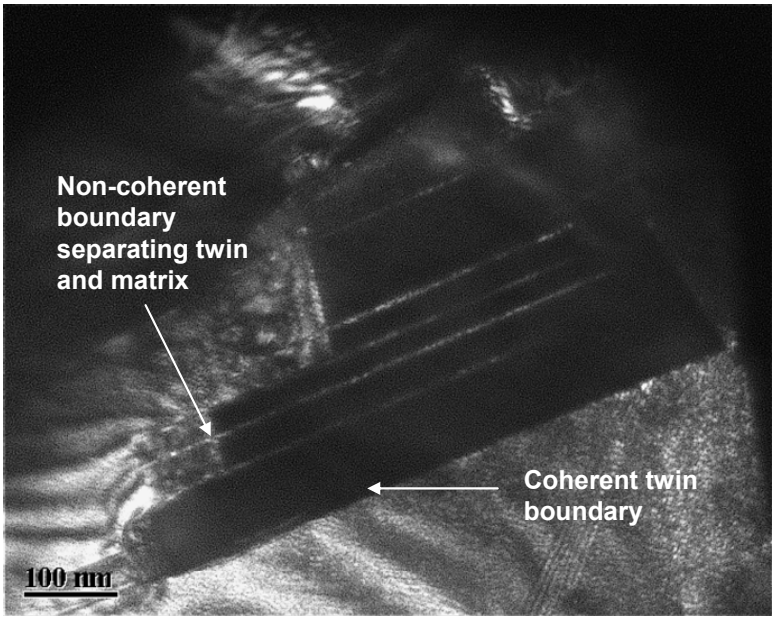

Figure-6.30a Dark field TEM micrograph using g = $[1\text{-}1\text{-}1]_M$

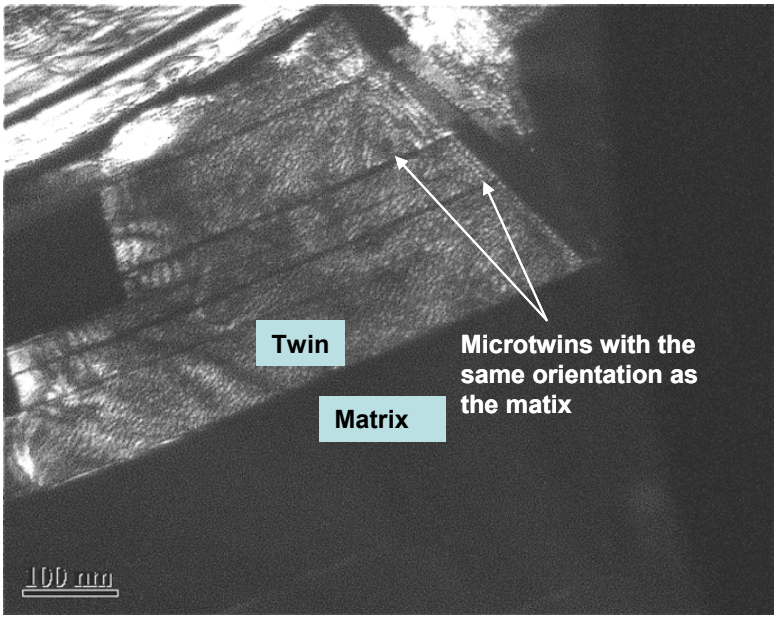

Figure-6.30b Dark field TEM micrograph using g = $[1\text{-}1\text{-}1]_T$

In the next chapter, the emergence of these different morphologies of twins will be rationalized by existing models for FCC metals and their modifications for the FCC related $L1_0$-ordered tetragonal crystal structure of the γ_1-FePd.

6.2.4 Texture Evolution during Grain Growth after CR Transformation

Figure-6.31 is a phi2 constant section of the ODF after annealing for 8 hours after 97% reduction in thickness in the FCC condition. The generation of a prominent texture signature characteristic of twinning is evident in the phi2 = 45° constant section. Additionally the cube texture component ({001} in the rolling plane, <100> in the rolling direction) also starts to appear in the different phi2 constant sections.

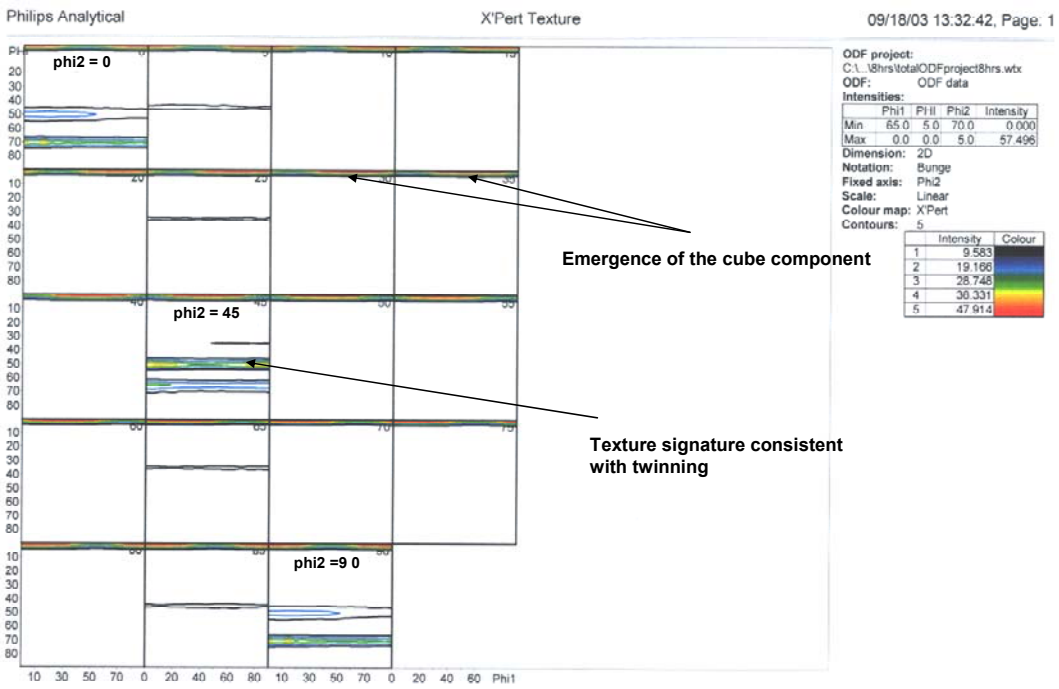

Figure- 6.31 phi2 constant section of the ODF obtained after annealing for 8 hours at 600C after 97% reduction in the FCC condition.

The cube component emerges due to formation of grain boundaries that separate two grains that have a 90° misorientation angle between them. The two crystals can be brought into correspondence by an appropriate 90° rotation with one of the cube axes as the rotation axis. Figure-6.32 is a chart obtained using OIM in the SEM. It has been obtained from the sample that was annealed for 14 hours at 600°C after 97% reduction in thickness in FCC condition. A large fraction of grain boundaries (~ 40% by number fraction) are boundaries with 90° misorientation angle between neighboring grains.

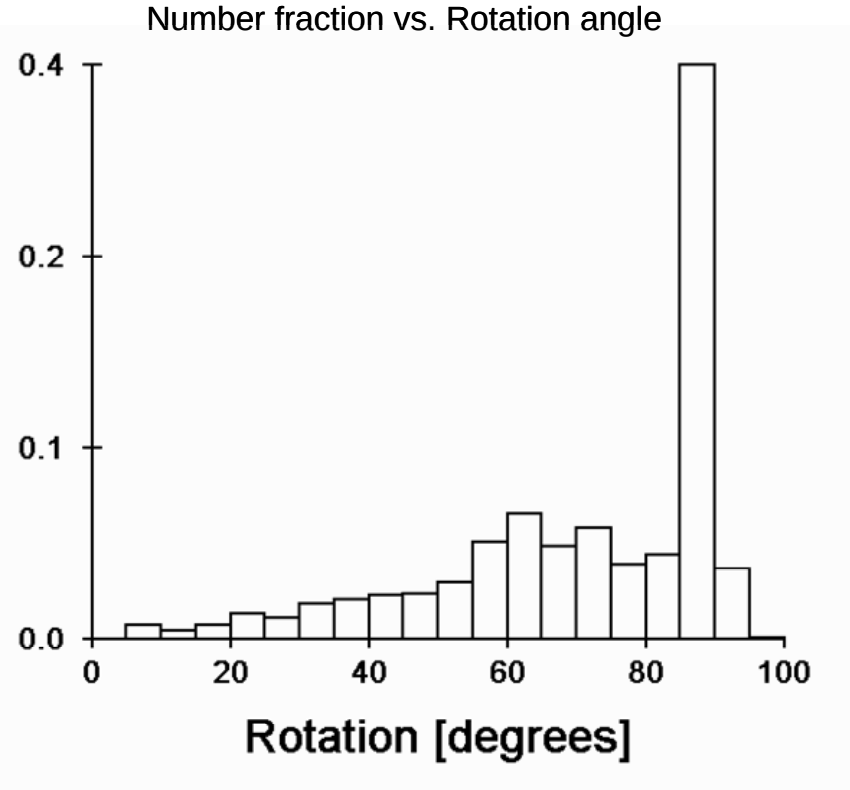

Figure-6.32 Number fraction vs. rotation angle chart obtained for the sample that was annealed for 14 hours at 600°C after 97% reduction in thickness in FCC condition.

Figure-6.33 is a plot of the misorientation distribution function (MDF) obtained using OIM in the SEM for the same sample (14 hours at 600°C). The MDF in figure-6.33 is an intensity plot (using number fraction) of the grain boundaries with different misorientation angles across them. The misorientation angle for each MDF plot is indicated in the upper left corner. Three axes ([001], [100], [110]) that could potentially form the rotation axes are depicted as the three vertices of the MDF triangle. All axes that lie in between these three orientations ([001] and [100]; [001] and [110] separated by 90°, [100] and [110] separated by 45°) can be also be depicted in this MDF triangle.

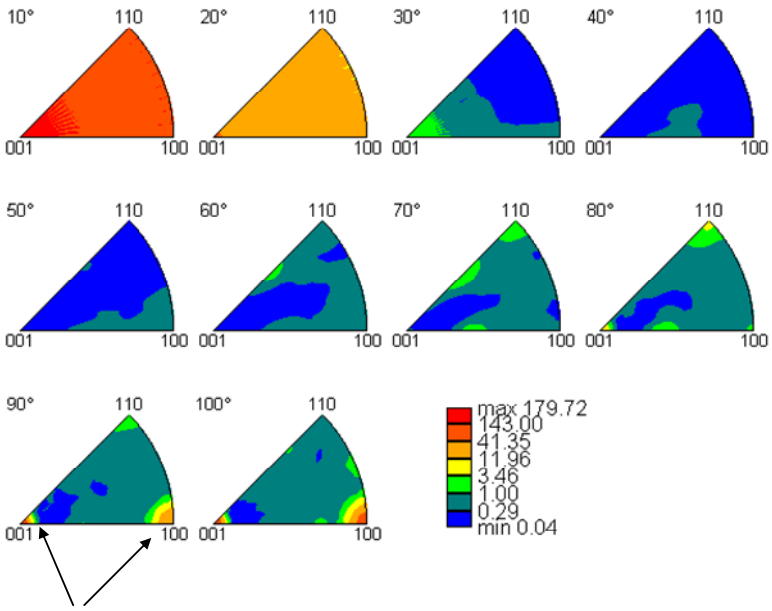

Figure-6.33 MDF representation of the sample annealed for 14 hours at 600°C after 97% reduction in thickness in FCC condition.

From the rotation angles chart it can be deduced that there is a large number fraction (~40%) of grain boundaries that have a 90° misorientation across them. From the MDFs it can be deduced that the 90° misorientations occur with the cube axes being the rotation axes. Thus, the presence of the cube component as a dominant texture component can be established in this sample.

The results of texture evolution obtained using two completely different techniques (X-ray diffraction and OIM) are seen to be comparable and mutually consistent. In addition, the results obtained using both these techniques are also statistically significant. Thus, from these observations it seems reasonable to conclude that the cube component becomes dominant during the microstructural transformation stage accomplished by grain growth.

In the presence of such overwhelming preference exhibited by the system for the formation of a certain crystallographic texture, it seems unreasonable to postulate that the process of grain growth in these CR transformed microstructures would be amenable to a simple 'capillarity' motivated analysis. The underlying assumption in capillarity analysis that all grain boundary segments would have the same mobility and self similarity would be maintained as grain growth progresses does not seem to be valid in this case. It appears as though additional criteria to those of the simple surface tension model (as considered in capillarity analysis)[75] dictate the microstructural transformation. In the next chapter analogies between the coarsening behavior of the polytwin lamellae obtained during conventional transformation and the grain growth observed after CR transformation will be highlighted. Based on a misfit strain energy argument, similar to the polytwin microstructure, the emergence of the cube component would be rationalized.

6.3 COLD DEFORMATION IN $L1_0$-ORDERED γ_1 FePd WITH EQUIAXED MICROSTRUCTURE

Previous studies have attempted the cold deformation of the equiatomic $L1_0$-ordered alloy with the polytwin microstructure[58]. Cold deformation of this alloy with the equiaxed microstructure has not been attempted before.

One of the main objectives of this study is to attempt deformation of the $L1_0$-ordered equiaxed microstructure by cold rolling. As has been described in the previous experimental procedures chapter, CR transformation has been utilized to achieve an $L1_0$ -ordered equiaxed microstructural state before cold deformation is attempted. Figure-6.34 is a SEM micrograph obtained in the crystallographic orientation sensitive BSE mode depicting the microstructure after the CR annealing.

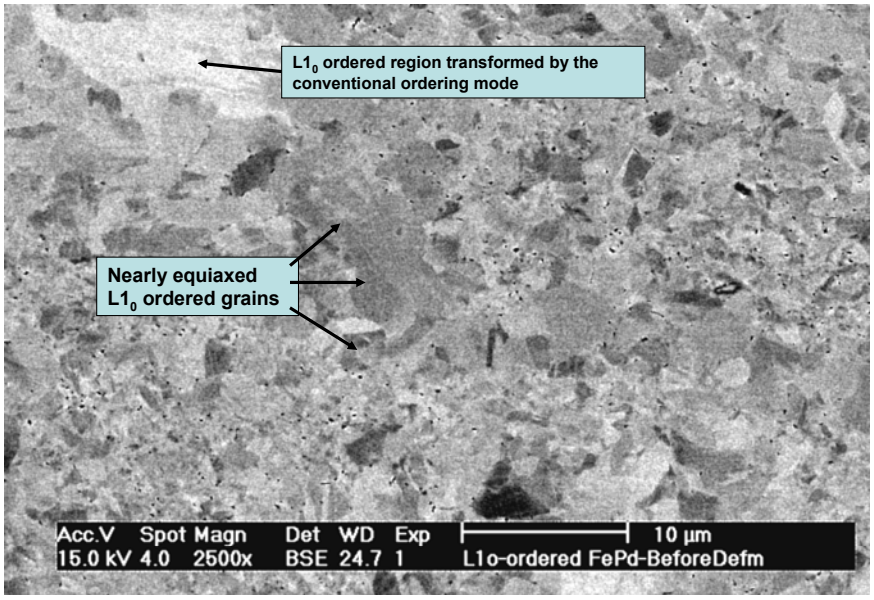

Figure-6.34 SEM micrograph in the BSE mode depicting the microstructure in the CR transformed condition before deformation.

As can be deduced from this micrograph a large fraction (~90% area fraction) appears to consist of nearly equiaxed $L1_0$-ordered grains. The formation of a well developed lamellar polytwin microstructure is not evident in this orientation sensitive micrograph. Thus, the remainder fraction must be comprised of the conventionally transformed microstructure that consists of $L1_0$-ordered orientation variant domains.

Figure-6.35 depicts symmetric θ-2θ scans obtained using X-ray diffraction at different stages of cold rolling in the nearly equiaxed $L1_0$-ordered microstructural state as depicted for example in figure-6.34.

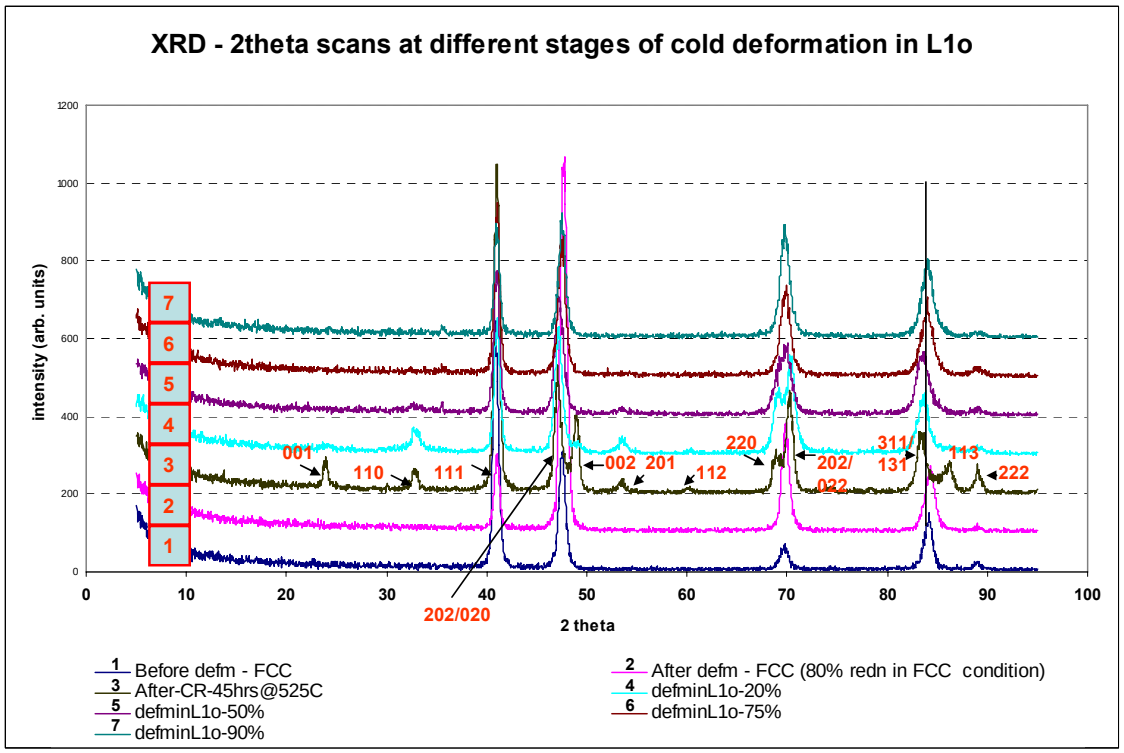

Figure-6.35 Symmetric θ-2θ scans obtained using XRD at different stages of cold rolling in the $L1_0$ ordered condition.

For comparison, equivalent XRD scans have been obtained for the undeformed and deformed FCC Fe-Pd solid solution and are included in figure-6.35. Scans – 1 and 2 have been obtained from the starting disordered undeformed and the disordered deformed FCC (γ) FePd phase respectively. Scan-3 has been obtained from the CR transformed $L1_0$-ordered microstructure depicted in figure-6.34. The presence of an ordered phase can be discerned from the emergence of superlattice diffraction peaks, such as the 001, 110 etc. The c/a ratio (0.967) calculated for this state is also close to the equilibrium c/a ratio for the $L1_0$ ordered phase (0.966) [2]. This data set in tandem with the micrograph in figure-6.34 establishes the starting microstructural state as $L1_0$-ordered, largely consisting of equiaxed grains. Deformation by cold rolling in such an equiaxed $L1_0$-ordered microstructure has not been attempted before.

Scans-4 through 7 have been obtained for increasing amounts of cold rolling strain (20%,50%,75% and 90% reduction in thickness respectively). The decrease in the intensity of superlattice peaks (e.g. 110) and the disappearance of some other superlattice peaks (e.g. 001) after 20% reduction in thickness is evident from scan-4. It can be observed that the peak positions of the various diffraction maximum are also changing as cold rolling progresses (e.g. the maximum observed for the peak 311/131 after CR is complete (scan-3) does not align with the peak maximum observed for the 311/131 peak after 20% reduction in thickness (scan-4)). With increasing thickness reduction in cold rolling the peak splitting due to the tetragonality of the $L1_0$-ordered unit cell is also no longer evident (e.g. 311/131 and 113 peaks in scans-5 through 7). The peaks appear to be broadened into one peak that might have contributions from all different diffracting planes within the same family. A comparison between scan-7 (90% reduction in thickness in $L1_0$-ordered condition) and scan-1 (starting disordered FCC (γ) FePd) reveals similarities such as absence of superlattice peaks, peak maximum positions that are

comparable and apparent absence of split peaks. Thus, it seems tempting to suggest that the process of cold rolling in the $L1_0$-ordered phase after 90% reduction in thickness leads to a microstructural state that has similar X-ray diffraction characteristics as the disordered FCC phase.

The strain introduced in the microstructure during cold rolling would manifest in the form of broadening of the diffraction peaks. In addition it could also change the peak maximum positions[76,77]. In the presence of sufficient peak broadening due to strain, the peak splitting typical of the tetragonal $L1_0$-ordered structure cannot be discerned any longer.

To measure c/a ratios as deformation progresses, the prominent 200/020 and the 202/022 peaks have been used. The peak maximum positions for 200/020 and 202/022 have been measured. Interplanar spacings d for (200 / 020) and (202 / 022) have been computed using Bragg's law

$$2d\sin\theta = \lambda \qquad 6.1$$

The d spacing is related to the lattice parameters a and c of the $L1_0$-ordered phase by the following relation.

$$1/d^2 = [(h^2+k^2)/a^2\ ] + [l^2/c^2]. \qquad 6.2$$

The lattice parameter a has been determined using the 200/020 peak. Thus, in the above equation for given {hkl} (e.g. (202)) the lattice parameter c is the only unknown. It has been determined for different processing conditions.

Figure-6.36 is a plot of the variation in the c/a ratio as deformation processing progresses to increasing reduction in thickness by rolling. The c/a ratio has a value of unity in the undeformed and deformed FCC phase (scans-1 and 2). It has a value of 0.967 in the completely CR transformed condition. This value is very close to the equilibrium c/a ratio of 0.966. Thus, the CR transformation produces a microstructure consisting entirely of the $L1_0$-ordered phase. The

c/a ratio changes from 0.967 (in the CR transformed, $L1_0$-ordered undeformed condition) to 0.989 (in the cold rolled to 90% reduction in thickness in the $L1_0$-ordered condition).

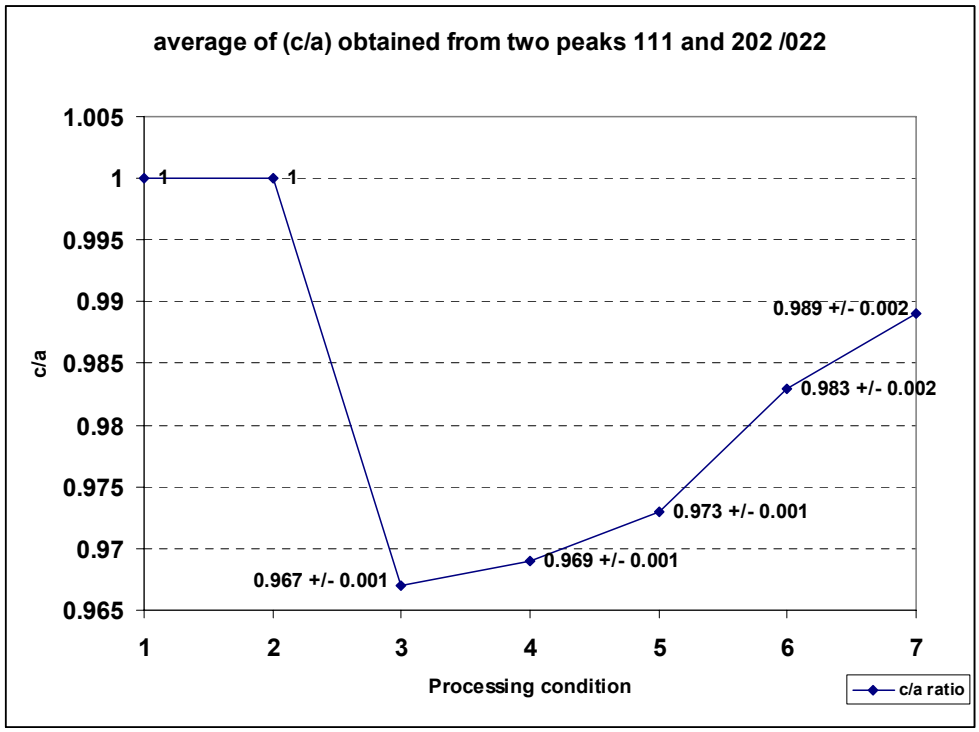

Figure-6.36 Variation in c/a as a function of processing condition. The legend describes each of the processing steps.

Since the c/a ratio is a direct measure of the long range order parameter[29], from these observations it seems reasonable to conclude that the process of cold rolling in the $L1_0$-ordered condition generates a microstructure that has a lower long range order (LRO) parameter than the equilibrium $L1_0$-ordered phase. 'Mechanical disordering' is a term that has been frequently used in the literature, when describing such lowering of LRO parameter during deformation of other

ordered alloys[78]. However, it has to be clarified that the similarity of the XRD scans of the heavily cold-deformed $L1_0$-ordered phase to that of the cold-deformed FCC imply a phase transformation, hence, the term 'mechanical disordering'. According to the XRD scans the cold-deformed states prior to annealing appear to be quite similar for the cold-rolled FCC and the cold rolled $L1_0$-ordered Fe-Pd. However, it is important to note the differences in the processing routes and thus the possible mechanisms by which this disordered FCC-like states have been attained. The process of cold deformation would be facilitated by dislocations (glide as well as possibly twinning). These dislocation motions are highly crystallographic. As against this, thermally induced disordering would be facilitated by motion of vacancies which is much more stochastic in nature. These differences have been discussed in greater details in the next section and their effects on the subsequent microstructural transformation during annealing have also been explored.

Microstructure sensitive magnetic properties, such as coercivity, can also be used to monitor the change in the LRO parameter in Fe-Pd[79] as deformation by cold rolling proceeds. Figure-6.37 is a plot that depicts the variation in coercivity at different stages of cold rolling. An increase in coercivity from 57 Oe to 456 Oe (+/-20 Oe) can be observed after CR annealing is complete and the CR transformed microstructure has undergone significant grain growth. This observation is in agreement with previous studies that report the attainment of the highest coercivity state when the fully $L1_0$-ordered microstructure is attained[79]. An increase in coercivity to about 649 Oe is observed after 20% reduction in thickness. Further cold rolling to larger reduction leads to a decrease in the coercivity. However, even after 90% reduction in thickness the coercivity is ~200 Oe (nearly 10 times that observed in the disordered, undeformed FCC phase).

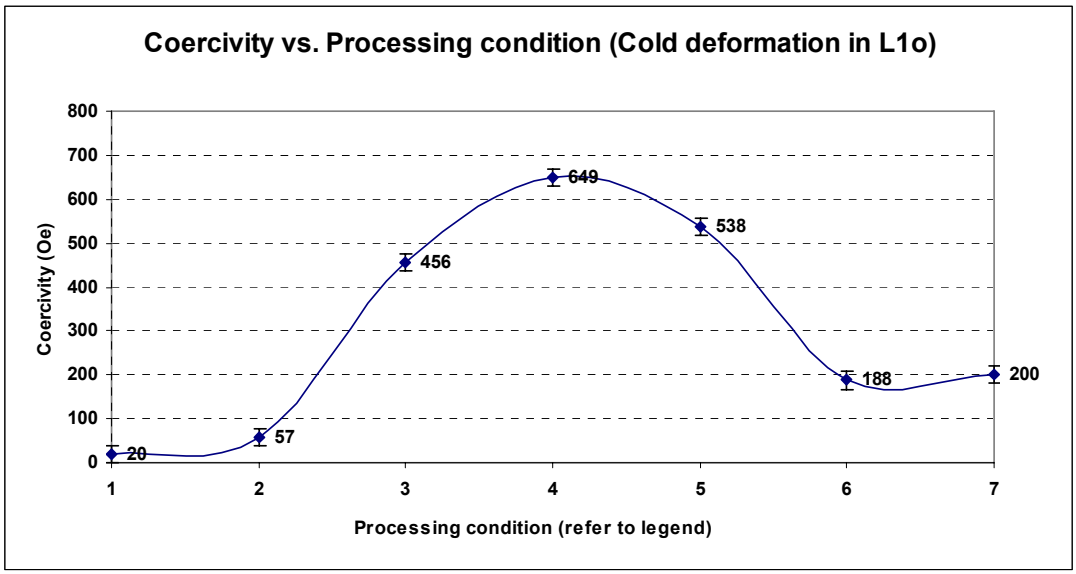

Figure-6.37 Variation in coercivity as a function of processing condition. The legend describes each of the processing steps.

Thus, after heavy cold deformation in the $L1_0$-ordered condition the microstructure sensitive magnetic property exhibits a value significantly different than that expected for the disordered FCC phase. Thus, these magnetic property measurements seem to conflict with the implication of a mechanically induced complete disordering phase transformation that may be deduced from X-ray diffraction experiments. However, the reduction in coercivities from the peak after 20% cold-rolling reduction for the larger amounts of cold-deformation is consistent with decrease of LRO parameter deduced from XRD. Nevertheless, the magnetic property differences suggest that it would be reasonable to conclude that the $L1_0$-ordered deformed microstructure is significantly different from the disordered FCC phase.

TEM observations have been conducted to elucidate the evolution of the deformation microstructure. Figure-6.38 is a bright field TEM micrograph depicting the deformed microstructural state after 20% reduction in thickness in the $L1_0$-ordered condition. Inset is the

diffraction pattern obtained from this deformed microstructure. The presence of superlattice spots, such as the 001, in the diffraction pattern indicate the presence of an $L1_0$-ordered structure. Arcing in the diffraction spots due to strain in the microstructure is also evident. The dark regions in the bright field micrograph appear to be contrast features associated with dislocations and other crystal defects / imperfections introduced during cold deformation. A large density of dislocations and other crystal imperfections is observed in the microstructure after 20% reduction in thickness in the $L1_0$-ordered condition.

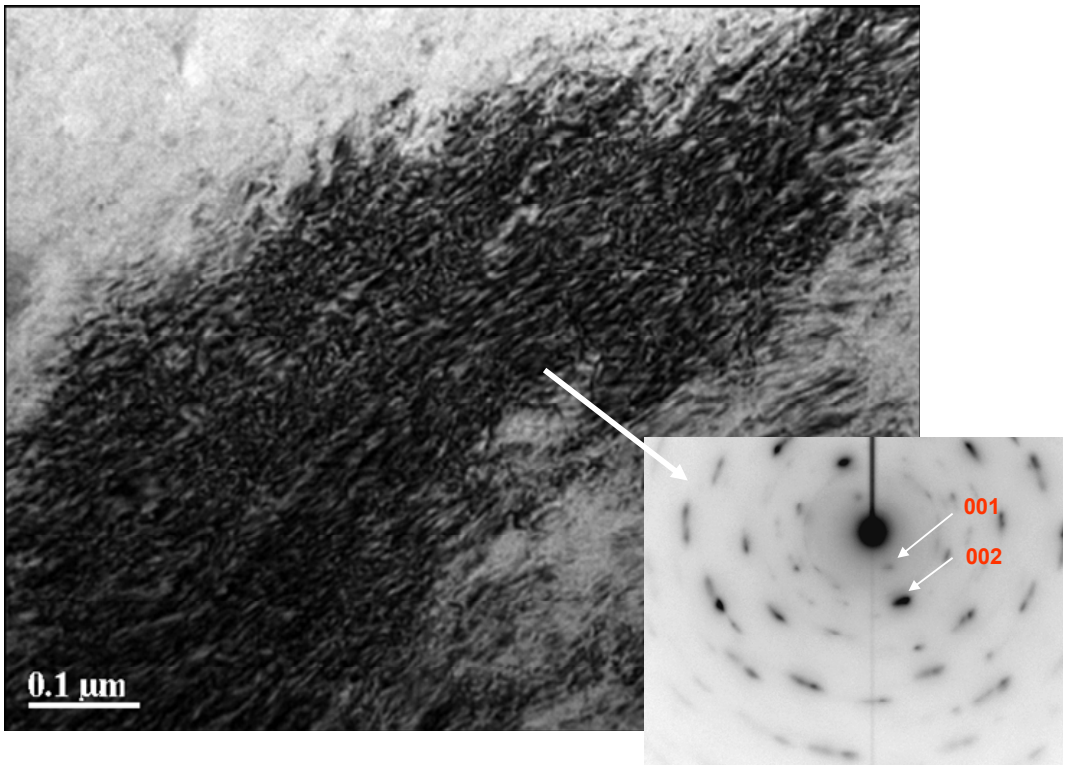

Figure-6.38 Plan view bright field TEM micrograph obtained from the cold rolled to 20% reduction in thickness sample. Inset diffraction pattern obtained from the deformed microstructure.

Figure-6.39 is a plan view bright field TEM micrograph depicting the deformed microstructural state after 90% reduction in thickness in the $L1_0$-ordered condition. Inset is the diffraction pattern obtained from this deformed microstructure. In this diffraction pattern obtained from a large field of view of the microstructure (~40μm in diameter) extremely weak, diffuse rings corresponding to the superlattice reflections, such as 001,110, are observed. Thus, the presence of an $L1_0$-ordered crystal structure even after heavy plastic deformation can be discerned from this observation. The intensity in the 111 as well as the 200 reflections appears to be higher in certain sectors of the ring. This would indicate the development of a texture as cold deformation progresses. This plan view TEM micrograph is not sufficient to comment on the development of the potential 'pan-cake' like structure during cold rolling. Nevertheless, qualitatively it can be concluded that the contrast features in this bright field micrograph do depict some spatial variations that could be associated with different density distributions of defects in the microstructure that have been introduced during cold rolling and represent a section through a deformation cell-structure. Given the extremely large defects density observed after 20% (and for 90%) reduction in thickness samples, attempts to image individual dislocation segments and to identify their characteristics have met with limited success. Thus, direct experimental physical insight into the preferred modes of deformation during cold rolling is currently lacking. Nevertheless, indirect measurements (such as X-ray diffraction and vibrating sample magnetometry) in addition to direct observations (such as TEM observations of the annealing phenomena discussed later) could provide pointers towards these underlying mechanisms of deformation. These potential mechanisms that would lead to 'mechanical disordering' observed in this study will be discussed in greater detail in the next chapter.

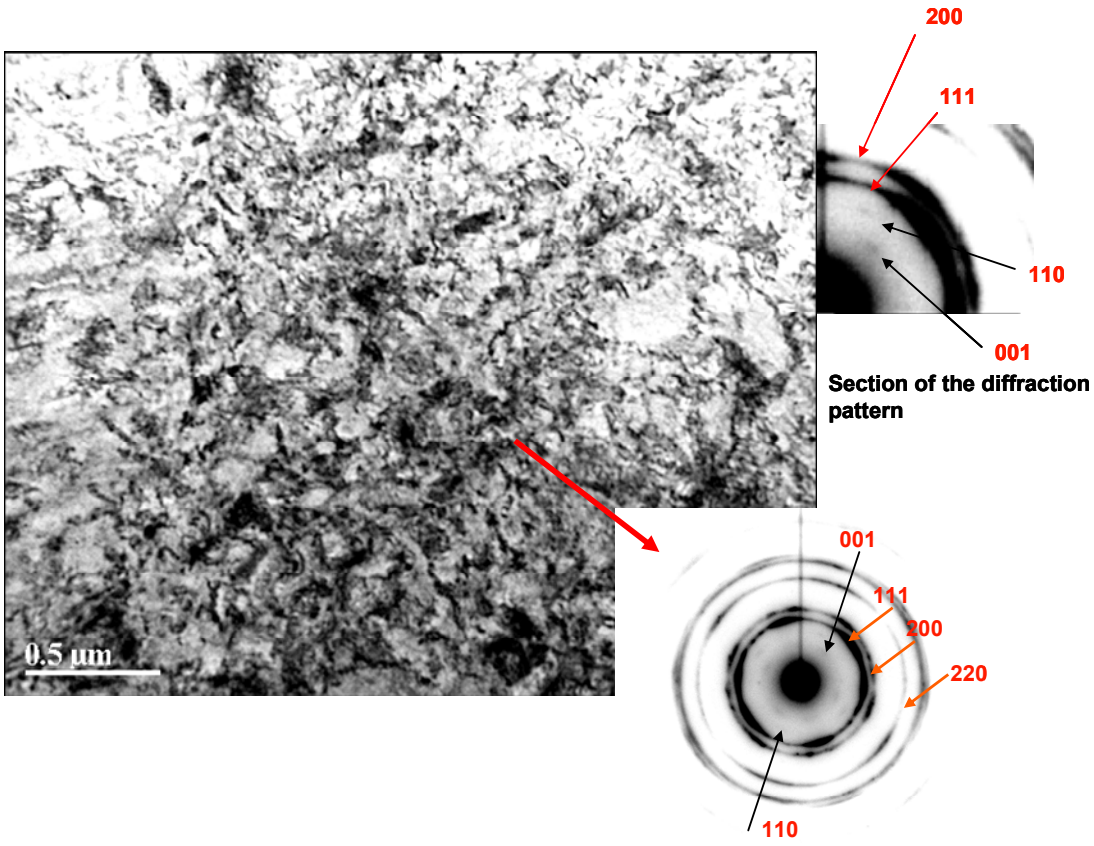

Figure-6.39 Plan view bright field TEM micrograph depicting the microstructure after cold rolling to 90% reduction in thickness in the $L1_0$-ordered condition. Inset-diffraction pattern obtained from this cold deformed microstructure.

X-ray diffraction has also been used to understand texture evolution during cold rolling of the $L1_0$-ordered equiaxed microstructure. Figure-6.40 is a phi2 constant section of the ODF obtained after 20% reduction in thickness in the $L1_0$-ordered condition. The starting microstructure before cold deformation is dominated by the cube component (similar to figure-6.31) that emerges during the grain growth of the CR transformed microstructure. The cube component also appears to be the dominant texture component after 20% reduction in thickness (maximum intensity approximately 31 times random).

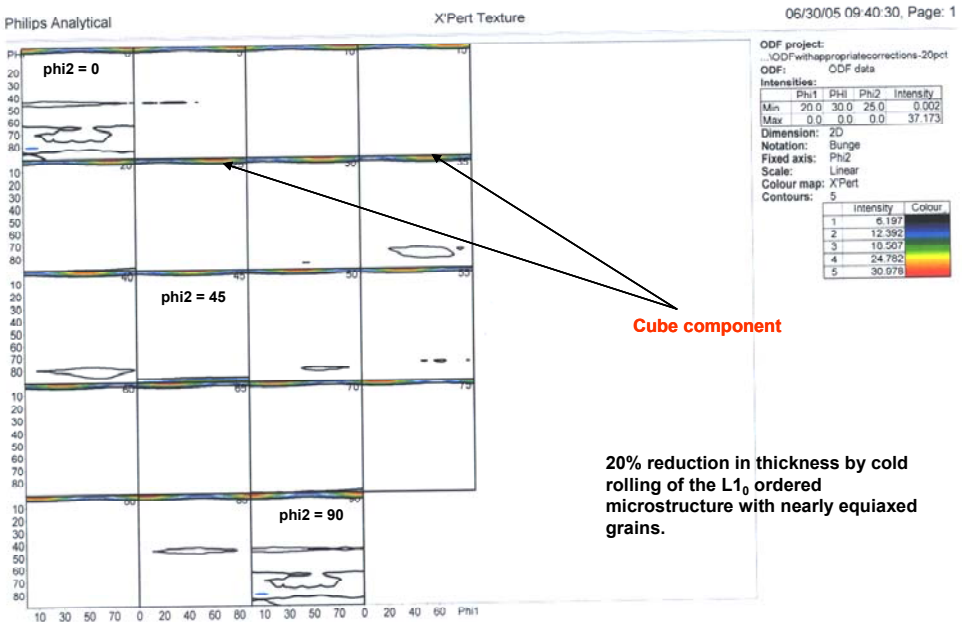

Figure – 6.40 phi2 constant section of the ODF obtained from the sample cold deformed to 20% reduction in thickness by cold rolling in the $L1_0$-ordered condition.

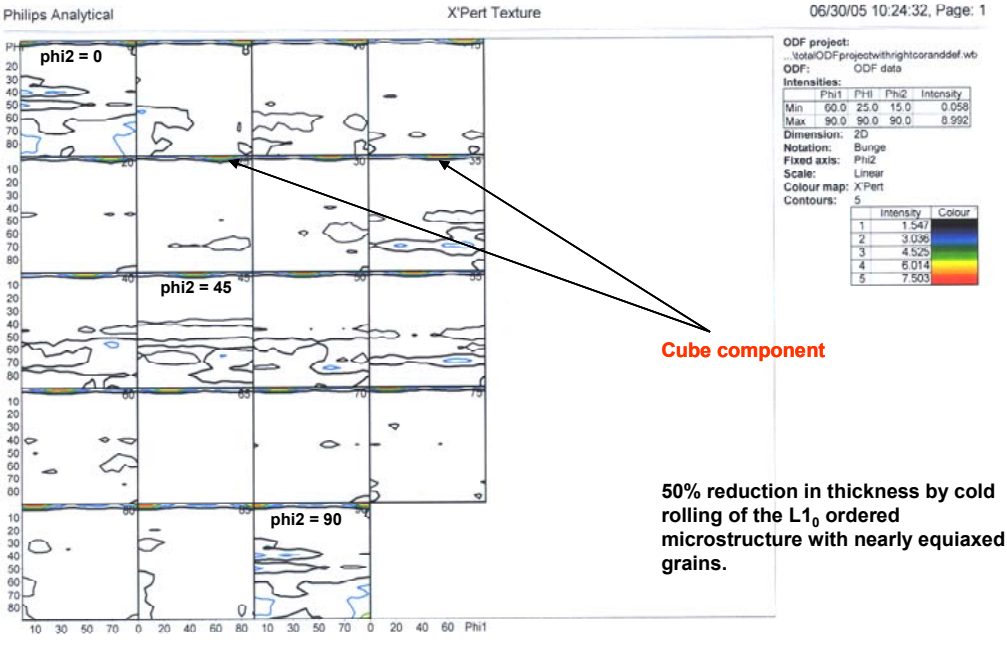

Figure – 6.41 phi2 constant section of the ODF obtained from the sample cold deformed to 50% reduction in thickness by cold rolling in the $L1_0$-ordered condition.

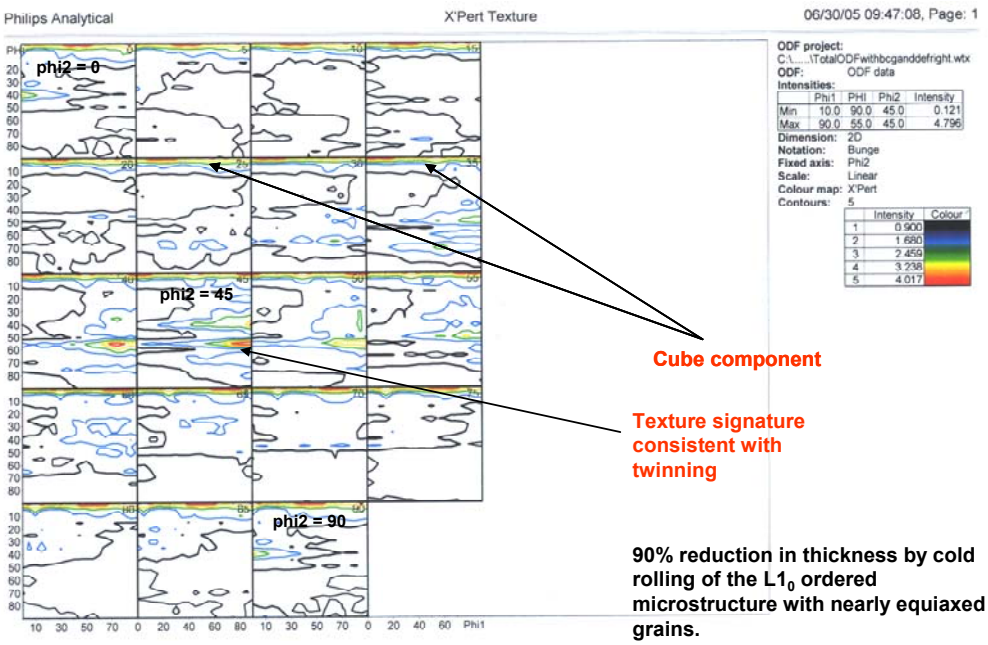

Figure – 6.42 phi2 constant section of the ODF obtained from the sample cold deformed to 90% reduction in thickness by cold rolling in the $L1_0$-ordered condition.

Figure-6.41 is a phi2 constant section of the ODF after 50% reduction in thickness. This section depicts the weakening of the cube component as compared to the 20% thickness reduced sample (maximum intensity approximately 7 times the random). Figure-6.42 is a phi2 constant section of the ODF after 90% reduction in thickness. A further weakening of the cube component as compared to the 50% reduction in thickness sample can be observed in this condition.

The maximum intensity is only approximately 4 times random. Moreover, considerable spread in intensity can also be observed in the vicinity of the expected signature of the cube component. Additional texture component signatures, such as that consistent with twinning[67] , also start to emerge in the phi2 = 45° constant section.

Hence, it appears reasonable to conclude that the cube component inherited from the grain growth regime of the previously CR transformed starting microstructure, while weakening

considerably, persists and dominates the texture evolution. Also, it appears that the process of twinning as a deformation mechanism starts to become significant only in the later stages of deformation. This observation is in sharp contrast with previous studies that have observed twinning as a deformation mechanism in $L1_0$-ordered polytwin microstructures that were deformed by cold rolling to only 30% reduction in thickness[58]. It is also worth noting that the final texture after cold deformation in the equiaxed $L1_0$-ordered condition (figure-6.42) appears to be considerably different than that observed after comparable cold deformation in the FCC condition (figure-6.4). The brass component was significantly present in the phi2 = 0° constant section of the ODF obtained from the FCC deformed sample. This component is only weakly present in the texture signature of the deformed $L1_0$-ordered microstructure. Moreover, mechanical twinning appears to be a more prominent mechanism by which deformation is achieved in the $L1_0$-ordered sample as compared to the FCC sample.

Thus, the data sets obtained from X-ray diffraction, vibrating sample magnetometry and conventional TEM observations establish a number of important differences between the cold deformed starting states prior to CR transformation and conventional annealing

.

6.4 CONVENTIONAL ANNEALING AFTER COLD DEFORMATION IN THE $L1_0$-ORDERED CONDITION.

6.4.1 Early stages of Annealing at 600°C – regaining of order

Figure-6.43 depicts the XRD symmetric θ-2θ scans obtained after different amounts of thickness reduction in the $L1_0$-ordered condition (scans-1 through 7). Superimposed are scans obtained

after annealing the sample at 600°C. The sample after 90% reduction in thickness has been annealed at 600°C for 0.5 hour and 1 hour (scans-8 and 9 respectively).

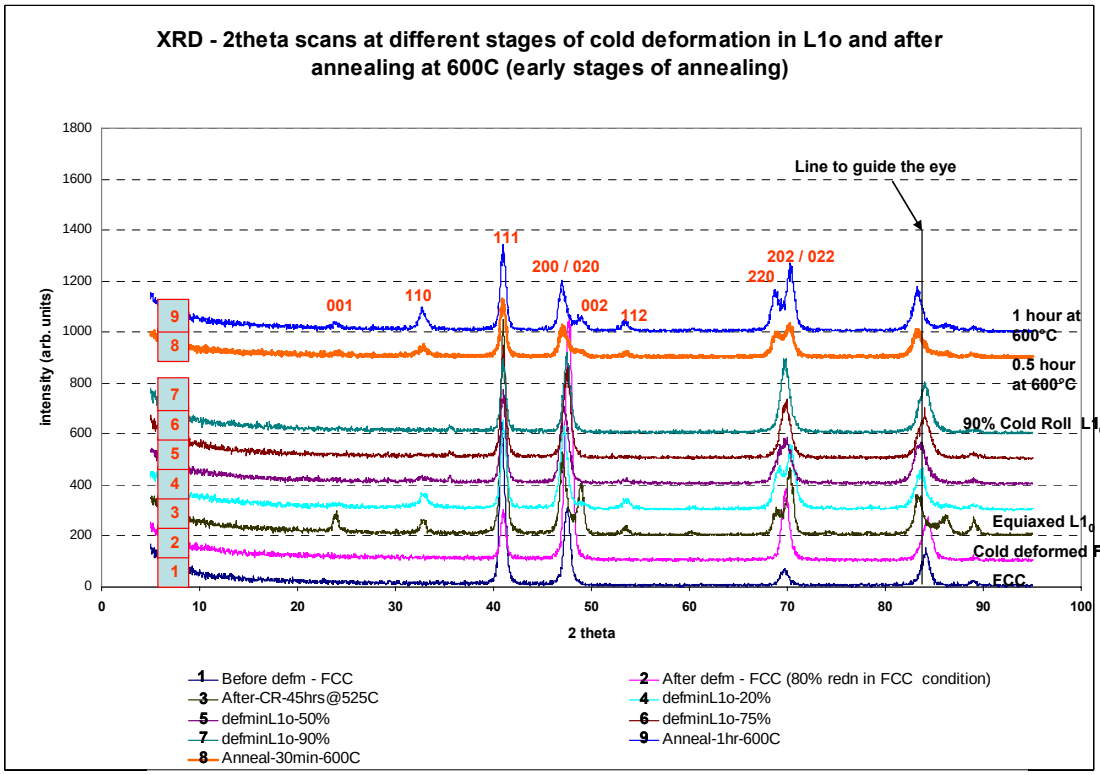

Figure-6.43 Symmetric θ-2θ scans obtained using XRD at different stages of cold rolling in the $L1_0$-ordered condition. Superimposed are scans obtained from early stages of annealing at 600°C.

The emergence of superlattice peaks, such as the 110, after 0.5 hours of annealing is evident in scan-8. Peak splitting in chemical ordering sensitive peaks, such as the 200/020 and 002 peaks, is also evident. The c/a ratio calculated utilizing the d spacings computed from 200/020 and 202/022 peak positions was found to be 0.964 (+/- 0.003). This value agrees within the error margin with the equilibrium c/a ratio for the $L1_0$-ordered structure (0.966). Thus, from these observations it seems reasonable to conclude that after only 0.5 hour at 600°C the microstructure

appears to be completely $L1_0$-ordered. Previous studies[32] have reported the attainment of a completely $L1_0$-ordered microstructure after 3 hour at 600°C after 97% reduction in thickness in FCC condition (CR transformation at 600°C). Thus, the attainment of the $L1_0$-ordered structure after only 0.5 hours at 600°C after comparable deformation during conventional annealing is in direct contrast with the observation for CR transformation.

6.4.2 Texture Evolution during Conventional Annealing – early stages

Figure-6.44 is a phi2 constant section of the ODF obtained after annealing for 1 hour at 600°C after 90% reduction in thickness in $L1_0$-ordered condition. The cube component appears to be the most dominant texture component in the ODF section (Maximum intensity is approximately 33 times random). Moreover, the spread in intensity near the ideal cube component signature observed in the cold deformed (90% reduced sample) is no longer visible in the signature obtained from the annealed sample.

Thus, the significant texture component observed at the onset of conventional annealing is similar to that observed in the cold deformed condition. The cold deformed textures are different prior to CR transformation and prior to conventional annealing. However, a similarity exists in the texture evolution during transformation. Both types of microstructural transformations lead to an inheritance of the cold deformed texture into the transforming microstructure. However, the underlying reasons for this similarity in texture signatures are completely different and will be developed in greater detail in the next chapter. Additional observations that would aid in clarifying this distinction will be presented.

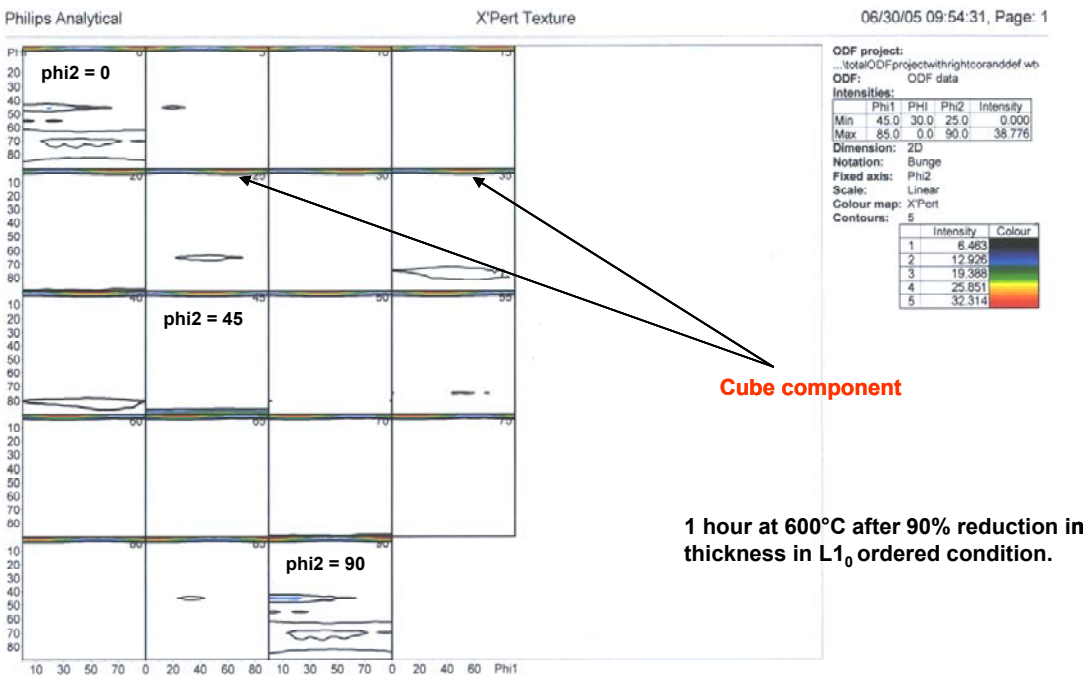

Figure – 6.44 phi2 constant section of the ODF obtained from the sample annealed for 1 hour at 600°C.

Figure-6.45 is a multibeam bright field TEM micrograph depicting the microstructure after annealing for 1 hour at 600°C after 90% reduction in thickness in the $L1_0$-ordered condition. Inset is the selected area diffraction pattern obtained from a large field of view (~ 40 μm) of this microstructure. The presence of rings corresponding to the superlattice reflections (001, 110 etc) in the diffraction pattern supports the conclusion drawn from XRD data that the sample is completely ordered after annealing for 0.5 hour at 600°C. Regions that appear to be devoid of any crystal defect contrast also appear in this bright field micrograph and are most likely new recrystallized $L1_0$-ordered grains. Contrast features associated with the large density of crystal defects that were introduced during the process of cold deformation can still be seen present in this microstructural state. However, these crystal defects appear to be spatially distributed in such a fashion that they form narrow regions with a high density of defects encompassing

regions that appear to have a lower density of defects. Such spatial arrangements are most likely signatures of the recovery processes that allow for annihilation of excess defects via their recombination and rearrangement[9]. Thus, it could be reasonably concluded that the processes of recovery are most likely dominant in the microstructural transformations during the early stages of annealing and that recrystallization is only sparsely occurring after 1 hour at 600°C.

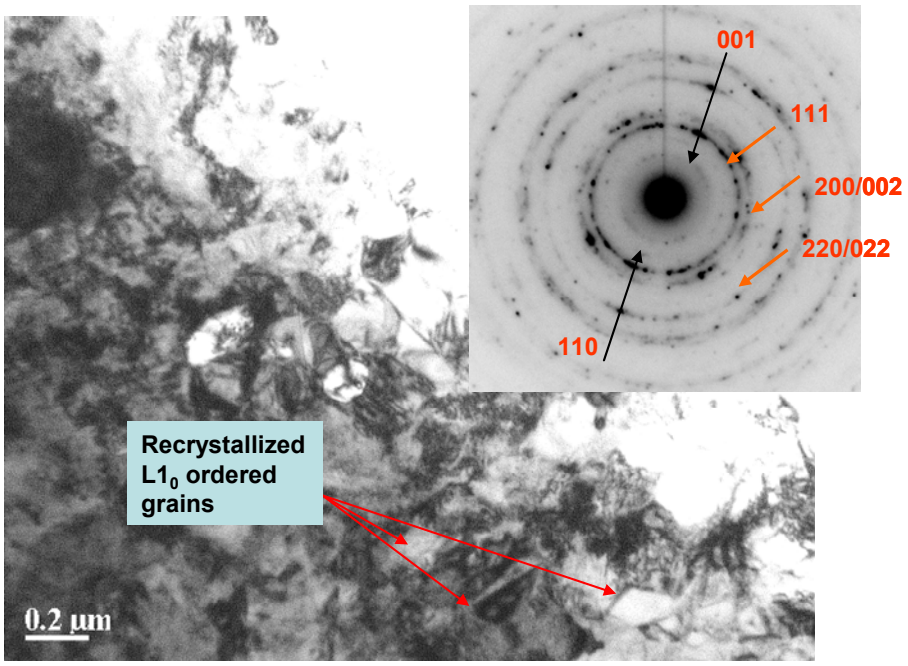

Figure-6.45 Multibeam bright field TEM micrograph depicting the microstructure after annealing for 1 hour at 600°C after 90% reduction in thickness in the $L1_0$ ordered condition. Inset – diffraction pattern obtained from this ordered microstructure.

Figure-6.46 is a HREM micrograph obtained from a sample that has been annealed for 0.5 hour at 600°C after 90% reduction in thickness in the $L1_0$-ordered condition. The approximate crystallographic orientations of different regions in this HREM micrograph can be discerned

from the FFTs. Interference contrast characteristic of regular atomic arrangements can be observed in this HREM micrograph in the vicinity of regions labeled fft1 and fft2.

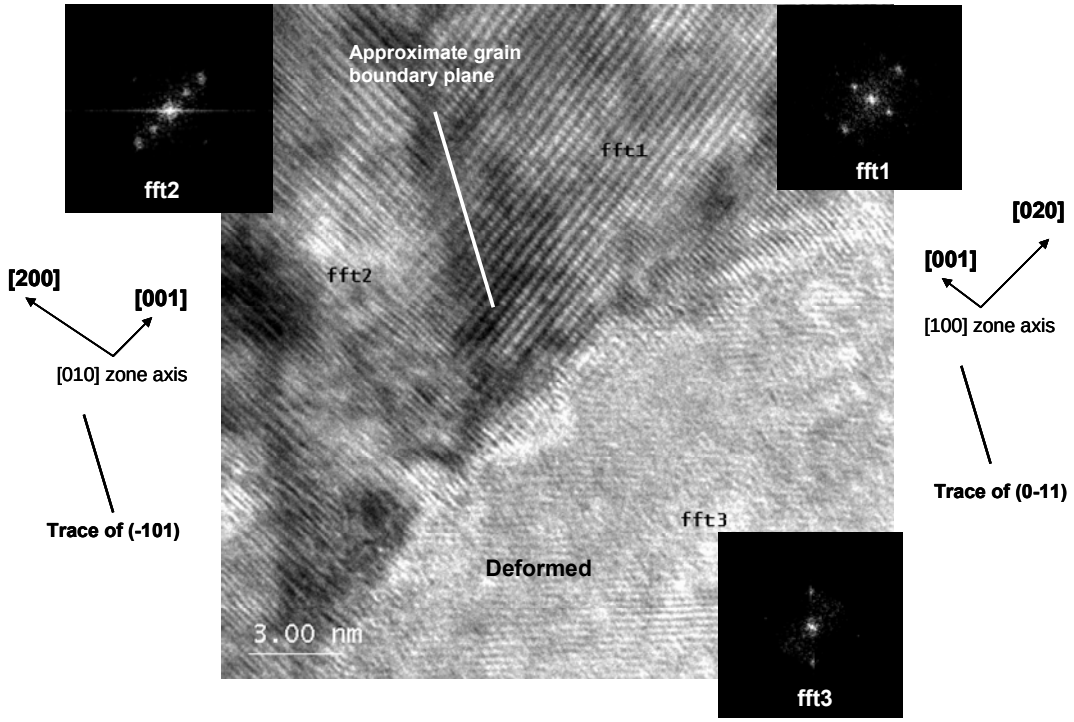

Figure-6.46 HREM micrograph obtained from sample annealed for 0.5 hour at 600°C. Insets FFTs obtained from different regions.

The absence of such regular contrast variations in the vicinity of the label fft3 indicates crystal lattice is not oriented into an orientation of sufficient symmetry relative to the electron beam. Furthermore, some of the localized contrast features in region in the vicinity of the label fft3 appear to suggest that the regular atomic arrangement is most probably disturbed in this region. This could be caused by crystal defects that have been introduced during the cold deformation and have not been annihilated during recovery and recrystallization processes. Thus, it seems reasonable to conclude that the region in the vicinity of the label fft3 has a higher density of

crystal defects as compared to regions marked fft1 and fft2. Moreover, there does not seem to exist a systematic low index orientation relationship between the grain of region labeled fft3 and those of labels fft1 and fft2. From fft1 and fft2 it can be concluded that these regions are oriented with one of their cube axes <100> being parallel to the beam direction. The relative orientations of the c-axis, [001], in both the regions can also be distinguished from the orientation of the intensity maxima corresponding to the periodicity of (001) in fft1 and fft2. The presence of a 90° misorientation between the two crystal lattices can be identified from these ffts. The presence of such 90° boundaries would be consistent with the formation of the cube texture component in the ODF as has been observed in the phi2 constant section of the ODF obtained from the sample annealed for 1 hour at 600°C (figure-6.44).

The observations in this section indicate that recovery processes are mostly dominant in these early stages of annealing. These processes do not alter the morphology and texture of the prior cold deformed microstructure markedly. In fact it seems that the cube texture strengthens during recovery (deduced from the maximum intensity observed in the ODF sections). $L1_0$-ordered regions that have a 90° misorientation across the grain boundary with cube axes approximating as plane normals have been observed in the TEM. The presence of such orientations in the microstructure are consistent with the presence of a rather strong cube texture component.

6.4.3 Attainment of a Completely Recrystallized Microstructure during Conventional Annealing

It has been established previously using X-ray diffraction data that after 0.5 hour of annealing at 600°C the microstructure consists entirely of the $L1_0$-ordered phase with a c/a ratio close to the equilibrium value (see section 6.4.1). Figure-6.47 is a bright field TEM micrograph depicting the microstructure obtained after annealing for 3 hours at 600°C after 90% reduction in thickness

in the $L1_0$-ordered condition. Strain contrast associated with the presence of a large density of crystal defects in the deformed $L1_0$-ordered matrix can be seen in this bright field TEM micrograph. Regions that are relatively devoid of any strain contrast are also visible. These appear to be new recrystallized $L1_0$-ordered grains. Thus, from this overview micrograph it can be concluded that even after 3 hours at 600°C the sample is only partially recrystallized. From TEM micrographs, such as figure-6.47, it can be concluded that only approximately 40% of the volume fraction observed in the micrograph depicts new recrystallized $L1_0$-ordered grains.

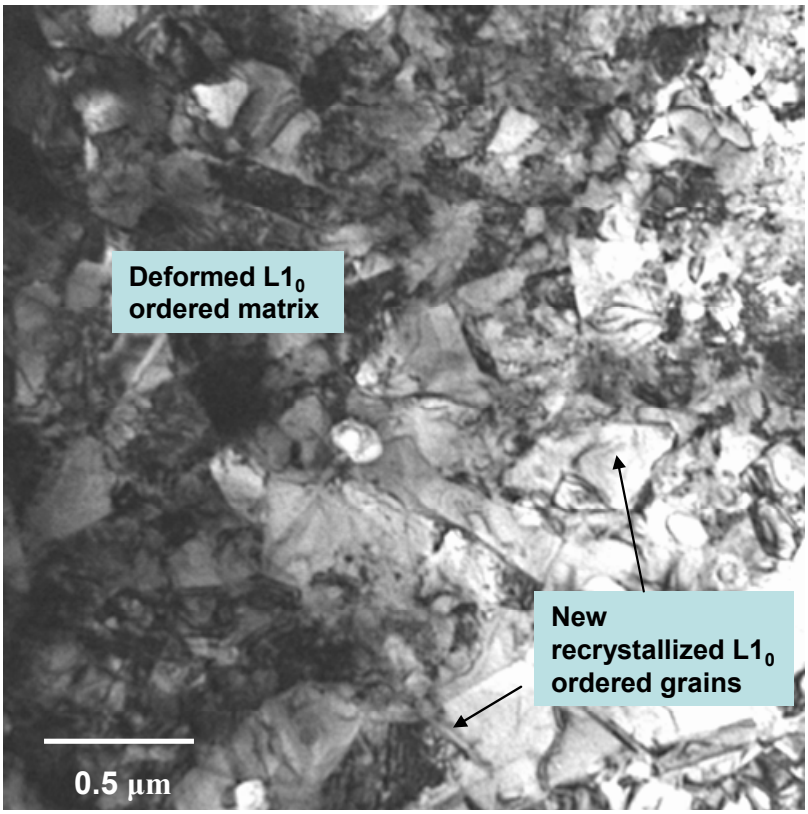

Figure-6.47 Bright field TEM micrograph depicting the microstructure after 3 hours of annealing at 600°C.

Previous studies[32] have reported the generation of microstructure consisting entirely of equiaxed, nearly defect free $L1_0$-ordered grains after 3 hours of annealing at 600°C during CR transformation after comparable amounts of cold deformation in the FCC condition. In contrast, during conventional annealing only 40 vol % of the microstructure appears to consist of new defect free $L1_0$-ordered grains after annealing for 3 hours at 600°C. Thus, it appears reasonable to conclude that the kinetics of the processes that lead to the generation of equiaxed microstructure during CR transformation are faster as compared to the processes in conventional annealing transformation that would generate a morphologically similar equiaxed $L1_0$-ordered microstructure.

Figure-6.48 is a bright field TEM micrograph depicting the partially recrystallized microstructure observed after 3 hours of annealing at 600°C. The diffraction patterns in the inset (DP1 and DP2) have been obtained from the deformed microstructure and the new recrystallized $L1_0$-ordered grain respectively. Since superlattice spots, such as 001, 110, are present in the diffraction pattern obtained from the deformed region, it can be concluded that the deformed matrix is ordered. The presence of strain in the deformed matrix is also evident from the arcing in the diffraction spots. The diffraction pattern DP1 appears to be a composite pattern obtained due to superposition of diffraction from two crystals that have a matrix and twin type relation with each other. From the relative orientations of different directions in the matrix and twin (identified in figure-6.48 inset) it can be concluded that the twins are true order twins. The observation of such true order twins in the deformed matrix is direct evidence of twinning being an important mechanism of deformation in the equiaxed $L1_0$-ordered microstructure.

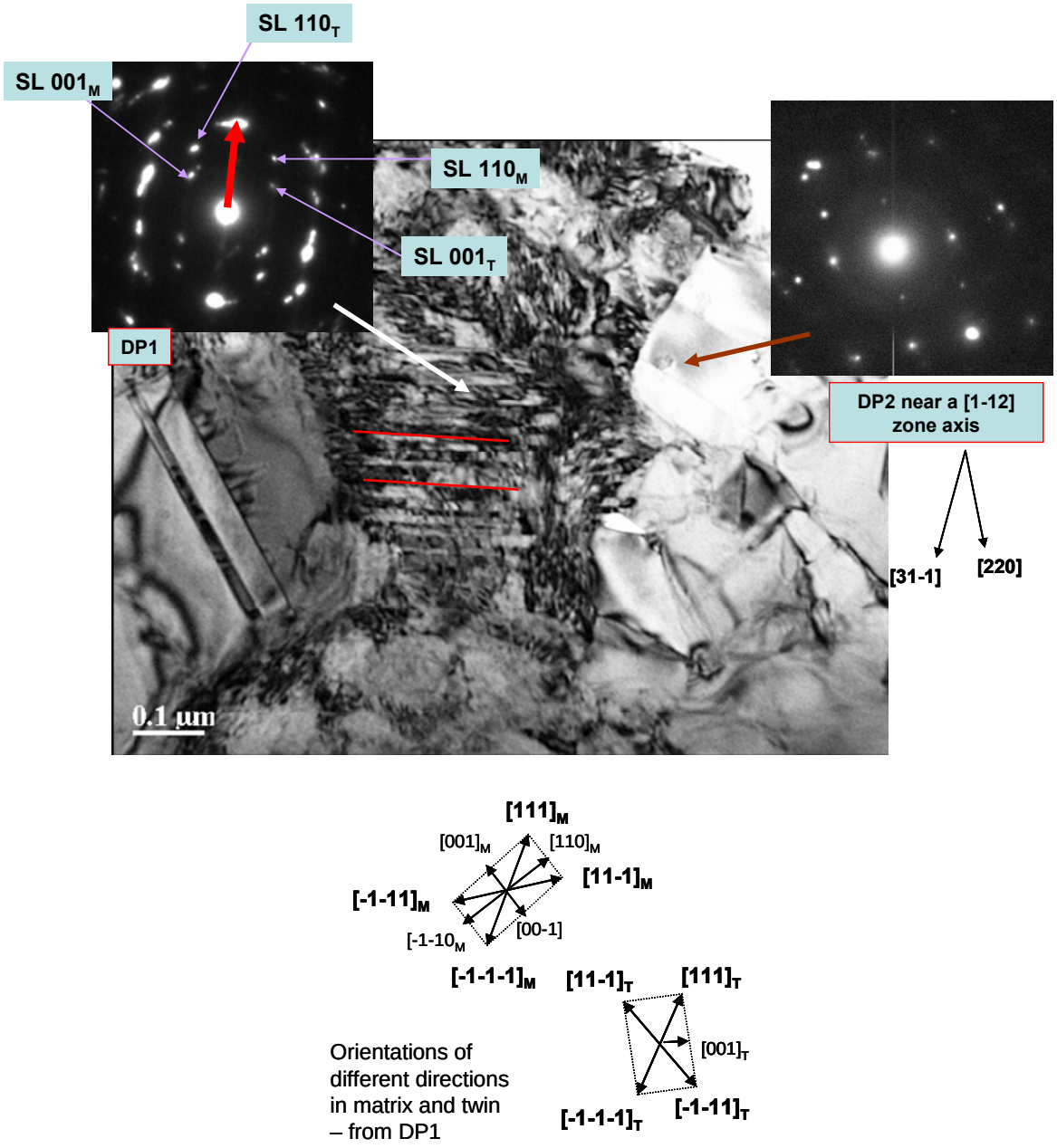

Figure-6.48 Bright field TEM micrograph depicting the deformed matrix and the new recrystallized $L1_0$-ordered grains. The diffraction patterns in the inset have been obtained from the deformed matrix and a recrystallized grain. The relative orientations of different directions in the matrix and twin in the deformed matrix is included as inset.

This TEM observation also corroborates the ODF data in figure-6.42 that gave an indirect evidence of twinning as a deformation mechanism based on the appearance of a texture signature. From the diffraction pattern the coherent twinning interfaces can also be identified and they have been delineated as red lines in the micrograph. The deformed region is diffracting such that the [1-10] is nearly parallel to beam direction. DP2 is a diffraction pattern obtained from the essentially defect free new recrystallized $L1_0$ -ordered grain. This grain is diffracting such that the [1-12] is nearly parallel to beam direction. The presence of superlattice spots such as 110 (with [110] parallel to [220]) can also be discerned. The angle between the [1-10] that is the plane normal in the deformed matrix and the [1-12] that is the plane normal in the recrystallized grain is 54.7°. Thus, the deformed matrix and the recrystallized grain are separated by a high angle grain boundary.

The emergence of such new orientations in the deformed matrix should also lead to a weakening of the prior deformation texture. Figure-6.49 is a phi2 constant section of the ODF obtained from the sample annealed for 3 hours at 600°C. The presence of cube component as the main texture component is still evident. However, the maximum in intensity has decreased to only approx 4 times random (as compared to the approx 33 times random observed after 1 hour at 600°C). Thus, it appears reasonable to conclude that recrystallization in the deformed $L1_0$-ordered matrix, unlike CR transformation, proceeds by the formation of new defect free grains that have a different orientation as compared to the deformed matrix. There appears to be no 'oriented nucleation', as was observed during CR transformation. Hence, the process of recrystallization during conventional annealing of the deformed $L1_0$-ordered alloy is similar to that observed in deformed solid solutions with a FCC crystal structure without a chemically ordered motif and that do not undergo an ordering transformation (e.g. recrystallization of

copper) and proceeds by generation of new orientations in the deformed matrix. A new recrystallization texture, different from the cold-deformation texture develops.

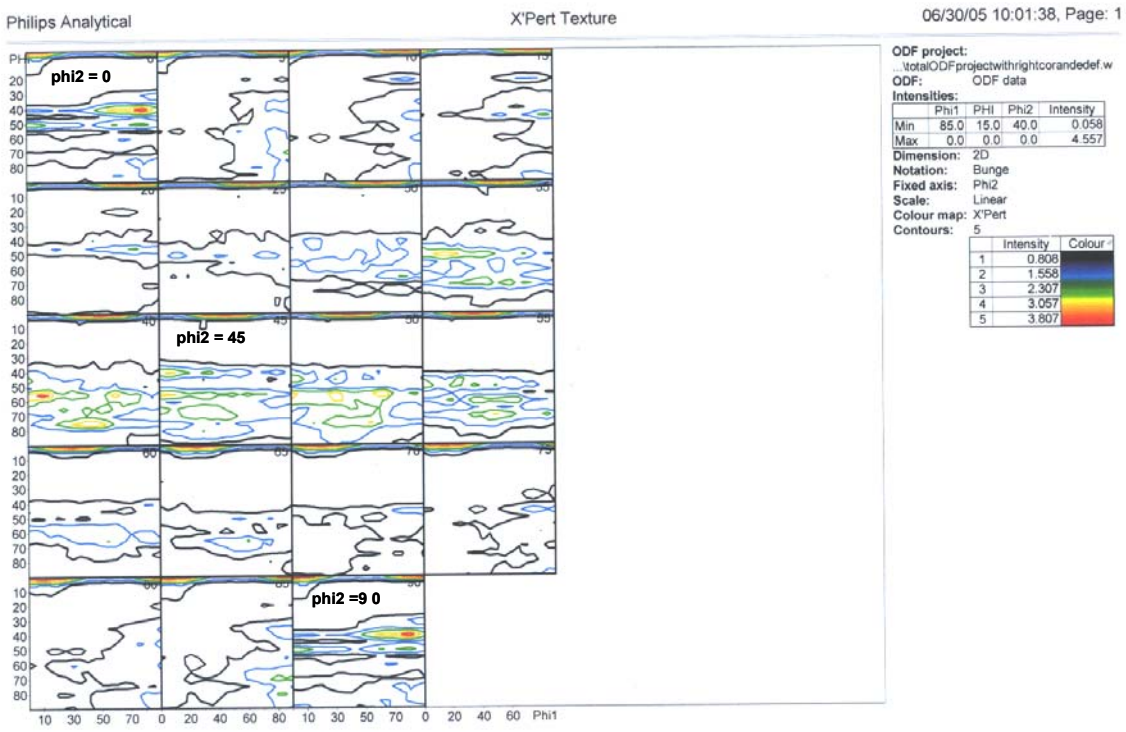

Figure-6.49 phi2 constant section of the ODF obtained from sample that was annealed for 3 hours at 600°C after 90% reduction in thickness in the $L1_0$-ordered condition.

Figure-6.50 is a bright field TEM micrograph depicting the microstructural state after 8 hours of annealing at 600°C. The microstructure appears to consist nearly entirely of new recrystallized $L1_0$-ordered grains. Thus, the process of recrystallization is essentially complete after about 8 hours of annealing at 600°C after 90% reduction in thickness in the equiaxed $L1_0$-ordered microstructure.

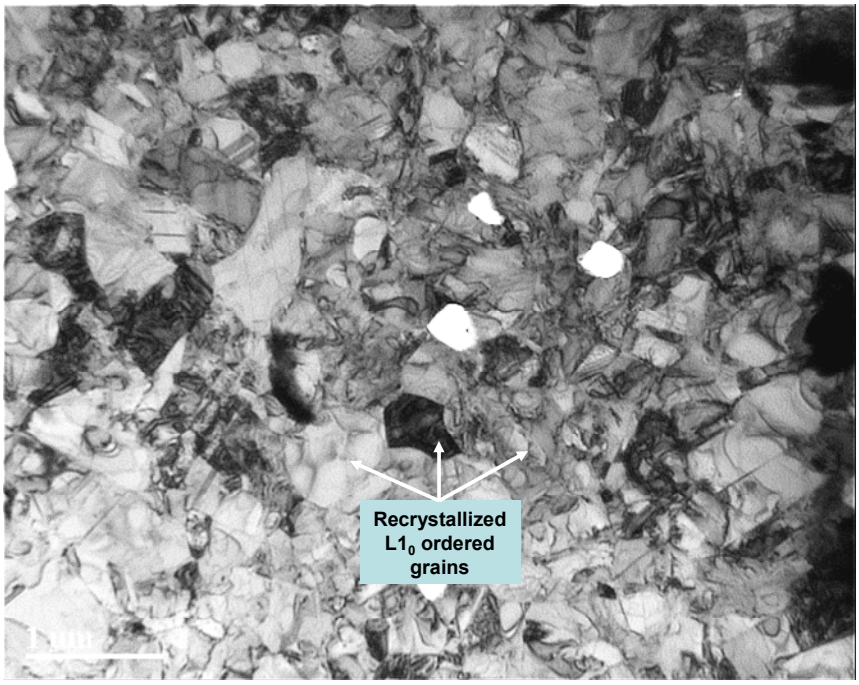

Figure-6.50 Bright field TEM micrograph obtained from a sample annealed for 8 hours at 600°C after cold rolling to 90% reduction in thickness in $L1_0$ condition.

Figure-6.51 is a phi2 constant section of the ODF obtained from the sample annealed for 8 hours at 600°C. The cube component appears to be the dominant texture component in this microstructure. However, the maximum in intensity obtained is only approx 6 times random. This is still very low as compared to the approximately 33 times random observed after 1 hour of annealing at 600°C (during recovery). Thus, it can be concluded that the process of recrystallization does not significantly promote the formation of a cube texture. Recrystallization progresses by formation of new defect free $L1_0$-ordered grains in the deformed $L1_0$-ordered matrix, with these new grains having no apparent, systematic, high symmetry orientation relationship with the deformed matrix.

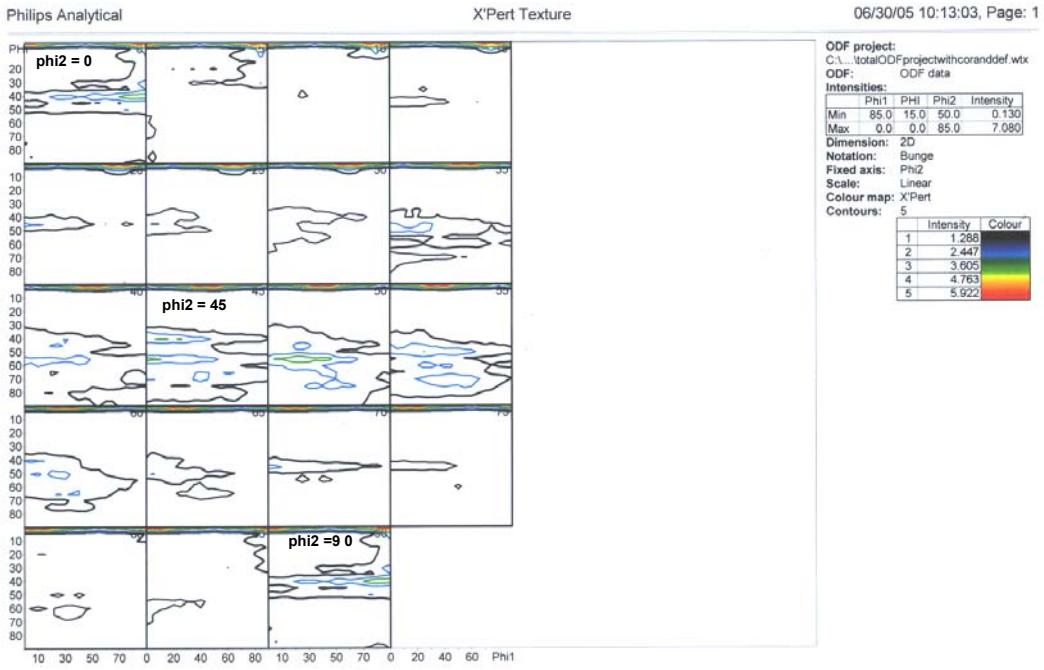

	Phi1	PHI	Phi2	Intensity
Min	85.0	15.0	50.0	0.130
Max	0.0	0.0	85.0	7.080

	Intensity	Colour
1	1.286	
2	2.447	
3	3.605	
4	4.763	
5	5.922	

Figure-6.51 phi2 constant section of the ODF after annealing for 8 hours at 600°C.

6.4.4 Emergence of Crystal Defects during Recrystallization

Figure-6.52 is a bright field TEM micrograph obtained from a newly recrystallized $L1_0$ -ordered grain (1 hour at 600°C). The diffraction pattern in the inset has been obtained from the vicinity of the straight interface observed in this micrograph as indicated. From the diffraction pattern it can be concluded that this interface separates two crystalline $L1_0$-ordered regions that are diffracting with their [101] parallel to the beam direction. The relative orientations of different directions in the two regions separated by the boundary have also been identified. From these observations it can be concluded that the two crystalline regions have a matrix and twin type orientation relationship and the conjugation plane, the planar interface is of the type {111}. From the diffraction pattern it can also be deduced that these are true-order twins. Figure-6.53a and 6.53b are dark field TEM micrographs obtained using the $g = [1\text{-}1\text{-}1]_M$ and $g = [1\text{-}1\text{-}1]_T$ respectively.

The rather straight coherent twin interface that separates the two crystals can be identified from these dark field micrographs. The feature labeled x in figure-6.52 can also be seen in these dark field micrographs. From these DF micrographs this feature can be identified as a microtwin lamella. Moreover, from figure-6.53a it can also be concluded that the microtwin has the same orientation as the matrix. Similar microtwin lamellae (labeled u and v) can also be seen to emerge in the matrix (figure-6.52).

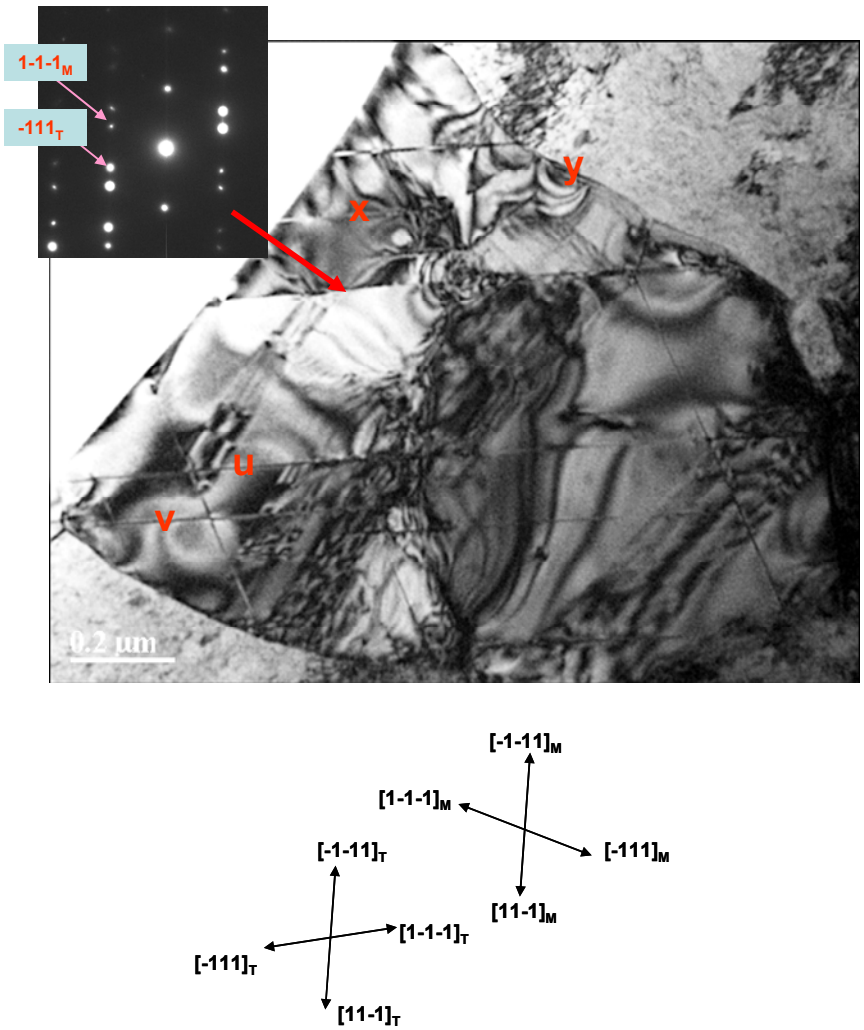

Figure-6.52 Bright field TEM micrograph depicting the generation of twins and stacking faults in newly recrystallized $L1_0$-ordered grain. Inset-diffraction pattern obtained in the vicinity of the twin interface.

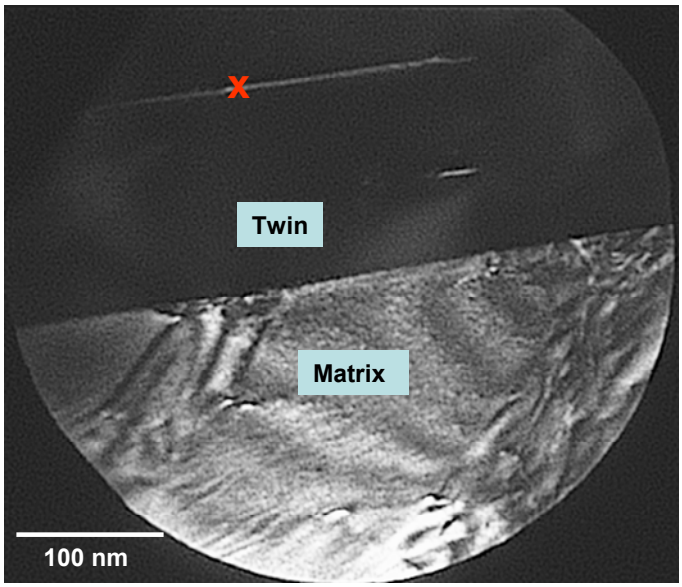

Figure-6.53a Dark field TEM micrograph obtained using g = $[1\text{-}1\text{-}1]_M$

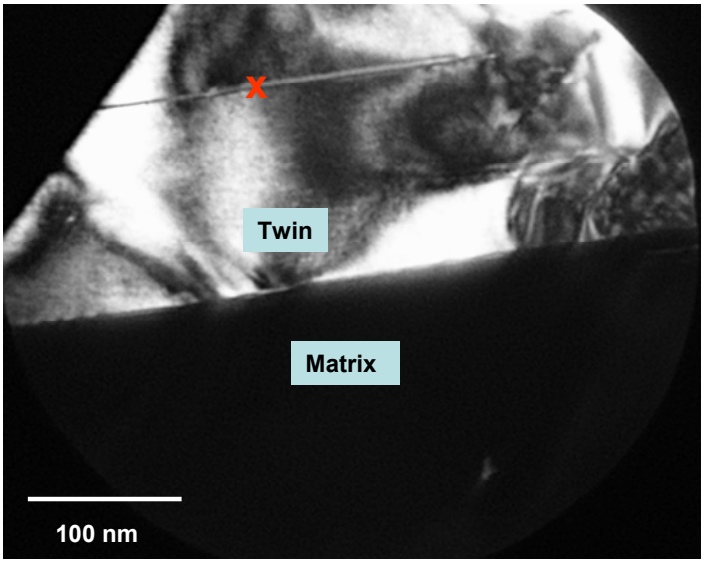

Figure-6.53b Dark field TEM micrograph obtained using g = $[1\text{-}1\text{-}1]_{T.}$

Figure-6.54 is a bright field TEM micrograph obtained from the partially recrystallized microstructure after annealing for 1 hour at 600°C. Inset is the diffraction pattern that has been obtained from the superposition of diffraction patterns obtained from three $L1_0$-ordered crystalline regions with different orientations that are enclosed within the selected area aperture.

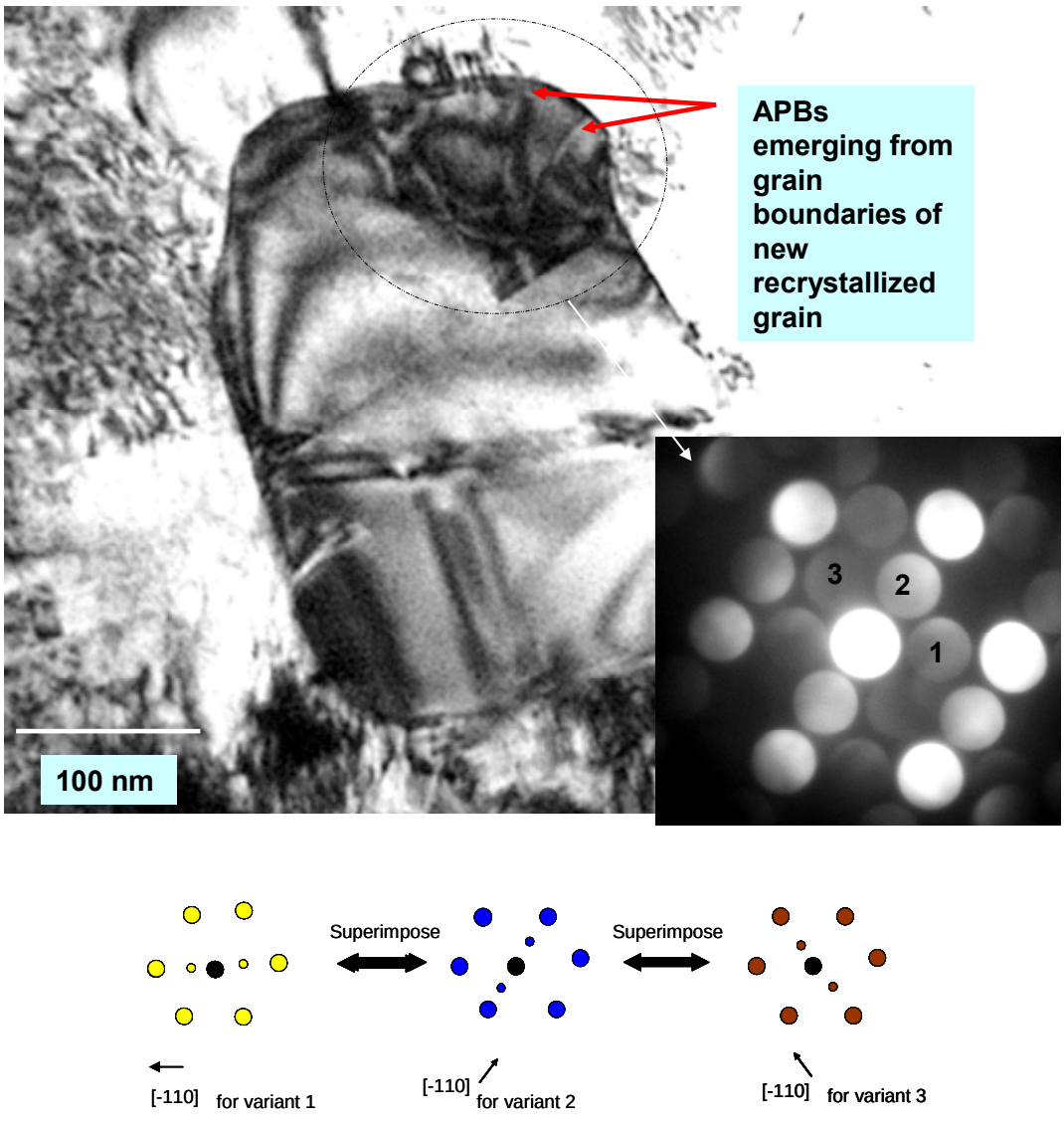

Figure-6.54 Bright field TEM micrograph depicting the emergence of APBs in the recrystallized microstructure. Inset-diffraction pattern obtained from the recrystallized grain with some contribution from the surrounding deformed ordered matrix.

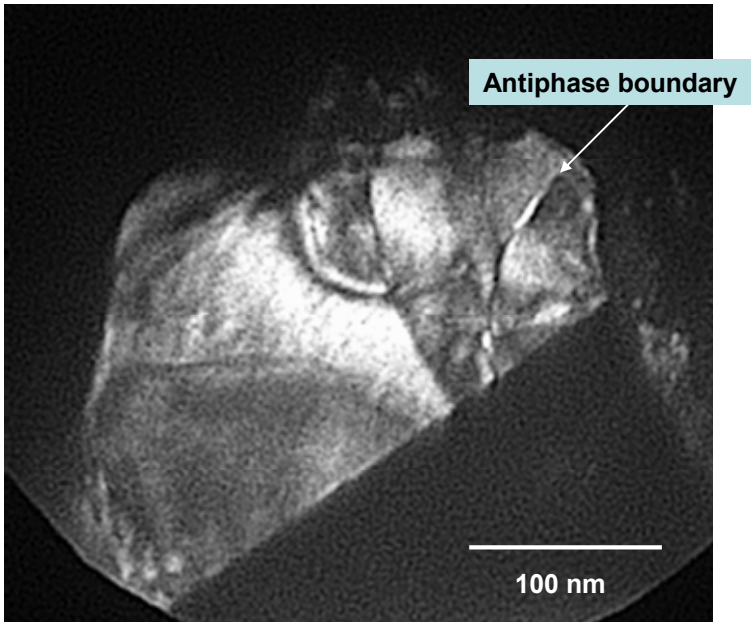

Figure-6.55 Dark field TEM micrograph obtained using superlattice spot -1 from the diffraction pattern in figure-6.54

All three regions enclosed in the SA aperture in figure-6.54 are diffracting with <111> parallel to the beam direction. Wavy features that could be antiphase boundaries emerging from the grain boundary of the recrystallized grain can be seen. The emergence of two APB related regions within the new recrystallized grain can also be discerned from the presence of superlattice spots (numbered 1 and 2) corresponding to two different orientations. Superlattice spot numbered 3 can be attributed to the presence of $L1_0$-ordered deformed matrix that has also been enclosed in the SA aperture. To verify the presence of APBs, dark field imaging in the TEM using superlattice spot number 1 has been conducted. This has been depicted in figure-6.55

The wavy segment exhibits bright contrast in this dark field micrograph obtained using the superlattice spot numbered 1, confirming it to be an APB. Other APB segments also appear in bright contrast. All these segments seem to terminate on the rather straight interface observed in

the micrograph. This interface could possibly be a twin interface that does not appear to be edge on in this micrograph.

Figure-6.56 is a bright field TEM micrograph depicting the microstructure obtained after annealing for 3 hours at 600°C. A rather large density of residual dislocations can be seen to be present in the recrystallized $L1_0$-ordered grains, which are typically arranged in linear arrays.

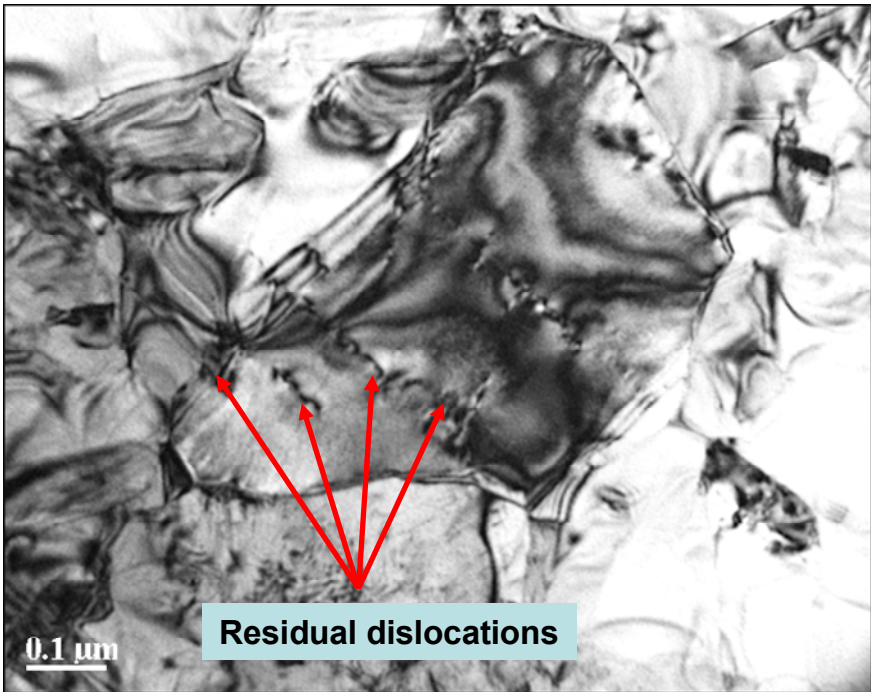

Figure-6.56 Bright field TEM micrograph depicting residual dislocations in the recrystallized grain (3 hours at 600°C).

A qualitative comparison between the grains obtained after CR transformation (e.g. figure-6.25) and during conventional annealing (e.g. figure-6.56) in terms of their crystal defect content is now possible. While cascades of stacking faults and twins have been observed to emerge from grain boundary segments during CR transformation, yet there have been no observations of considerable amounts of residual dislocations (from the cold deformed state) being inherited in

the CR transformed grains. During conventional annealing the emergence of twins and cascades of stacking faults has also been observed (figure-6.52) along with other defects, such as APBs (figure-6.54). In addition, a significant density of dislocations inherited from the cold deformed $L1_0$-ordered state is also seen to be present in the recrystallized grains (figure-6.56). Thus, it appears reasonable to qualitatively conclude that the new recrystallized $L1_0$-ordered grains still contain more defects when compared to the CR transformed grains obtained during annealing at 600°C.

6.4.5 Emergence of Crystal Defects during Grain Growth

Figure-6.57 is a bright field TEM micrograph that depicts the microstructure obtained after 12 hours of annealing at 600°C after 90% reduction in thickness in the $L1_0$-ordered condition.

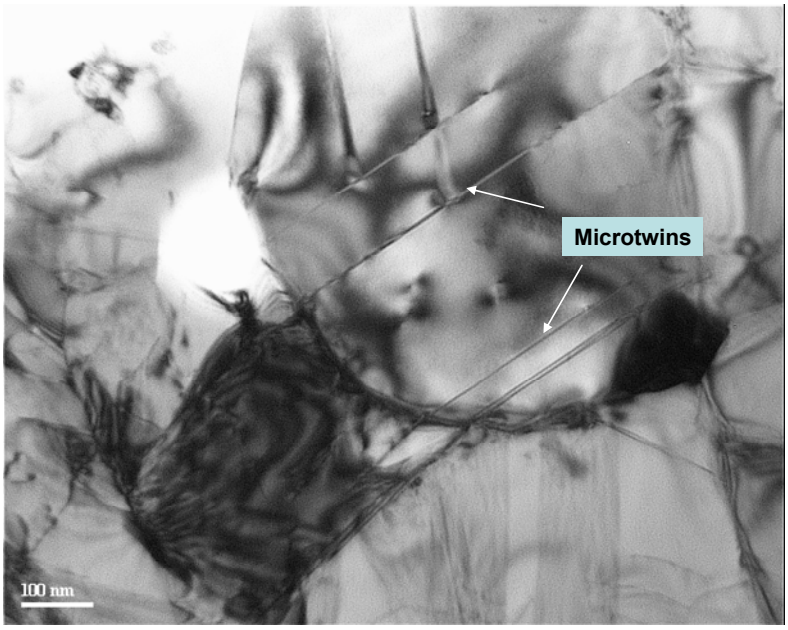

Figure-6.57 Bright field TEM micrograph depicting the microstructure during grain growth (12 hours at 600°C)

This is the microstructural state during the process of grain growth. Figure-6.57 depicts the emergence of extremely narrow microtwins from grain boundary segments of grains that are undergoing grain growth during conventional annealing. This is one of the significant types of twin morphology that appears to emerge during grain growth during conventional annealing. This morphology is similar to the microtwins observed during grain coarsening after CR and most likely has similar mechanistic origin.

6.4.6 Grain Growth after Recrystallization of the $L1_0$ - ordered Deformed Matrix

Figure-6.58 is a phi2 constant section of the ODF obtained after 16 hours of annealing at 600°C. This is a sample that has undergone grain growth for 8 hours at 600°C.

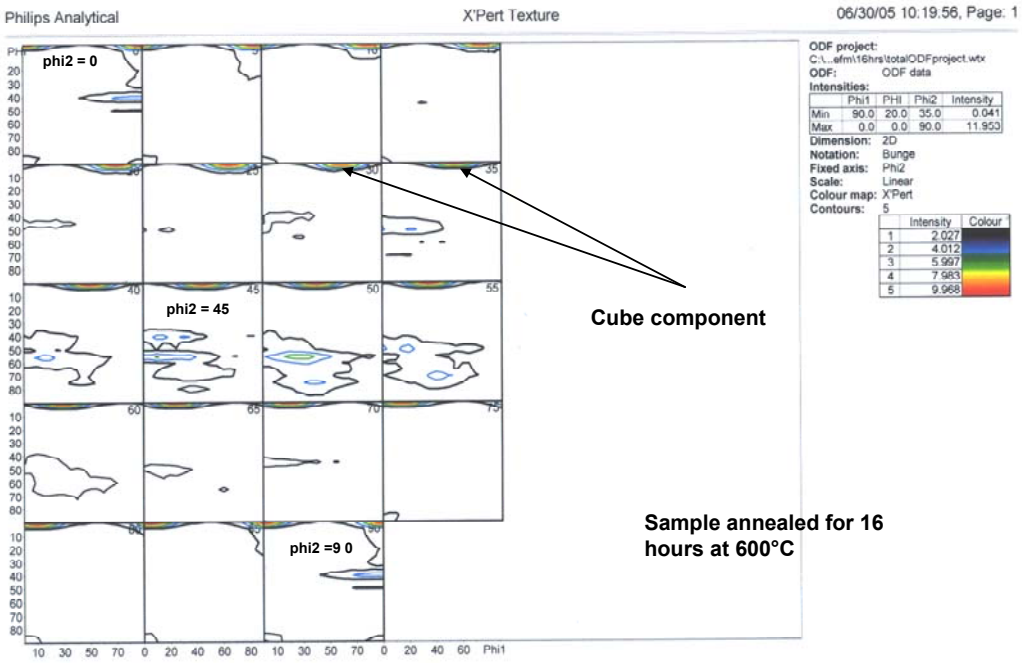

Figure-6.58 phi2 constant section of the ODF obtained from a sample annealed for 16 hours at 600°C.

The cube component appears to be the dominant texture component in this phi2 constant section. The maximum in intensity is approx. 10 times random. The cube component was also seen to be the dominant component after recrystallization was complete (8 hours at 600°C). However, the maximum in intensity was only observed to be approx. 6 times random. Thus, it can be concluded that the cube component increases in strength during grain growth. In other words, the number of grain orientations that contribute to the cube component has definitely increased during grain growth.

OIM investigations have also been conducted to obtain independent proof for the strong presence of cube component exhibited by the ODFs obtained using X-ray diffraction.

Figure-6.59 is a chart obtained using OIM in the SEM. It has been obtained from the sample that was annealed for 12 hours at 600°C after 90% reduction in thickness in the $L1_0$-ordered condition. The largest fraction of boundaries (~ 11% by number fraction) consists of boundaries with 90° misorientation angle between the two grains separated by the boundary segment.

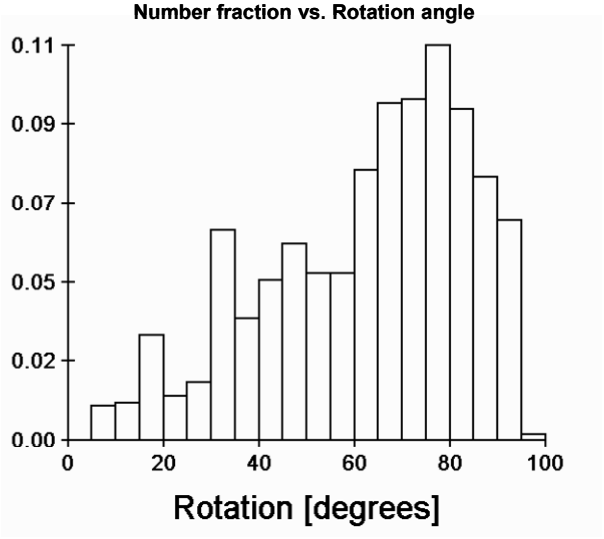

Figure-6.59 Number fraction vs. rotation angle chart obtained for the sample that was annealed for 12 hours at 600°C after 90% reduction in thickness in the $L1_0$-ordered condition.

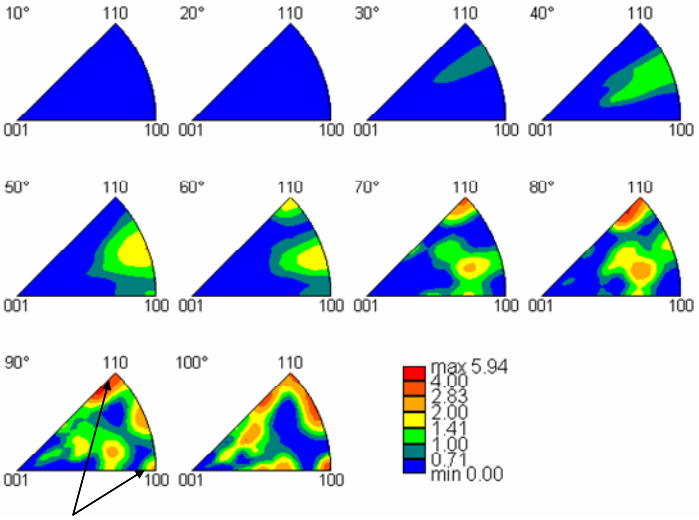

Figure-6.60 MDF representation of different types of grain boundaries observed after 12 hours at 600°C.

Figure-6.60 is a plot of the misorientation distribution function (MDF) obtained using OIM in the SEM for the same sample (12 hours at 600°C). The MDF in figure-6.60 is an intensity plot (using number fraction) of the grain boundaries with different misorientation angles across them. From the MDFs it can be deduced that the 90° misorientations occur with either the cube axes or the [110] direction being the rotation axes. Hence, it can be deduced that the cube component emerges to dominate during grain growth.

Figure-6.61 is a plot of grain boundary number fraction vs. rotation angle that has been obtained from the sample annealed for 24 hours at 600°C after 90% reduction in thickness in the $L1_0$-ordered condition.

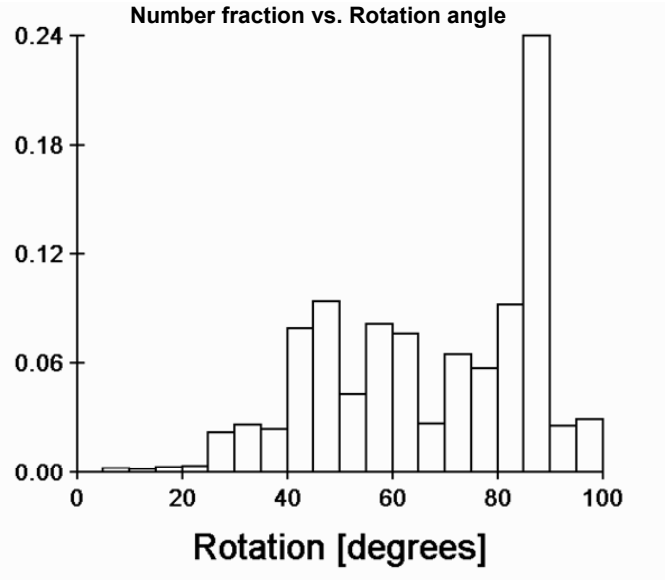

Figure-6.61 Number fraction vs. rotation angle chart obtained for the sample that was annealed for 24 hours at 600°C after 90% reduction in thickness in the $L1_0$-ordered condition.

It can be inferred from this chart that the fraction of 90° boundaries has increased during grain growth. Figure-6.62 is an MDF obtained from the same sample. From this MDF representation it can be inferred that the cube axes (esp. [100]) are preferred rotation axes. These observations support the conclusion drawn based on ODFs obtained using X-ray diffraction that the cube component emerges as a dominant texture component during grain growth.

The cube component is expressed in the microstructure by a dominant presence of the 90° boundaries. It was perceived that the understanding of the spatial emergence of these 90° boundaries in the microstructure could shed some light on the mechanism by which the cube component comes to dominance in the microstructure. To gain such insight localized OIM experiments were conducted.

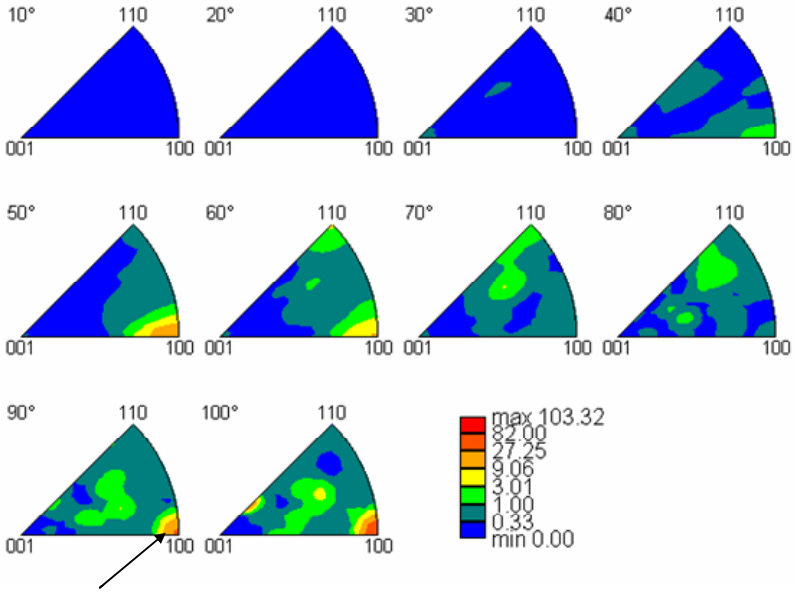

Figure-6.62 MDF representation of different types of grain boundaries observed after 24 hours at 600°C.

Areas in the microstructure as small as 3.5μm x 3.5μm were analyzed. Figure-6.63a depicts the grain structure identified by the OIM in one such small area scan conducted on a sample annealed for 24 hours at 600°C during conventional annealing. All the regions in this map with the same color have the same crystallographic orientation. The nature of the different grain boundaries was analyzed. Since the interest was mainly to study the spatial emergence of 90° boundaries, the program was set to identify either the presence of a 90° (+/- 5°) boundary or any other general high angle grain boundary (20°to 80° +/-5°). Figures-6.63b and 6.63c depict the emergence of different types of grain boundaries in the microstructure. It can be seen that the grain boundary between small grains labeled C and D (≤ 0.7 μm in diameter) is a general high

angle grain boundary (#1). The grain boundaries between other small grains such as B and D (#2); E and D (#3) and E and C (#9) are also general high angle grain boundaries. However, the grain boundary between small grain such as D and large grains such as G (#s 4, 5, 6) is a 90° boundary. Similar observations hold for other big and small grains such as G and B (#7), A and E (#8). Similarly, it can also be seen that the grain boundary between large grains is a 90° boundary (e.g. between F and A). The cube axis [010] has been identified as the direction common to both of the grains that have the 90° rotation relationship (figure-6.63d). A rotation of 90° with [010] as the rotation axis can be performed to bring both of the crystals into correspondence. It can be inferred from this figure that most of the 90° boundaries are such that they have [010] as the rotation axis. Some segments such as #4,#5,#6 could also be identified with the other cube axes as the rotation axis.

Data from other large area scans depicted a similar behavior. The presence of general high angle grain boundary segments between the smaller grains could be identified. The presence of the 90° boundary segments between large grains, as well as between one large and one small grain could also be globally identified. Thus, it appears reasonable to conclude that during grain growth the general high angle grain boundary segments appear to be replaced by 90° boundaries. The emergence of 90° boundaries with cube axes as the rotation axes in the microstructure leads to the dominance of the cube texture during grain growth. The observation of the emergence of cube texture during grain growth after CR and after conventional annealing depicts a similarity between both of these modes of transformation. In the next chapter a similitude between the coarsening of ordered domains after conventional transformation (FCC to $L1_0$ ordering) into the polytwin structure and the coarsening of grains after CR and conventional annealing will be

established. An attempt will be made to rationalize the emergence of a cube texture during grain growth based on ideas rooted in the coarsening behavior of the polytwin microstructure.

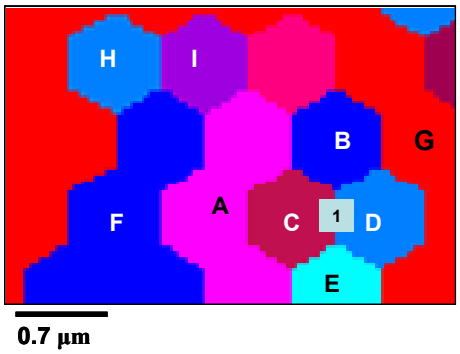

Figure-6.63a

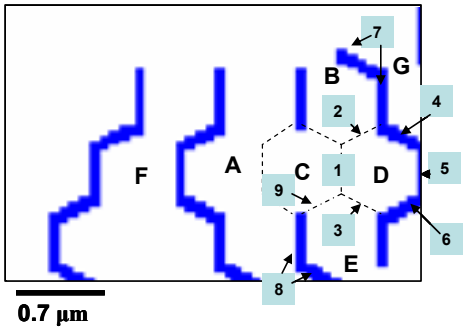

Figure-6.63b

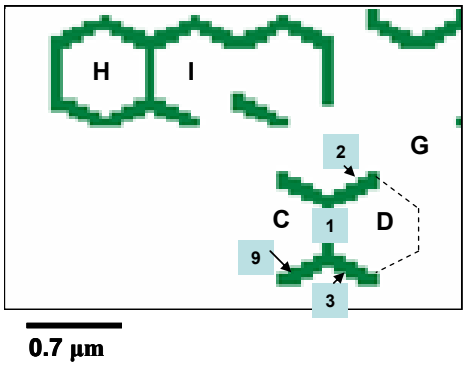

Figure-6.63c

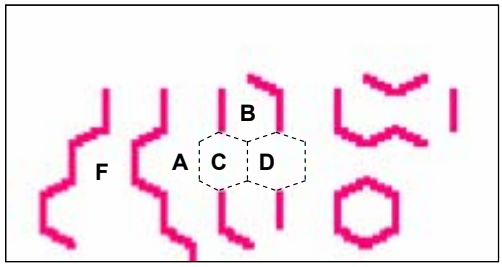

Figure-6.63d

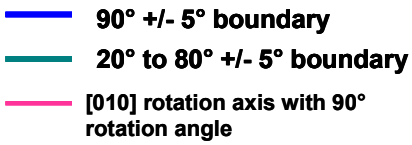

Figure-6.63a The grain structure identified by OIM.

Figure-6.63b The distribution of 90° grain boundaries.

Figure-6.63c The distribution of general grain boundaries

Figure-6.63d The 90° boundaries with [010] as the rotation axis.

The results presented in this chapter will be discussed in greater detail in the next chapter. Existing theories and the modifications thereof will be applied to explain the differences observed during the microstructural evolution during CR transformation and conventional annealing. Thus, the results presented in this chapter will form the kernel for discussion, which will lead to a clear distinction between these two solid state transformations in the Fe-Pd microstructures after cold-deformation.

7.0 DISCUSSION

In the previous chapter the experimental results pertaining to the two different routes of microstructural transformations by the CR and conventional annealing processes were presented separately. In this chapter a direct comparison between the results obtained for these transformations by XRD,SEM,TEM and VSM will be presented. The applicability of different models, mechanisms to explain the observations is intended to be developed in this chapter. This discussion will further increase the understanding of the solid state transformations of CR and conventional annealing.

7.1 THE STARTING COLD DEFORMED STATE

Here, a comparison of the studies of the cold deformed FCC phase and the cold-deformed equiaxed $L1_0$ -ordered phase after imparting comparable strain (% reduction in thickness) by cold rolling is presented. From the results in sections 6.1 and 6.3 it can be concluded that the deformation characteristics of the starting cold deformed FCC phase and the cold deformed $L1_0$-ordered phase are completely different. The texture signatures obtained after cold deformation in the FCC phase and the $L1_0$-ordered phase show considerable differences. The presence of a strong brass component (characteristic of low to intermediate SFE FCC metals) in the phi2 constant section of the ODF after cold rolling in the FCC condition can be observed (figure-6.4).

This observation is in agreement with prior studies[30]. In contrast the brass component is only weakly present in the phi2 constant section of the ODF obtained after cold rolling in the equiaxed $L1_0$-ordered condition (figure-6.42). The texture in the cold-deformed $L1_0$-phase is dominated by the cube component that was present in the predeformation CR transformed equiaxed $L1_0$-ordered microstructure. Considering the maximum in intensity in the ODF plots obtained for increasing amounts of cold deformation in the $L1_0$-ordered phase (figures-6.40 to 6.42) it can be concluded that the process of cold rolling leads to weakening of the cube texture component. A spread in the intensity in the vicinity of the ideal cube component signatures can also be observed. The spread in intensity in the vicinity of the ideal cube component signature could be caused by the development of a 'mosaic' structure in the deformed $L1_0$-ordered microstructure[80]. The TEM micrograph in figure-6.39 exhibits contrast features that can be identified as dislocation cells surrounded by dislocation cell walls that have a higher dislocation density than the cell interiors. This observation qualitatively supports the idea of formation of regions in the microstructure that have small misorientations with respect to each other in a given grain (mosaic structure). The development of a mosaic structure has also been reported in the cold deformed disordered (γ) FCC solid solution of FePd similar to other disordered FCC solid solutions that do not show an ordering transformation[81] . However, the majority of the grain orientations in the cold deformed FCC phase have X-Ray diffraction characteristics such that they contribute to the brass component in the ODF. In the case of the cold deformed $L1_0$-ordered phase the majority of the grain orientations contribute to the cube component. Thus, a significant difference, at least regarding texture, in the starting conditions before transformations, the cold deformed state, can be identified for the Fe-Pd material deformed in the FCC phase and that cold-deformed in the $L1_0$-ordered phase.

The symmetric θ-2θ scans obtained using X-ray diffraction (figure-6.35) also aid in distinguishing between the cold deformed FCC phase and the cold deformed $L1_0$ -ordered phase. These XRD scans have been obtained at different stages of cold deformation processing of the $L1_0$-ordered phase. The c/a ratios obtained from these XRD scans have been plotted as a function of the processing condition in figure-6.36. The c/a ratio is close to the equilibrium c/a ratio of 0.966 at the start of the cold rolling experiments (processing step -3). As the process of cold deformation progresses, the c/a ratio increases from 0.967 (processing step-3) to 0.989 (processing step-7). Thus, the c/a ratio approaches unity. This approach of the c/a ratio to unity is also accompanied by the disappearance of the superlattice peaks (e.g. 001, 110 etc.) and the absence of split peaks (e.g. 200/020 and 002 peaks) in the later stages of cold deformation. Thus, it appears as if the process of cold deformation of the $L1_0$-ordered FePd generates a microstructure that has similar X-ray diffraction characteristics to that of the disordered FCC FePd. Such phenomena have been studied previously in other ordered systems and have been referred to as 'mechanical disordering'[78].

The localized observations conducted by TEM (e.g.figures-6.38 and 6.39) add important details that complement the X-ray diffraction measurements. The presence of extremely diffuse intensities in the superlattice rings in the accompanying diffraction pattern in figure-6.39 can be observed after 90% reduction in thickness. This is a direct experimental proof of the presence of some $L1_0$-order in the microstructure after 90% reduction in thickness. In addition, the microstructure sensitive magnetic property (coercivity) measured using VSM after 90% reduction in thickness in the $L1_0$-ordered condition exhibits a value (~200Oe) nearly 4 times higher than that expected for the disordered deformed FCC FePd (~ 50Oe). For bulk FePd such a high value of the coercivity can be obtained only from the ferromagnetic $L1_0$-ordered phase.

Thus, it appears reasonable to conclude that the process of cold deformation in the $L1_0$-ordered phase leads to a reduction of the long range order parameter, while the $L1_0$-ordered structure is maintained to a significant degree in the deformed microstructure.

The disappearance of the superlattice peaks, peak broadening and the approach of the c/a ratio to unity as observed in XRD θ-2θ scans, however, need to be rationalized.

The process of plastic deformation in the $L1_0$-ordered phase can be facilitated by unit dislocations (of the type a/2 [110]) by pairs of superpartial dislocations (of the type a/2 [101] and a/2 [011]). A dissociation of the unit dislocation (of the type a/2 [110]) into two Shockley partial dislocations that are separated by a complex stacking fault (CSF) is energetically favorable[82], based on elastic line energy considerations (Frank's rule).

e.g.

a/2 <-110] → a/6<-211] + CSF + a/6<-12-1].

Similarly, superpartial dislocations can dissociate into Shockley partial dislocations and super intrinsic stacking faults (SISF) and CSF.

e.g.

a/2<0-11] → a/6<-1-12] + SISF + a/6<1-21]

and

a/2<0-11] → a/6<-1-12] + CSF + a/6<1-21].

It can be envisaged that during plastic deformation these dissociated dislocation structures would glide on {111}. Such extended dislocation structures gliding on different {111} can intersect. Unit dislocations dissociated into Shockley partials that are separated by an intrinsic stacking fault have been observed in FCC metals with low SF energy (e.g. Au)[83] . Such extended dislocations gliding on different {111} have also been observed to intersect and produce

superjogs in FCC metals (a superjog is a jog where its height is a multiple of interplanar spacings)[84]. The creation of dislocation lock configurations (such as superjogs), during plastic deformation, has been associated with the generation of point defects, such as structural vacancies in the FCC lattice[84]. It can be envisaged that the different extended dislocation structures in $L1_0$-ordered lattice that, presumably, are gliding on different {111} on intersection can produce superjogs. These superjogs could act as sources of structural vacancies and aid in formation of anti-sites in the $L1_0$-ordered lattice that is closely related to the FCC structure. Similarly, other dislocation configurations (such as the double Lomer-Cottrell barrier as observed in $L1_2$-ordered Ni_3Al[85]) and a multitude of other dislocation configurations that are possible in the $L1_0$-ordered phase could lead to the generation of point defects, such as anti-sites and structural vacancies in the $L1_0$-ordered lattice during plastic deformation. The creation of excess point defects during plastic deformation can lead to the mixing of species on the atomic positions of the ordered A and B sites in the $L1_0$-ordered lattice. In the vicinity of these point defects the $L1_0$-ordered structure (alternating (002) layers of Fe and Pd atoms) would be compromised. Thus, the 'mechanical-disordering' must be related to the production of regions with incorrect nearest neighbor correlations in the $L1_0$-ordered crystal structure that have been mechanistically facilitated by point defects, which are a by-product of the work-hardening processes activated during plastic deformation.

The mixing of atomic species on the two sublattices in the $L1_0$-ordered structure would manifest itself in the reduced intensity of the superlattice peaks. Due to the local loss of chemical order the structure factor for X-ray diffraction to superlattice peaks, in those volumes, would be reduced to zero or closer to zero overall.

The disappearance of the superlattice peaks may also be facilitated by imperfect or partial dislocation activity during cold deformation. An imperfect or partial dislocation may produce thin volumes / layers in the vicinity of its plane of motion that are associated with Fe and Pd atom positions that are not consistent with the rest of the undisturbed $L1_0$-ordered crystal structure. Hence, it could be envisaged that planar fault trailing partial dislocation can have an effect on the structure factor of the superlattice peaks and thus could lower the intensity in these superlattice peaks. As a simplest case the effect of a Shockley partial dislocation (of type a/6 [112]) on the intensity in the superlattice peaks is qualitatively discussed below.

The intensity of a peak in the XRD scan (I) is related to the structure factor (F) by the following equation (ref #80 pg 139)

$$I = |F|^2 * p * \{(1+\cos^2 2\theta) / (\sin^2\theta * \cos\theta)\} * A(\theta) * e^{-2M} \quad 7.1$$

Where θ is the Bragg angle, F is the structure factor for a set of diffracting {hkl}, p is the multiplicity of the diffracting planes, the trigonometric terms are the Lorentz-polarization factor, A(θ) is the absorption factor and e^{-2M} is the temperature factor.

For a given Bragg angle and a given set of diffracting planes, the intensity of the diffraction peak can be related to the structure factor F by

$$I \propto |F|^2 \quad 7.2$$

The structure factor F can be envisaged as the resultant wave that is scattered by all atoms of the unit cell. The unit cell in turn is the repeating unit in the crystal lattice. The structure factor for a given set of diffracting planes {hkl} is given by

$$F_{hkl} = \sum_n f_n e^{2\pi i (hu_n + kv_n + lw_n)} \quad 7.3$$

In this equation u_n , v_n and w_n are the relative positions of the n^{th} atom of the n atoms in the unit cell.

The conventional unit cell that can be used to describe the $L1_0$-ordered γ_1 – FePd has been depicted in figure-7.1a. The relative positions of Pd atoms would be 000 and 1/2 1/2 0 and the positions of Fe atoms would be 1/2 0 1/2 and 0 1/2 1/2 in the unit cell depicted in figure-7.1a. It can be deduced from figure-7.1a that the unit cell used to describe the $L1_0$ -ordered phase is closely related to the unit cell used to describe any other FCC disordered material.

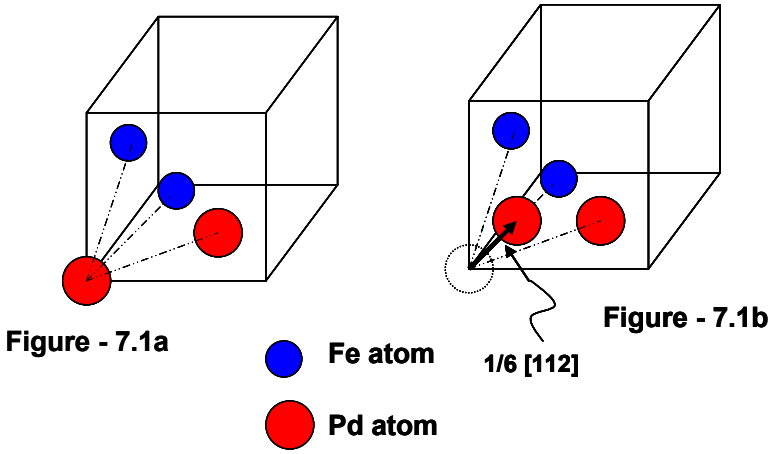

Figure-7.1a Unit cell that can be used to compute the structure factor for $L1_0$-ordered FePd.

Figure-7.1b Displacement (associated with a Shockley partial dislocation) that can cause a change in the relative atomic positions.

Figure – 7.1b depicts an atomic displacement along the 1/6[112] in the conventional unit cell of the $L1_0$-phase (a possible Burgers vector of the Shockley partial dislocation that can aid plastic deformation). Due to such a displacement the relative positions of the atoms in the unit cell (u_n,v_n,w_n in equation 7.3) would change. As a result the structure factor associated with that volume of material that experienced such a displacement would change. This change in the structure factor would be manifested in the intensity of the XRD peaks (equation 7.2) (Appendix – 1 Structure factor determination for different peaks in the $L1_0$-ordered phase).

The presence of strain associated with crystal defects in the lattice (such as individual dislocations, populations of interacting dislocations, excess point defects that are deposited in the lattice) can lead to the broadening of the XRD peaks as has been observed in this study. TEM and VSM observations provide experimental proof for the increasing population of these crystal defects as the % reduction in cold rolling increases.

It has been observed that the c/a ratio changes (from 0.967 to 0.989) as cold deformation progresses in the $L1_0$-ordered condition. This change in the c/a ratio is also accompanied by the 'merging' of the split peaks (e.g. 311 / 131 peak and the 113 peaks). The merging of the splits peaks can be attributed to the peak broadening due to strain that has been imparted into the microstructure. The lattice parameters a and c have been determined from these θ-2θ XRD scans. The 200/020 peak has been used to obtain the lattice parameter a. Using these measurements for a, the lattice parameter c has been determined from the 202/022 and the 111 peaks. The change in the lattice parameters as a function of the processing condition has been depicted in figure-7.2. The error bars have been obtained by considering the absolute differences between the lattice parameters obtained from different peaks. From this figure it can be concluded that the lattice parameters a and c approach the value for the parameter a for the disordered FCC (γ) FePd as cold deformation progresses.

The 'relaxation' of the lattice parameters of the $L1_0$-ordered phase towards the disordered FCC phase is consistent with the increase in point defect content during plastic deformation. Since the equilibrium c/a ratio is less than unity in the $L1_0$-ordered phase (0.966) , it can be deduced that there is a disparity between the interatomic spacing (and the bond strength) between the atoms within a single layer (002) of the $L1_0$-ordered structure (Fe-Fe atom or Pd-Pd atom bonds) compared with Fe-Pd bonds.

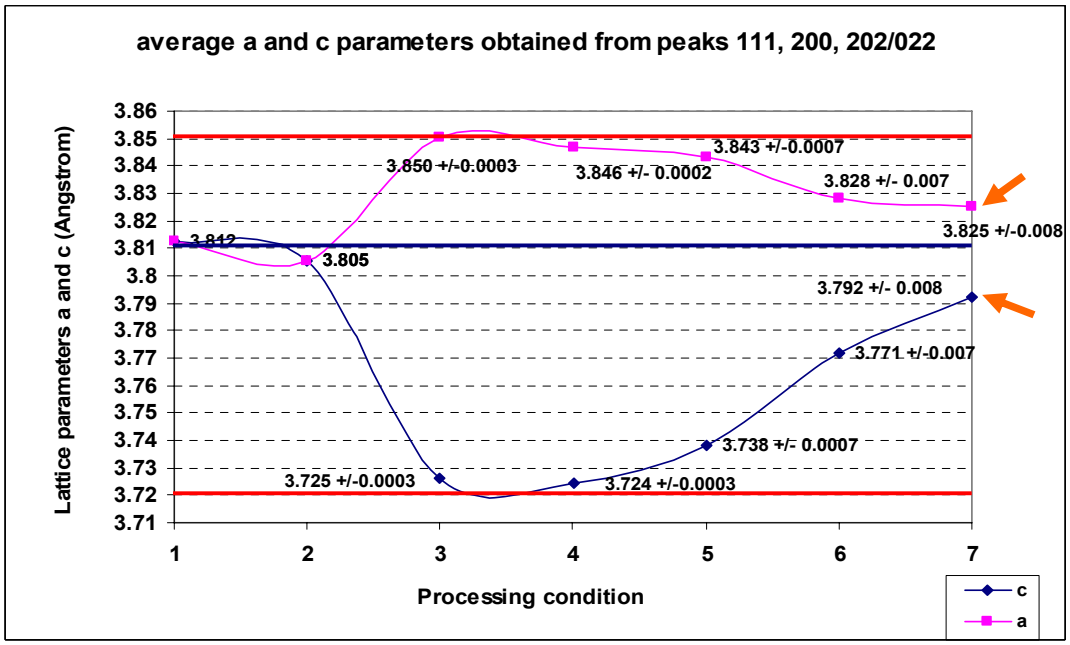

Figure-7.2 Change in lattice parameters a and c as a function of the processing condition. The legend describing the processing condition is also included. The equilibrium lattice parameters for the $L1_0$-ordered FePd and FCC disordered FePd have been delineated by red and blue straight lines. Note: the lines joining the different data points are to guide the eye of the reader.

The equilibrium interatomic spacing for the Fe-Pd bonds appears to be shorter as compared to the Fe-Fe bonds and Pd-Pd bonds between the next nearest neighbors. The presence of a vacancy on a Fe or a Pd lattice site can disrupt these bonds. Due to the absence of a Fe or Pd atom at the lattice site the shortening of the c-axis due to the shorter Fe-Pd equilibrium interatomic bond length, would no longer be possible. This could lead to a relaxation of the lattice. Thus, the generation of excess point defects during cold deformation could be responsible for the c/a ratio approaching unity as cold deformation progresses.

The 'mechanical disordering' phenomenon in equiatomic $L1_0$-ordered FePd has been observed for the first time in this study. A very brief understanding of this phenomenon has been developed in this study as the main intention of this study is to compare and contrast the CR transformation and conventional annealing transformation after cold deformation. The data presented in the previous chapter and the discussion of this data in this chapter provides sufficient comparative information about the starting cold deformed microstructures before annealing experiments. These comparative points are now summarized –

1) The cold deformed $L1_0$-ordered microstructure has a weak cube type texture; the deformed FCC microstructure has a strong brass type texture.

2) The $L1_0$-ordered phase (with a higher c/a ratio than equilibrium) is present after cold deformation in the ordered $L1_0$ (γ_1) FePd. The FCC phase with a c/a ratio of unity is present after cold deformation in the disordered FCC (γ) FePd.

7.2 ATTAINMENT OF A $L1_0$-ORDERED STRUCTURE DURING CR AND CONVENTIONAL ANNEALING

Figure-6.43 depicts θ-2θ XRD scans obtained after annealing for 0.5 hour and 1 hour at 600°C (scans-8 and 9) after 90% reduction in thickness in the $L1_0$-ordered condition (Conventional annealing). The reappearance of the superlattice peaks (e.g. 110) and splitting in the peaks (e.g. 022/202 and 220 peaks) is evident in the scan-8. The lattice parameters a and c have been obtained from the 200/020 peak and the split 022/202 peak respectively. The c/a ratio obtained from these peaks was found to be 0.9640 (+/- 0.003). This value is very close to the equilibrium c/a ratio for the $L1_0$-ordered structure (0.966) and agrees with it in the error margin. Thus, it seems reasonable to conclude that after only 0.5 hour at 600°C the microstructure is again

completely $L1_0$-ordered. The peaks observed in these scans appear to be considerably broader as compared to the peaks observed before the start of the cold deformation process (scan-3 in figure-6.43). Figure-6.45 is a bright field TEM micrograph obtained from the sample that has been conventionally annealed for 1 hour at 600°C. The presence of a large density of dislocations in this microstructure can be observed. These dislocations appear to be arranged in relatively narrow segments in the microstructure. A small fraction of the microstructure (~10 vol %) also appears to consist of relatively defect free, recrystallized, equiaxed $L1_0$-ordered grains. The observation of large density of crystal defects in the microstructure and the presence of broad peaks in the XRD scans are an indication of the presence of strain in the microstructure, even when the c/a ratio achieves an equilibrium value after 0.5 hours at 600°C during conventional annealing.

It is known from studies of annealing phenomena of the disordered solid solution that do not show an ordering transformation (e.g. annealing of cold deformed Cu) that the recovery processes would dominate the microstructural transformation in the initial stages of annealing. Recovery processes are known to annihilate the excess content of point defects and some dislocations present in the microstructure. During recovery, dislocations would undergo conservative motions, such as glide, and non-conservative motions, such as climb (facilitated by vacancies). These motions could lead to recombination events in which dislocations that are associated with opposite stress fields would recombine and annihilate to allow for the reduction of the overall dislocation density. Alternatively, they could also lead to the rearrangement of dislocations into low energy configurations (e.g. formation of LEDS[86]). The processes associated with recovery are all facilitated by short range diffusion and characteristically show an absence

of the generation of new grain orientations in the microstructure that are separated by a high angle grain boundary from the surrounding matrix.

From the TEM and XRD observations it can be concluded that the recovery processes are occurring during the early stages of conventional annealing (0.5 hour and 1 hour at 600°C). It can be concluded that the short range diffusion processes that are sufficient to facilitate recovery are also sufficient for the establishment of the equilibrium c/a ratio. The processes of recovery do not involve the creation of any new interfaces as would be expected in a phase transformation. Thus, the mere rearrangement of atoms over short distances during recovery of the deformed $L1_0$-ordered microstructure leads to the generation of an $L1_0$-ordered structure with c/a ratio close to the equilibrium value and the rapid regaining of the $L1_0$-order. In the previous section the emergence of point defects, such as structural vacancies, anti-sites was proposed to explain the mechanical-disordering phenomena. Thus, the cold-deformed $L1_0$-ordered microstructure could be envisaged as that containing an excess content of structurally induced point defects. The thermal activation provided during the initial stages of annealing can facilitate the diffusion of structurally induced vacancies. Recombination events of these vacancies with atomic species present on the 'wrong' sublattice can allow for the regaining of the layered structure that constitutes the $L1_0$-ordered lattice. In addition, thermal vacancies introduced in the microstructure due to thermal activation would also allow for similar recombination events and would help restore the ordered structure. This proposal is also in agreement with the conclusion drawn in the previous section, in which the deformed $L1_0$-ordered structure (with $c/a \sim 0.99$) was described as a deviation from the ideal $L1_0$-ordered structure caused by local perturbations in the crystal lattice (perturbations due to point defects). These perturbations can be compensated by the short range diffusion processes during recovery and order can be regained.

This observation is in direct contrast with the observation made during CR transformation (after comparable prior strain of cold deformation in the FCC condition). It has been observed that the FCC to $L1_0$ ordering transformation is complete after 3 hours of annealing at 600°C. However, in case of CR the attainment of the $L1_0$-ordered phase (with c/a = 0.966) has been accompanied by the complete transformation of the microstructure. The microstructure in this completely ordered state has been observed to consist almost entirely of new defect free equiaxed $L1_0$-ordered grains (figure-6.5). An attainment of the $L1_0$-ordered phase solely through recovery processes has not been observed in CR transformation. The massive ordering mode (as described in the chapter-2-background) has been observed to facilitate the microstructural transformation leading to new, defect free $L1_0$-ordered grains. This mode involves the heterogeneous nucleation and growth of new $L1_0$-ordered grains at deformation heterogeneities in the deformed FCC parent phase (figure-6.7). As has been described in the background chapter, the massive ordering mode is a distinctively different process by which order is established in the microstructure as compared to the recovery processes that lead to regaining of the order during conventional annealing.

Thus to distinguish between both modes of transformation

1) Recovery processes facilitated by short range diffusion are sufficient to regain order in conventional annealing, whereas a massive ordering mode involving a FCC to $L1_0$ -ordering phase transformation is required to establish an $L1_0$-ordered microstructure during CR.

2) The kinetics of regaining of order during conventional annealing are much faster as compared to the kinetics of the establishment of order via massive ordering mode in CR transformation. This is consistent with re-ordering during conventional annealing involving short-range diffusion

facilitated atomic rearrangements that are more rapidly accomplished than the nucleation and growth processes required for ordering in the CR transformation.

7.3 THE ATTAINMENT OF A COMPLETELY EQUIAXED MICROSTRUCTURE – CR VS. CONVENTIONAL ANNEALING.

7.3.1 Texture Evolution

Figure-6.3 and figure-6.5 depict the microstructures in the cold deformed FCC phase and the CR transformed $L1_0$-ordered phase. Figure-6.4 and figure-6.6 depict the phi2 constant sections of the ODF in the cold deformed FCC and the CR transformed $L1_0$-ordered phase. From these TEM and XRD observations it can be concluded that the main texture component (Brass component in the phi2 = 0° constant section) is inherited from the cold deformed FCC into the CR transformed $L1_0$-ordered phase. This inheritance occurs even when the microstructure transforms from a heavily defected FCC phase to CR transformed equiaxed grained $L1_0$-ordered phase. The inheritance of texture components signifies the presence of similar crystallographic orientations in the deformed FCC and the CR transformed $L1_0$-ordered microstructure.

During the massive ordering mode that facilitates CR transformation, preferential nucleation and growth of $L1_0$-ordered grains at deformation heterogeneities in the FCC deformed matrix has been observed (figure-6.7). The emergence of low angle grain boundaries as the FCC / $L1_0$ interphase interfaces has also been observed (figure-6.9 and 6.10). Statistically significant measurements showed that large fraction (~92%) of interphase interfaces are low angle grain boundaries. Thus, the presence of low angle grain boundaries would allow for the approximate inheritance of the crystallographic orientation from the cold deformed FCC grains into the CR

transformed $L1_0$-ordered grains. This would lead to similar texture signatures in the ODF as has been observed in this study.

The observation of the low angle grain boundaries as interphase interface during CR transformation can be rationalized based on a kinetics argument. Figure-7.3 is a schematic depicting the massive ordering mode in CR transformation.

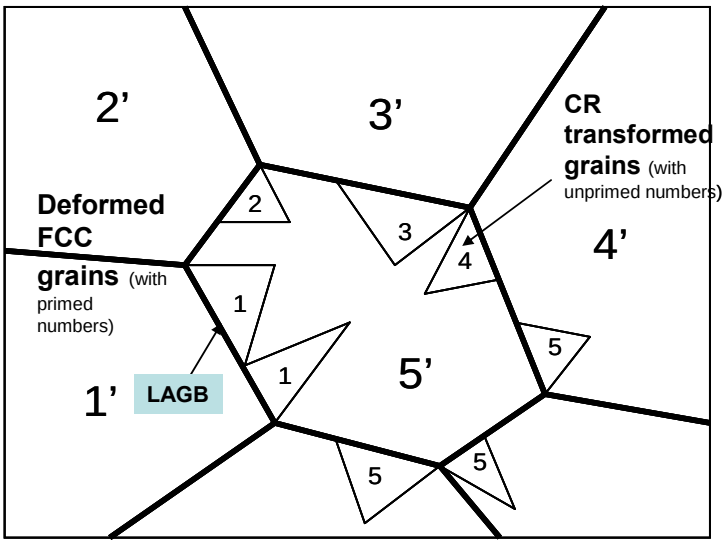

Figure-7.3 Schematic depicting the heterogeneous nucleation and growth of $L1_0$ -ordered grains in the deformed FCC matrix.

As has been depicted in the schematic in figure-7.3 the FCC to $L1_0$ ordering transformation would occur by heterogeneous nucleation and growth of $L1_0$-ordered grains. The FCC to $L1_0$ ordering, a thermodynamically first order phase transformation, would be associated with an activation energy barrier (ΔG^*). This activation energy barrier is directly proportional to the energy penalty incurred by the system in creating an interphase interface ($\sigma_{FCC\ /\ L1_0}$). The relationship can be written as[33]

$$\Delta G^* \propto \sigma^3_{FCC / L1o.} \quad 7.4$$

The energy penalty associated with the interphase interfaces that are low angle boundaries would be much less as compared to creating interphase interfaces that are high angle boundaries, except for some special cases, e.g. high coincidence site HAGBs. Hence, to first approximation

$$(\sigma_{FCC / L1o})_{LAGB} < (\sigma_{FCC / L1o})_{HAGB} \quad 7.5$$

Due to a smaller activation energy barrier in the presence of LAGBs as interphase interfaces, the FCC to $L1_0$ ordering phase transformation would be favored at many locations in the microstructure, which provide for such configurations. Thus, this would enable the system to maximize the rate of dissipation of excess free energy that is stored in the deformed metastable FCC microstructure ($\Delta G_{metastable\ FCC \rightarrow stable\ L1o}$).

The emergence of a large fraction of LAGBs as interphase interfaces would be kinetically favorable and hence these boundaries characteristically emerge during CR transformation leading to texture inheritance.

A similarity in texture signatures has also been observed during conventional annealing. However, the rationalization of this similarity in texture signatures appears to be completely different than that for the CR transformation. Figures-6.42 and figure-6.51 depict the phi2 constant sections of the ODF after cold deformation to 90% reduction in thickness in the $L1_0$-ordered condition and after annealing for 8 hours at 600°C after the cold deformation (completion of recrystallization) respectively. The cube texture component appears to be the dominant texture component in both of these conditions However, the maximum in the intensity of the texture component (times random) are not very strong (~ 4 and 6 respectively). Figure-6.44 is a phi2 constant section of the ODF obtained after annealing for 1 hour at 600°C after cold deformation in $L1_0$ condition. The cube component also appears to be the dominant texture

component in this condition (~ 33 times random). Moreover, the texture signature appears to be sharp with little or no spread in intensity in the vicinity of the ideal cube component signature. From figure-6.45 it can be concluded that recovery processes are dominant in the microstructure after 1 hour at 600°C. The recovery processes appear to strengthen the cube texture which is already present in the prior cold deformed condition. This would be in agreement with expectations as recovery processes would lead to reduction in the dislocation density via rearrangement and annihilation processes only. The reduction in dislocation density and point defect concentration would aid in sharpening of the texture signature. Figure-6.46 offers additional experimental proof for the presence of cube component in the recovering microstructure. Creation of new $L1_0$-ordered grains by the process of recrystallization starts to dominate the microstructural transformation during annealing for times longer than 1 hour at 600°C. Figures-6.47 and 6.48 depict the partially recrystallized microstructure after annealing for 3 hours at 600°C. Approximately 40 vol% of the microstructure appears to have recrystallized after annealing for 3 hours at 600°C. Moreover, it can also be concluded from figure-6.48 that the new recrystallized $L1_0$-ordered grains are separated by high angle grain boundaries from the deformed $L1_0$-ordered matrix. Thus, the new recrystallized $L1_0$-ordered grains have a different orientation as compared to the surrounding deformed matrix. The creation of new orientations in the microstructure during recrystallization is also reflected in the phi2 constant section of the ODF obtained after annealing for 3 hours at 600°C (figure-6.49). While the cube component is still the significant component after 3 hours at 600°C, the maximum in intensity appears to have reduced to only 4 times random from 33 times random observed after annealing for 1 hour at 600°C. The generation of such new orientations in the microstructure during recrystallization continues with increasing annealing time and finally yields a completely recrystallized

microstructure (after 8 hours at 600°C) that has the cube component as the significant texture component, but with an intensity of only approximately 6 times random.

In summary during conventional annealing the weak cold deformed texture is inherited and even strengthened in the microstructure during the recovery stage. The recrystallization proceeds by creation of new orientations in the microstructure and leads to a weakening of the cube texture.

Thus, it is now possible to compare the attainment of the microstructure consisting of new $L1_0$-ordered equiaxed grains via CR and Conventional annealing. The massive ordering mode that facilitates CR allows for an inheritance of texture from the cold deformed FCC into the CR transformed $L1_0$ phase. The recrystallization process that facilitates the formation of new $L1_0$-ordered grains in conventional annealing leads to a diminution of the prior texture.

7.3.2 Kinetics of Transformation

It is now possible to compare the kinetics of the processes that lead to a completely equiaxed $L1_0$-ordered microstructural state after transformation in the CR mode and the conventional annealing mode. The CR transformation is complete and a nearly entirely equiaxed $L1_0$-ordered microstructure obtains after 3 hours of annealing at 600°C. In contrast, 8 hours of annealing at 600°C is required to achieve a similar microstructural state during conventional annealing after comparable strain of cold deformation. Thus, the CR mode of transformation appears to be faster as compared to the conventional annealing mode in attaining an equiaxed $L1_0$-ordered grain morphology in the microstructure.

This observation can be rationalized using the Burke-Turnbull approach to kinetics of a transformation[8]. In the first approximation the velocity of a moving interface V can be given as a

product of two terms, mobility of the interface (which is closely related to the mobility of atoms) at the temperature of transformation (μ) times the driving force for the transformation (ΔG). (An 'average' interface is considered, special interfaces such as the coherent {111} would have to be treated differently)

$$V \propto \mu * \Delta G \qquad 7.6$$

In case of the CR transformation, two driving forces can be prominently identified

1. The driving force associated with the reduction in defects stored in the cold deformed FCC phase (ΔG_{CW})

2. The driving force associated with the FCC to $L1_0$ ordering transformation ($\Delta G_{FCC \rightarrow L1o}$).

In case of the conventional annealing, it has been previously established that the process of recovery leads to regaining of order in the deformed $L1_0$-ordered phase. Thus, the reduction in defect content introduced in the $L1_0$-ordered phase appears to be the most prominent driving force for recrystallization to occur during annealing (ΔG_{CW}). Both of these conditions have been schematically depicted in figure-7.4

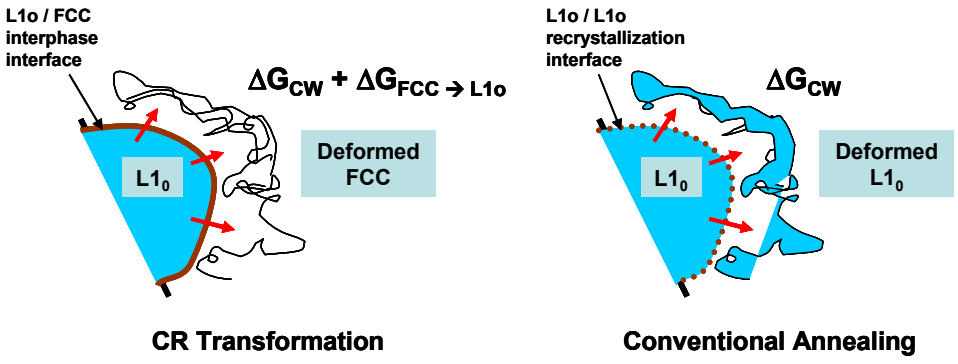

Figure-7.4 Schematic representation of CR transformation and Conventional Annealing.

As has been depicted in figure-7.4 CR transformation is known to be driven by two dominant driving forces. Under the influence of both of these driving forces, during CR transformation, lattice and boundary diffusion of atoms through the disordered FCC phase would occur to the $L1_0$ / FCC interphase interface. This process would be followed by the attachment of atoms onto the interphase interface. This attachment would be such that the layered structure of the $L1_0$-ordered phase is attained. As the interphase interface moves, it would also replace the deformed metastable FCC phase by the relatively defect free $L1_0$-ordered phase. In contrast, during conventional annealing the lattice and boundary diffusion of atoms would occur through the $L1_0$-ordered phase. The stored strain energy of cold work would be the single dominant driving force. Atoms can attach to the recrystallization interface and promote the growth of the new recrystallized relatively stress free $L1_0$-ordered grain that is sweeping the defect content in front of the recrystallization interface. It is known that the mobility of atoms in the $L1_0$-ordered phase would be lower as compared to the mobility of atoms in the disordered FCC phase[87,88]. These differences in the mobility of atoms can be traced to the differences in mechanisms of diffusion in the disordered FCC and $L1_0$-ordered structure[89]. The requirements of maintaining a layered structure even when diffusion of atoms (facilitated by vacancies, antisites) is occurring, makes the process of diffusion more difficult in the $L1_0$-ordered structure as compared to the FCC structure. Thus, at a given temperature of transformation the mobility of atoms in the FCC phase would be higher as compared to the $L1_0$-ordered phase.

From the above discussion it can be concluded that both the mobility of the atoms (and therefore the mobility of the interface) and the driving force for the CR transformation are higher as compared to the conventional annealing transformation. Thus, using the approach described by equation 7.6 it can be concluded that the velocity of the moving interface would be higher

during CR transformation as compared to conventional annealing. In the presence of interfaces that have a higher velocity than their counterparts in the conventional annealing transformation, it appears reasonable to conclude that the kinetics of transformation are faster during CR as compared to conventional annealing and the experimental observations support this conclusion.

7.4 GRAIN GROWTH AFTER CR TRANSFORMATION AND DURING CONVENTIONAL ANNEALING

Figure-6.31 is a phi2 constant section of the ODF obtained after annealing for 8 hours at 600°C after 97% reduction in thickness in the FCC condition. It has been established previously that the CR transformation was complete essentially after annealing for 3 hours at 600°C and the microstructure consisted almost entirely of new $L1_0$-ordered grains. Thus, the microstructural state represented by figure-6.31 has been obtained after 5 hours of grain growth (8h-3h = 5h) in the $L1_0$-ordered condition at 600°C. The cube component appears to be the dominant texture component with the maximum intensity in the ODF close to 48 times random. The presence of the dominant cube component during grain growth has also been independently confirmed using OIM in the SEM. Figures-6.32 and 6.33 are a number fraction-rotation angle chart for grain boundaries and the corresponding MDF obtained for a sample that has been annealed for 14 hours at 600°C (Grain growth for 11 hours). A large number fraction (~40%) of boundaries can be seen to be associated with 90° misorientation between the two grains they separate. From the MDF it can also be discerned that the cube axes are the preferred rotation axes. These observations confirm the dominance of cube component during grain growth after CR.

Figures – 6.58, 6.61 and 6.62 are the phi2 constant section of the ODF obtained after 16 hours of conventional annealing at 600°C (8 hours of grain growth) and a grain boundaries rotation

chart and a MDF obtained after 24 hours at 600°C (16 hours of grain growth) respectively. During grain growth the preferential emergence of boundary segments with cube axes as the rotation axes has also been established using OIM data sets (figures-6.63a to 6.63d). From these observations it can be concluded that there is a dominance of cube component during grain growth in conventional annealing as well. Thus a similarity in texture evolution during grain growth after CR transformation and conventional annealing could be identified.

The reduction in the interfacial free energy is the significant driving force for the process of grain growth. The system would preferentially try to establish interfaces that have a higher mobility that can maximize the rate of grain growth. Mechanisms such as twinning have been observed to facilitate the creation of such high mobility interfaces in FCC materials. In addition, the system could also choose to lower the overall interfacial free energy by replacing the high energy interfaces by special boundaries that have a much smaller energy penalty associated with them[90].

The $L1_0$-ordered monophase microstructures are observed during grain growth after CR and during conventional annealing. It is known that the lattice parameters a and c of the tetragonal structure differ by approximately 3%. Previous studies[2] have shown that the three dimensional arrangement of crystals that have such a lattice mismatch, under the constraint of reduction of the overall strain energy, can lead to the formation of the polytwin microstructure. The polytwin microstructure can be thought of as a system of micro and macro twins that have the dodecahedral {101} as the conjugation plane. The twins are arranged such that the two crystal lattices on either side of the twin boundary can be brought into correspondence by an approximate 90° (88°) rotation with the common cube axis being the rotation axis. The relative arrangement of different atoms in the twin and matrix in the polytwin structure has been depicted

in appendix-2. As can be seen from figure-A2.1 atomic species matching across the polytwin {101} type interface can be achieved. To obtain a coherent {101} interface a shear along the <10-1> would be required (ref#2, pg 28). It is also known that elastic lattice shear on {101} in <10-1> is energetically favored. This being due to the smaller value of the shear modulus on {101} in the <10-1> as compared to other directions[91], leading to the smallest shear strain energy contribution to the overall energy of the interface. Thus, dodecahedrally {101} conjugated polytwin boundaries are low energy coherent boundary segments that depict good lattice matching across the interface. They are special boundaries that the system prefers under the constraint of minimization of the overall strain energy associated with filling three dimensional space with different orientations of the $L1_0$-ordered tetragonal structure.

It is also known that any one of the cube axes of the FCC phase can transform into the c-axis of the $L1_0$-ordered phase. Thus, three variants of the $L1_0$-ordered phase can form. It is known that during coarsening of the polytwin microstructure, the coherent {101} twin boundary between the two favorably oriented variants (variants that compensate for each other's strain fields) increases in area. In the process the third variant is consumed. Thus locally variant selection occurs that leads to strain minimization and formation of the polytwin morphology.

During the grain growth regime after CR and during conventional annealing long boundary segments that are able to establish a 90° rotation relationship between neighboring grains start to dominate. The cube axes can also be identified as their rotation axes. The 90° boundaries are observed between large grains and they are mostly absent between small grains. The large grains that have such 90° rotation relationship appear to be growing and consuming the smaller grains surrounding them. Thus, similar to the coarsening behavior of the {101} type twins, during grain growth, the system appears to prefer the 90° boundaries that allow the minimization of the

overall strain energy associated with filling of three dimensional space with different orientations of the $L1_0$ -ordered tetragonal structure. The preference exhibited by the system towards such orientations during grain growth is reflected in the dominance of cube texture during the grain-coarsening regime of the microstructural transformation.

7.5 FORMATION OF DEFECTS DURING CR TRANSFORMATION AND DURING CONVENTIONAL ANNEALING

7.5.1 Formation of Defects during CR and during Recrystallization Regime of Conventional Annealing

7.5.1.1 Formation of Stacking Faults and Octahedral {111} type Twins Two different morphologies of twins have been prominently observed during the massive ordering mode of the CR transformation. The octahedral {111} type twins that are heavily defected and emanate from the FCC / $L1_0$ interphase interface of the CR transformed grains (e.g. figures-6.11) is one of these morphologies. The other morphology is depicted in figure-6.18 and involves the nucleation and growth of the twin variants on relatively immobile {111} facets of the CR transformed grains that are growing into the defected FCC matrix.

The habit planes of the arrays of SF's and apparent μT's produced during CR transformation (depicted in figure-6.11) have been determined to be octahedral {111} planes using TEM tilting experiments. The dark field (DF) TEM micrograph of figure-6.14 shows the partial dislocations that bound the overlapping SF's emerging from the grain boundary of the CR transformed grain. The contrast features of the planar defects emanating from the grain boundary are consistent with those of cascades of overlapping SF's or SF arrays on octahedral planes of the mono-variant $L1_0$-ordered grain. The most likely Burgers vector of the SF generating Shockley partials would be of

the type b=1/6<112>, which can generate a proper octahedral twin in the $L1_0$-structure[58]. A suitable mechanism for the formation of the SF arrays at the migrating grain boundary can be proposed in analogy to the classic Dash-Brown mechanism for formation of annealing twins in FCC solid solutions[48]. The geometric arrangement of Shockley partial loops bounding stacking faults that emanate from the grain boundary has been previously elucidated by Mahajan et al[49], which is schematically reproduced in figure-7.5.

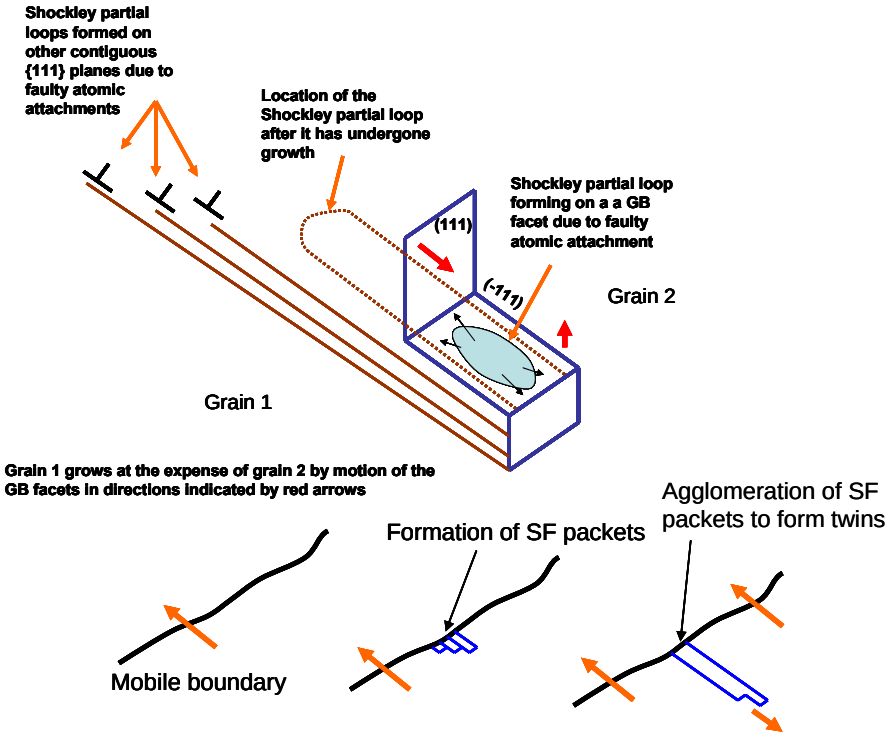

Figure-7.5 Schematic depicting the possible mechanism for the formation of internally faulted twins during CR transformation[49]

The SF cascades are bound by Shockley partial loops as observed in figure-7.5, which form on parallel {111}-facets at the transformation interface and mutually repel due to elastic

interactions, dragging out ribbons of SF into the growing grain. This mechanism is also suitable to generate internally faulted μT's on {111} in $L1_0$-ordered FePd if the cascades of parallel SF's emanating from the mobile interface become sufficiently thick and dense. The attachment faulting process for twin formation at mobile interfaces observed here is very similar to that reported previously for SF and twin genesis in massively transformed $L1_0$-ordered τ-MnAl [50].

The emergence of the other morphology of {111} twins (figure-6.18) can be rationalized based on a kinetics argument. The {111} facets of the $L1_0$-ordered CR transformed grains are immobile interfaces. As has been previously described, the massive ordering mode proceeds by the motion of the FCC / $L1_0$ interphase interface. Atomic attachment occurs to this interface leading to the increase in the volume of the $L1_0$-ordered grain at the expense of the disordered deformed FCC matrix. During CR transformation the formation of the immobile {111} facets would slow the FCC to $L1_0$ ordering massive transformation. The system prefers to maximize the rate of the dissipation of the excess free energy associated with the FCC to $L1_0$ ordering transformation. To achieve an enhanced rate of transformation, the system prefers highly mobile interphase boundaries. Thus, the nucleation and growth of a new twin variant occurs on the stalled, immobile {111} interface. This topotectic nucleation event is such that the low energy coherent {111} facet acts as the interface between the two grains. The remaining grain boundary segment (or rather FCC / $L1_0$ interphase interface) is a non-coherent boundary segment that has a much higher mobility as compared to the {111} facet. Thus, by nucleating and growing a new {111} twin variant the system can 'jump-start' the stalled CR transformation and maximize the rate of dissipation of the excess free energy ($\Delta G_{FCC \rightarrow L1_0}$).

The observations of the emergence of twins during CR transformation can now be compared with the observations of twins during the recrystallization regime of conventional annealing.

Figure-6.52 depicts the emergence of different morphologies of twins during the recrystallization regime. Microtwins appear to be dominantly present in this representative microstructure. In addition, grains that have a matrix and twin type relationships can also be observed (figure-6.53a and 6.53b). Extremely defected cascades of stacking faults can also be seen to emerge from the recrystallization boundary segments. These stacking faults and twin morphologies are similar to those observed during CR transformation. However, they have higher dislocation content as compared to the stacking faults and twins observed during CR transformation.

The emergence of similar morphologies of these planar defects during both of the transformations suggests similarities in the mechanisms for formation of these defects. However, the differences in driving forces for both of these transformations is manifest in the microstructure in the form of the residual defect content after transformation. Under the influence of higher overall mobility and a driving force that is nearly twice the magnitude compared to conventional annealing[92] the CR interface is able to effectively sweep out nearly all of the defect content introduced in the microstructure during cold deformation. This does not appear to be the case during recrystallization regime of conventional annealing. The lower mobility of atoms in the $L1_0$-ordered phase accompanied by the smaller driving force for transformation manifests into a higher residual dislocation content during recrystallization.

7.5.1.2 Formation of Antiphase Boundaries Figure-6.22 and figure-6.23 depicted the generation of APBs in the small fraction (~5 vol %) of the microstructure transformed by the conventional ordering mode and the new CR transformed $L1_0$-ordered grain respectively.

The impingement of $L1_0$-ordered domains during the process of formation of the polytwin microstructure can lead to a disregistry between the atomic layered structure across the impingement interface. This disregistry can be characterized by a superpartial dislocation that

can be associated with a lattice displacement. This lattice displacement is such that it would cause the reversal of site occupancies for the Fe and Pd atoms across the interface. Thus, an antiphase boundary would be created. This mechanism has been previously cited as a mechanism for the formation of APBs in the conventionally transformed microstructure[2] and has also been observed in this study in the extremely small volume fraction of the microstructure that transforms by the conventional ordering mode.

APBs have also been observed in the CR transformed $L1_0$-ordered grains. Figure-6.23 is a representative example of such APBs. APBs emerging from grain boundary segments can be potentially rationalized by a growth accident model. It can be envisaged that during the massive ordering transformation the FCC / $L1_0$ interphase interface of the CR transformed grain moves into the deformed FCC matrix. As atoms attach to the mobile interphase interface, attachment faults can result. These attachment faults can lead to the creation of a superpartial dislocation in the grain boundary plane. As the grain boundary segment propagates into the deformed FCC matrix the superpartial dislocation can be deposited into the $L1_0$-ordered grain while it trails an APB segment that terminates on the interphase interface. Most of the APBs observed during CR transformation appear to be terminating on the grain boundaries. It seems most likely that the growth accident model can be satisfactorily used to explain the generation of these types of APB segments.

APBs emerging from grain boundaries of the recrystallized grains have also been observed during conventional annealing. Figure-6.54 is a representative example of the emergence of such APBs. The growth accidents model can also be applied to rationalize the emergence of these APB segments. No APB segments generated due to impingement of ordered domains (as observed in some small fractions during CR transformation) were observed in the deformed $L1_0$-

ordered matrix. This provides additional proof to the conclusion that the order is regained during the recovery regime of conventional annealing by atomic rearrangements over few lattice displacements. During conventional annealing there is no creation of an FCC / $L1_0$ interphase interface (associated with small ordered domains), the propagation of which might facilitate creation of an $L1_0$-ordered region.

The comparison of the emergence of crystal defects, such as APBs, can thus help in evaluating the conclusions drawn in the previous section and further aid in creating a distinction between the two different modes of CR transformation and conventional annealing.

7.5.2 Formation of Defects (SFs, Twins) during Grain Growth after CR and during Conventional Annealing.

Figure-6.25 depicts different morphologies of twins that emerge during the grain growth regime after CR transformation. Twins terminating within the grain, microtwins, twin lamellae that are of nearly the same size as the matrix are some of the prominent morphologies that are observed in the microstructure. These morphologies are very similar to the twin morphologies that have been observed during annealing of FCC metals[48]. Figures-6.26 and 6.27 also aid in comparing the twins observed during grain growth after CR transformation with the twins observed during the massive ordering mode of the CR transformation. From these figures it can also be qualitatively concluded that the twins observed during grain growth have much lower dislocation content as compared to the twins observed during the massive ordering transformation. From the FFT in figure-6.27 and the diffraction pattern in figure-6.29 it can be concluded that these are true-order twins. The arrangement of atomic columns in these true-order twins has been depicted in figure-7.6. Other twin morphologies such as the pseudo-twin (the matrix and twin show a 60°

rotation across the common [111]) and the order rotation variant (120° rotation across the common [111]) have not been observed in this study.

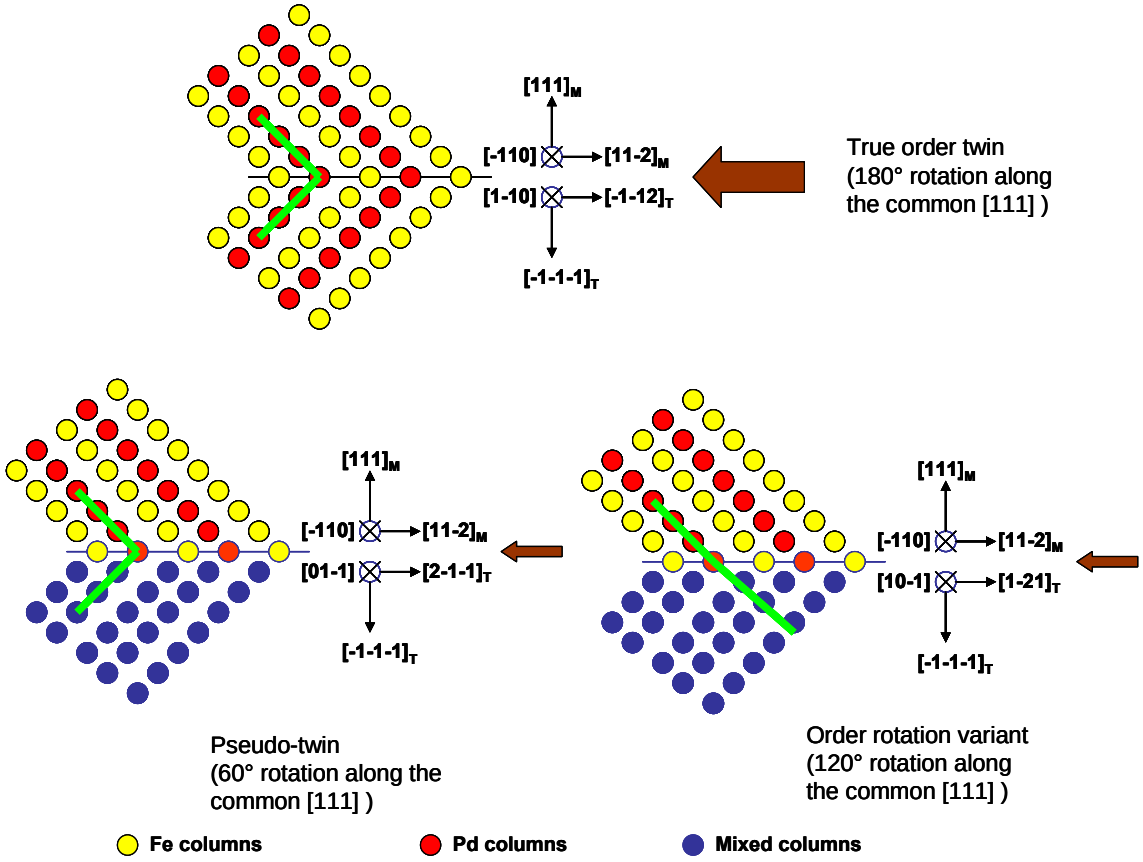

Figure-7.6 The arrangement of atomic columns in different octahedral {111} twins possible in tetragonal $L1_0$-ordered FePd.

Various mechanisms / models have been previously proposed to explain the generation of grain growth twins in FCC metals. The observations made in this study provide evidence that can be used to rationalize the emergence of grain growth twins based on these models.

A growth accident mechanism[93] which was further modified by Gleiter[94] can be used to explain the generation of some of the true order twin morphologies. This mechanism has been schematically depicted in figure-7.7.

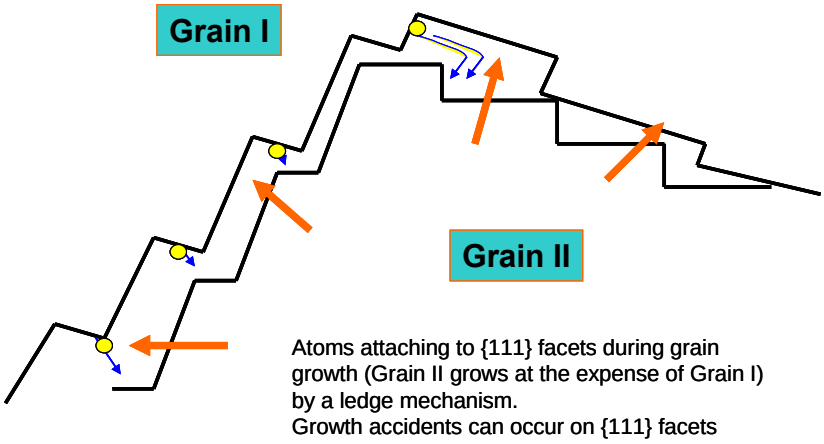

Figure-7.7 Schematic depicting the Gleiter model for true-order twin generation during grain growth.

This model is based on the idea that grain boundaries migrate by a ledge mechanism. A lateral migration of a ledge produces a forward movement of the boundary. For example during the process of grain growth depicted in figure-7.7 grain II is growing at the expense of grain I. Atoms migrate from the step edges (ledges) of grain I to the ledges in grain II. In this model these ledges were assumed to be {111}. As atoms attach to these ledges stacking accidents can occur leading to faulted stacking sequence, creating a coherent twin boundary.

Figure-6.28 is a bright field TEM micrograph depicting the generation of {111} ledges that are few nanometers tall on the grain boundaries of the $L1_0$-ordered grain. It can be envisaged that atomic attachments as illustrated in figure-7.7 can occur onto these {111} ledges and these

attachments would facilitate grain growth. Attachment faults can occur on these ledges and in accordance with the Gleiter model can produce coherent {111} twin boundaries.

A variation of the original growth accidents model[95] can also be used to explain the generation of the microtwin segments. Figure- 7.8 is a schematic that depicts this model.

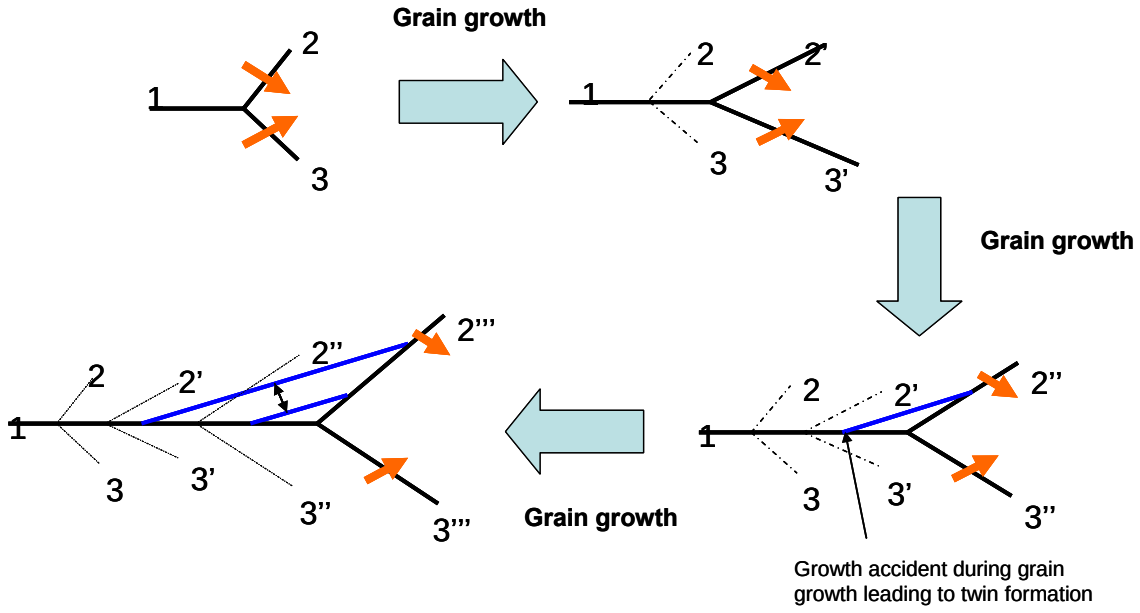

Figure-7.8 Schematic depicting the growth accidents model for true-order twin generation during grain growth.

In figure-7.8 the grain boundary 1 is increasing in area as grain growth proceeds by the motion of grain boundaries 2 and 3. The new locations of the grain boundaries 2 and 3 during grain growth have been indicated by primed numbers. As grain growth proceeds and the area of the boundary 1 increases, growth accidents can occur that can lead to twin formation events as have been depicted in figure-7.8. Such growth accidents can lead to formation of microtwins that run across the entire grain and terminate on another boundary segment.

Figure-6.29 and 6.30 are representative examples that depict the emergence of microtwins during the grain coarsening regime after CR transformation. These microtwins run across the entire grain and terminate on another boundary segment. They have the widths of few nanometers and are most likely formed by the growth accidents model depicted in figure-7.8. Microtwins emerging during grain growth during conventional annealing (figure-6.57) exhibit similar morphology as those observed during grain growth after CR. They can also be rationalized by a similar growth accidents model.

From these examples it appears feasible to conclude that similarities exist among the morphologies of twins observed during grain growth after CR transformation and during conventional annealing. Post-mortem observations conducted in this study suggest similarities in mechanisms that could lead to formation of grain growth twin morphologies.

It is for the first time in this study that a comparison between the two distinct modes of CR transformation and conventional annealing in the equiatomic FePd has been achieved. Vital differences between the two modes of transformations (such as mechanisms of formation of an ordered microstructure, kinetics of transformations etc.) have been elucidated for the first time. Similarities between them (such as grain-coarsening, defects formation) have also been recognized. Thus, using the observations in this study in tandem with previous studies[2,30] it is now possible to develop a coherent framework that can be used to analyze the microstructural evolution during annealing of deformed intermetallics that show an ordering transformation. The possible reaction paths that could aid in microstructural transformation have been depicted in appendix-3.

8.0 CONCLUSIONS

Based on the results and analysis of this study, the following conclusions can be drawn regarding the CR transformation and conventional annealing of cold deformed equiatomic FePd.

1. The cold rolling of the disordered FCC (γ) FePd and $L1_0$-ordered tetragonal (γ_1) FePd to comparable % reduction in thickness leads to considerably different crystallographic textures. The strong brass component dominates the FCC deformation texture, whereas a weak cube component is present in the $L1_0$-phase deformation texture.

2. The cold deformation in the equiaxed $L1_0$-ordered condition leads to a microstructure that has a c/a ratio higher than the equilibrium c/a ratio for the $L1_0$-ordered phase. The cold deformed $L1_0$-ordered phase and the disordered FCC phase are two distinctively different entities, although they appear to possess similar X-ray diffraction characteristics (in powder diffraction mode)

3. The perturbation of the $L1_0$-ordered unit cell due to small atomic displacements associated with lattice dislocations and excess point defects (structural vacancies, antisites) created during cold deformation can be used to justify the absence of superlattice peaks and inability to discern peak splitting in the XRD scans (in powder diffraction mode).

4. Recovery processes that are facilitated by short range atomic diffusion are sufficient to regain a microstructure with the c/a ratio close to unity after cold deformation in the $L1_0$ -ordered condition. The establishment of an $L1_0$-ordered microstructure facilitated only by recovery processes is not observed during CR transformation.

5. The regaining of order facilitated by recovery processes has faster kinetics in conventional annealing as compared to the kinetics of establishment of an ordered structure via the CR transformation route from the metastable deformed FCC phase.

6. Inheritance of crystallographic orientations from the deformed FCC grains into the new $L1_0$-ordered grains leads to similarity of texture in these two conditions during CR transformation. In contrast, during conventional annealing new recrystallized $L1_0$-ordered grains are formed in the deformed $L1_0$-ordered matrix. These new grains do not inherit the crystallographic orientations from the deformed matrix.

7. The kinetics of the massive ordering mode of transformation that is able to establish a nearly completely equiaxed $L1_0$-ordered grain morphology during CR transformation are faster as compared to the kinetics of the recrystallization process during conventional transformation that leads to an equiaxed $L1_0$-ordered grained microstructure.

8. The processes of grain coarsening after the massive ordering mode in CR transformation and after recrystallization in conventional annealing, both lead to the generation of a dominant cube component in the microstructure.

9. The emergence of the cube component during grain coarsening can be rationalized based on the similarity to the coarsening behavior of the dodecahedral {101} type polytwins. During grain coarsening, the system appears to prefer the 90° (low energy) boundaries that allow the minimization of the overall strain energy associated with filling three dimensional space with different orientations of the $L1_0$-ordered tetragonal structure.

10. The twins that emerge during CR transformation and during recrystallization in conventional annealing are true order twins (180° rotation about the common <111>). The presence of the pseudo twins (60° rotation along the common <111>) and order rotation variant (120° rotation along the common <111>) could not be experimentally confirmed.

11. The 'stacking fault packets' mechanism can be used to rationalize the emergence of the defected twins in the partially CR transformed microstructure. This mechanism can also be used to rationalize the generation of defected twins in the recrystallized $L1_0$-ordered grains during conventional annealing.

12. Topotectic nucleation and growth of true order twins on immobile {111} facets of $L1_0$-ordered grains, that enables the system to maintain a high rate of dissipation of excess free energy could be experimentally confirmed during CR transformation. Such topotectic nucleation and growth events were not observed during recrystallization regime of conventional annealing.

13. The growth accidents mechanism (The Gleiter model as well as the Fullman and Fischer model) can be used to rationalize the emergence of true order twins during grain coarsening after CR transformation and after recrystallization in conventional annealing.

14. A growth accidents model can also be used to rationalize the emergence of anti-phase boundaries during CR transformation and during conventional annealing in the recrystallization stage.

APPENDIX-1

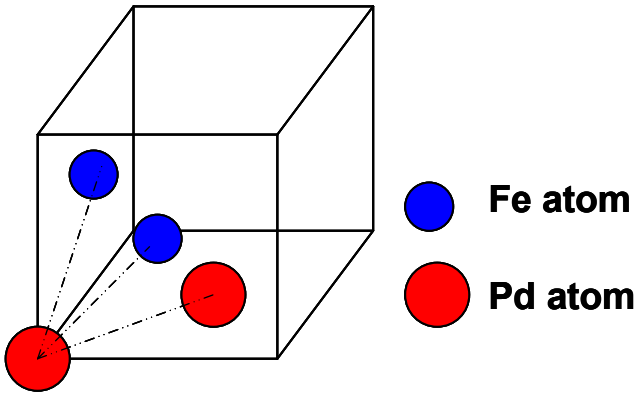

Figure-A1.1 Unit cell that can be used to compute the structure factor for $L1_0$-ordered FePd.

$I \propto | F |^2$

$F_{hkl} = \sum_n f_n \, e^{2\pi i \, (hu_n + kv_n + lw_n)}$

$F_{hkl} = f_{Pd} \, e^{2\pi i \, (0)} + f_{Pd} \, e^{2\pi i \, (h/2 + k/2)} + f_{Fe} e^{2\pi i \, (h/2+l/2)} + f_{Fe} e^{2\pi i \, (k/2 + l/2)}$

Superlattice 001

$F_{001} = f_{Pd} * 1 + f_{Pd} * 1 + f_{Fe} * e^{\pi i} + f_{Fe} * e^{\pi i} = 2(f_{Pd} - f_{Fe})$

$I_{001} \propto | F_{001} |^2 = \mathbf{4 \, | \, (f_{Pd} - f_{Fe}) \, |^2}$

Superlattice 110

$F_{110} = f_{Pd} * 1 + f_{Pd} * e^{2\pi i} + f_{Fe} * e^{\pi i} + f_{Fe} * e^{\pi i} = 2(f_{Pd} - f_{Fe})$

$I_{110} \propto \eta^2 \mid F_{110} \mid^2 = \mathbf{4\eta^2 \mid (f_{Pd} - f_{Fe}) \mid^2}$

Fundamental 111

$F_{111} = f_{Pd} * e^{2\pi i} + f_{Pd} * e^{2\pi i} + f_{Fe} * e^{2\pi i} + f_{Fe} * e^{2\pi i} = 2(f_{Pd} + f_{Fe})$

$I_{111} \propto \mid F_{111} \mid^2 = \mathbf{4 \mid (f_{Pd} + f_{Fe}) \mid^2}$

Fundamental 200

$F_{200} = f_{Pd} * 1 + f_{Pd} * e^{2\pi i} + f_{Fe} * e^{2\pi i} + f_{Fe} * 1 = 2(f_{Pd} + f_{Fe})$

$I_{200} \propto \mid F_{200} \mid^2 = \mathbf{4 \mid (f_{Pd} + f_{Fe}) \mid^2}$

SL $I_{110} \propto \mid F_{110} \mid^2 = \mathbf{4\eta^2 \mid (f_{Pd} - f_{Fe}) \mid^2}$ < Fundamental $I_{111} \propto \mid F_{111} \mid^2 = \mathbf{4 \mid (f_{Pd} + f_{Fe}) \mid^2}$

Same result can be proven for other superlattice reflections such as 001,112 etc.

Therefore in general $I_{Superlattice} < I_{Fundamental}$

The Long Range Order (LRO) parameter (η) also affects the intensity of the superlattice diffraction peaks.

$\eta = (r_{Fe\ on\ Fe\ sites} - N_{Fe}) / (1 - N_{Fe})$

Where $r_{Fe\ on\ Fe\ sites}$ is the number fraction of Fe atoms that occupy the appropriate lattice sites that can enable the description of the crystal structure as $L1_0$-ordered.

N_{Fe} is the mole fraction of Fe in the solid solution.

For instance if 10% of Fe atoms are not on Fe sites then for equiatomic FePd ($N_{Fe} = N_{Pd} = 0.5$), the Long Range Order parameter

$\eta = (0.9 - 0.5) / (1- 0.5) = 0.8$

Assuming forward scattering (i.e. f = Z) the intensities of the LRO sensitive superlattice peak and the LRO insensitive fundamental peak can be computed.

LRO parameter	I (sl)	I (fund.)	I (sl) / I (fund)
1	1600	20736	0.07716
0.8	1024	20736	0.04938
0.6	576	20736	0.02777
0.4	256	20736	0.01234
0.3	144	20736	0.00694
0.2	64	20736	0.00308
0.1	16	20736	0.00077

The above calculations depict the strong effect of LRO on the ratio I_{SL} / $I_{fundamental}$. The superlattice peaks decrease in intensity as LRO decreases (from being ~ 7.7 % of the fundamental peak at $\eta = 1$ to 0.077 % of the fundamental peak at $\eta = 0.1$).

These calculated changes are in agreement with experimental observations (figure 6.35)

APPENDIX-2

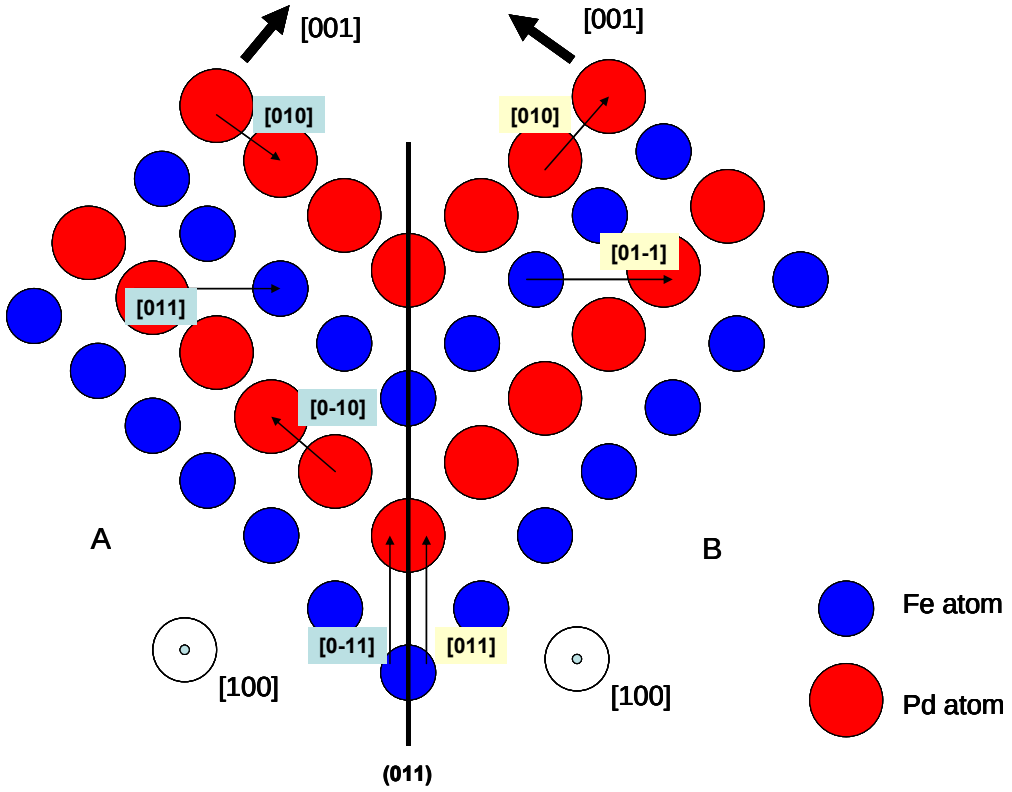

Figure-A2.1 Atomic structure of two layers of the {100} plane for {101} twin.

The examples of crystallographically equivalent directions that can be identified as parallel directions in crystal A and B respectively are

$[100] \parallel^{le} [100]$

$[011] \parallel^{le} [01\text{-}1]$

[001] $\|^{le}$ [010]

[0-10] $\|^{le}$ [001]

Directions in the {101} plane that can be identified as parallel directions are

e.g. [0-11] $\|^{le}$ [011]

A ~ 90° (88°) rotation with [100] as rotation axis can bring both the crystals into correspondence.

APPENDIX-3

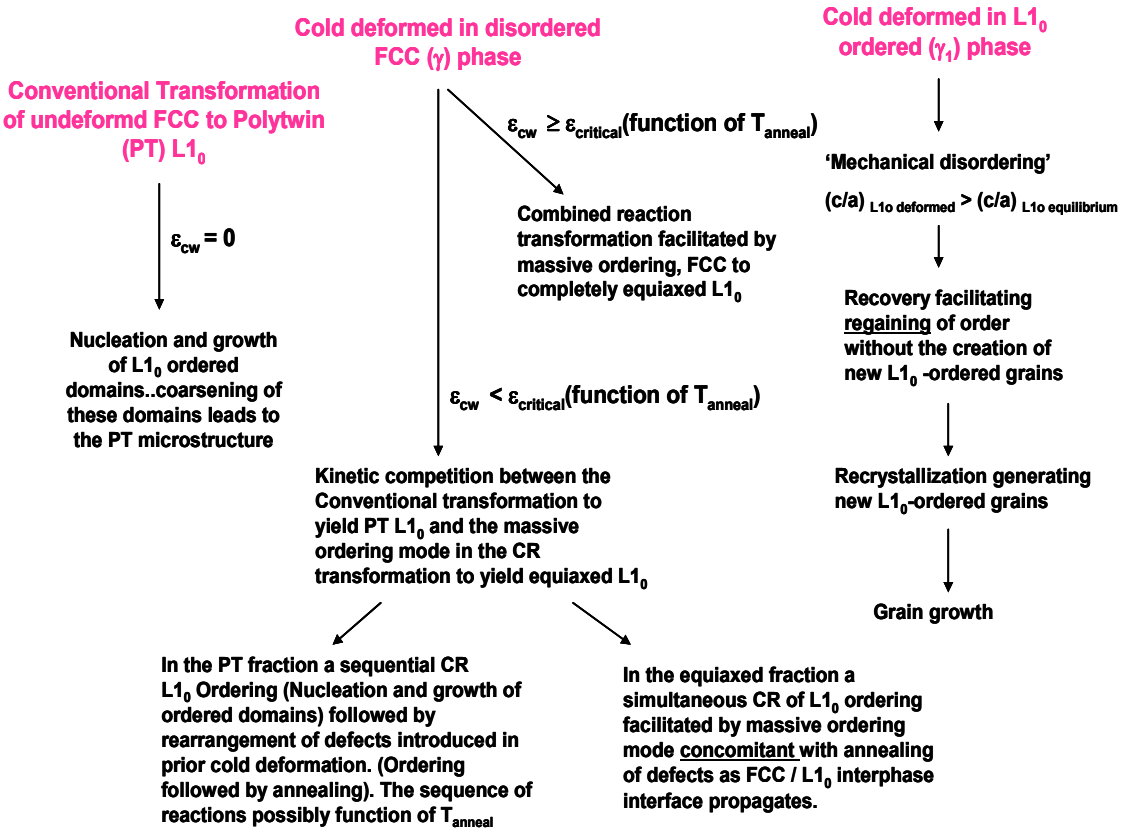

A framework for analyzing the evolution of microstructure during annealing after cold deformation of the equiatomic FePd.

BIBLIOGRAPHY

[1] Cahn,R.W. (1990) in : Recovery, Strain-Age-Hardening and Recrystallization in Deformed Intermetallics, High Temperature Aluminides and Intermetallics, ed. S.H. Whang et al. (TMS: Warrendale, PA), pg 245.

[2] Zhang Bing. (1991) PhD thesis, University of Pittsburgh, pg 23.

[3] Magat, L.M., Yermolenko AS, Ivanova GV, Makarova GM, Shur YAS. (1968) Fiz Metal Metalloved, vol 26,pg 11.

[4] Weller, D., Moser, A. (1999) IEEE Trans Magn, vol 35, pg 4423.

[5] Hornbogen, E. (1979) Met. Trans. vol 10(A), pg 947

[6] Hornbogen, E. (1987) in: 'Phase transformations'87, eds. Lorimer G.W. Inst. of Metals: Univ. of Cambridge. pg 394.

[7] Embury, J.D., Deschamps, A. Brechet, Y. (2003) Scripta Mater. vol 49, pg927.

[8] Burke,J.E., Turnbull, D. (1952) Progress in Metal Physics, vol 3, pg 220.

[9] Humphreys, F.J., Hatherly,M. (1996) in: Recrystallization and Related Annealing Phenomena, 2nd ed. Pergamon, Elsevier Science Ltd. New York, NY.

[10]Reed-Hill, R. E., Abbaschain,R.,(1992) In :Physical Metallurgy Principles, pg 247, PWS Pub. Co. Boston, MA.

[11]Cahn,R.,W., (1996) in: Physical metallurgy vol-3, p2427, edited by - Cahn,R.,W., and Haasen., P. North Holland Pub.Co.New York, NY.

[12]Ferran,G.L., Doherty, R.D., Cahn,R.W. (1971) Acta Metall.vol 19,pg 1019.

[13]Faivre,P., Doherty,R.D (1979), J Mater. Sci. vol 14, pg 897.

[14]Ray,R.K, Hutchinson,B.W., Duggan,B.J. (1975), Acta Metall., vol 23,pg 83.

[15]Ray,R.K., Jonas,J.J., Hook, R.E (1994), Internat. Mater. Rev. 39,pg 129.

[16]Doherty,R.D., (1974), Metal Science, vol 8,pg 132.

[17]Cahn R.W., (1950) Proc. Phys. Soc. vol A63,pg 323.

[18]Hu ,H. (1962) Acta Metall.vol 10,pg 112.

[19]Beck, P.A., Sperry, P.R., (1950) J Appl. Phys. 21,150.

[20]Hutchinson,W.B., Nes,E. (1992), Mater. Sci. Forum vol 94-96,pg 385.

[21]Vandermeer,R.A., (1995) in: 16th RisØ symp., pg 193. eds.N.Hansen et al.

[22]Warrington,D.H., (1979) in: Grain Boundary Structure and Kinetics, ASM Materials Science Seminar, pg 1. eds Balluffi R.W. et al., Milwaukee, WI.

[23]Pond,R.C., (1979) in: Grain Boundary Structure and Kinetics, ASM Materials Science Seminar, pg 13. eds Balluffi R.W. et al., Milwaukee, WI.

[24]Peterson, N.L., (1979) in: Grain Boundary Structure and Kinetics, ASM Materials Science Seminar, pg 209. eds Balluffi R.W. et al., Milwaukee, WI.

[25]Smith,D.A., Rae, C.M.F., Grovenor, C.R.M., (1979) in: Grain Boundary Structure and Kinetics, ASM Materials Science Seminar, pg 337. eds Balluffi R.W. et al., Milwaukee, WI.

[26]Zhang, B., Lelovic, M., Soffa, W.A. (1991) Scr. Metall Mater, vol 25, pg 1577.

[27]Yanar,C., Wiezorek, J.M.K, Soffa, W.A. (2000) in : Phase transformations and evolution of microstructure in materials. Warrendale: TMS pg39.

[28]Khachaturyan, A.G. (1983) in: Theory of Structural Transformations in Solids, pg 369, John Wiley and Sons, New York, NY.

[29]Klemmer, T., Hoydick, D., Okumura, H., Zhang, B., Soffa, W.A. (1995), Scr. Metall Mater. vol 33,pg 1793.

[30]Klemmer, T. (1995) PhD thesis, University of Pittsburgh.

[31]Deshpande, A. R., Al-Ghaferi, A., Xu, H., Heinrich, H., Wiezorek, J.M.K (2003) in : Nanostructural design of advanced materials: A commemorative volume on Prof.G. Thomas' seventieth birthday. London Elsevier; pg 129.

[32]Deshpande, A. R., Wiezorek, J.M.K. (2004), J. Magnetism and Magnetic Mater. vol 270, pg 157.

[33]Porter,D.A., Easterling, K.E., (2001) in :Phase transformations in metals and alloys., pg 305.

[34]Greenberg, B.A., Gornostirev, Yu.N., (1985) Scr. Met. vol 119, pg 1391.

[35]Yang R, Botton, G. A., Cahn, R. W. (1996) Acta Mater.vol 44, pg 3869.

[36]Takasugi, T., Izumi, O., (1985) Acta Met. vol 33, pg 49.

[37]Vidoz, A. E., Lazarevic, D., Cahn, R. W. (1963) Acta Met. vol 11, pg 17.

[38]Greenberg, B. A., Hug, G., Antonova, O. V., Boyarshinova, T. S., Pesina, Z. M., Sachanskaya, I. N., Volkov, A. Yu. (1997) Intermetallics vol 5, pg 297.

[39]Arunachalam, V. S, Cahn, R. W., (1967) J Mater. Sci. vol 2, pg 160.

[40]Kuranov, A. A., Sakhanskaya, I. N., Berseneva, F. N. (1982) Fiz. Metal. Metalloved vol 54, pg 121.

[41]Grokhovskaya, L. G., Greenberg, B. A., Ermakov, A. E., Adrianovskii, B. P. (1988) Fiz. Metal. Metalloved. vol 65, pg 1008.

[42]Buckley R A.(1979) Met. Sci. vol 13,pg 67.

[43]Gushchin, G. M., Kuranov, A. A., Berseneva, F. N. (1983) Fiz. Metal. Metalloved. vol 56, pg 117.

[44]Tanaka, K., Ichitsubo, T., Amano, M., Koiwa, M., Watanabe, K. (2000) Mat Trans, JIM. vol 41, pg 917.

[45]Burgers, W. G. (1957) in : ‘ The Art and Science of Growing Crystals’ eds – Gilman J. John Wiley, NY.

[46]Wilbrandt, P. J. (1992) Scr. Metall. Mater. vol 27, pg 1485.

[47]Haasen, P. (1993) Met. Trans. A, vol 24A,pg 1001.

[48]Dash, S., Brown, N. (1963) Acta Met. vol 11,pg 1067.

[49]Mahajan, S., Pande, C. S., Imam, M. A., Rath, B. B. (1997) Acta Mater. vol 45,pg 2633.

[50]Yanar, C., Radmilovic, V., Soffa, W. A., Wiezorek, J. M. K. (2001) Intermetallics vol 9, pg 949.

[51]Deshpande, A. R. (2004) Masters Thesis, University of Pittsburgh.

[52]Yoo, M. H. (1998) Intermetallics. vol 6, pg 597.

[53]Gao, Yi-qun., Wang Zhong-min, Whang, S. H. (1995) Mat. Sci. and Eng. A vol A192/193, pg 53.

[54]Rao, M., Soffa, W. A. (1997) Scr. Mater.vol 36,pg 735.

[55]Zupan, M., Hemker, K. J.(2003) Acta Mater. vol 51,pg 6277.

[56]Wiezorek, Jorg. M. K. (2003) Intermetallics.vol 11,pg 9.

[57]Xu, Huiping., Wiezorek, J. M. K. (2004) Acta Mater. vol 52, pg 395.

[58]Rao, M. (1997) PhD thesis, University of Pittsburgh.

[59]Borodkina, M. M., Detalf, E. I., Selisskii, Y. D. (1959) Fiz. Metal. Metalloved. vol 7, pg 50.

[60]Davies, R. G., Stoloff, N. S. (1966) Trans. Met. Soc. A.I.M.E. vol 236, pg 1605.

[61]Gottstein, G., Nagpal, P., Kim, W. (1989) Mater. Sci. Eng. vol A108 ,pg 165.

[62]Cahn, R. W., Takeyama, M., Horton, J. A., Liu, C. T. (1991) J. Mater. Res. vol 6, pg 57.

[63]Morris, D. G., Morris, M. A., (1993) Mater. Sci. Forum vol 113-115, pg 599.

[64]Kallend,J.S. in Chapter-3 of 'Texture and Anisotropy - Preferred Orientations in Polycrystals and their Effect on Materials Properties'(1998), pg 114-119, eds – Kocks UF, Tome CN, Wenk HR, Cambridge University Press, Cambridge, U.K.

[65]Goldstein, J.I., Newbury, D.E., Echlin,P., Joy, D.C., Romig, A.D. Jr., Lyman, C.E. Fiori, C. Lifshin, E., (1992) in : Scanning Electron Microscopy and X-ray Microanalysis, pg 91, Plenum Press, New York, NY.

[66]Randle, V., Engler, O. (2003) in : ' Introduction to Texture analysis – Macrotexture, Microtexture & Orientation Mapping' Taylor & Francis ltd. pg50.

[67]Hirsch, J., Lucke, K. (1988) Acta Metall. vol 36, pg 2863 (sections -1 and 2).

[68]Doherty, R.D., Samajdar, I., Kunze, K. (1992) Scr. Metall. Mater. vol 27, pg 1459.

[69]Adams, B.,L. (1993) Mat. Sci. and Eng. A vol A166, pg 59.

[70]Kumar, M., Schwartz, A.J., King, W.E. (2001) Mat. Sci. and Eng. A vol309-310, pg 78.

[71]Fultz, B., Howe, J.M. (2000) in :'Transmission Electron Microscopy and Diffractometry of Materials' pg392, Springer-Verlag, New York, NY.

[72]Yamaguchi,M., Umakoshi, Y. (1990) Progress in Materials Science, vol 34, pg 1.

[73]Jones A.R. (1981) J. Materials Science, vol 16, pg 1374.

[74]Cullity, B.D. (1978) in : 'Elements of X-ray Diffraction', pg 390, Addison-Wesley Publishing Co. Reading, MA.

[75]Kelly, A., Groves, G.W., Kidd, P. (2000) in: 'Crystallography and Crystal Defects', pg 385, John Wiley & Sons Ltd. New York, NY.

[76]Cullity, B.D. (1978) in : 'Elements of X-ray Diffraction', pg 476, Addison-Wesley Publishing Co. Reading, MA.

[77]Ungar, T. (2004) Scr. Mater. vol 51, pg 777.

[78]Dadras, M.M., Morris, D.G. (1993) Scr. Metall. Mater. vol 28, pg 1245.

[79]Ristau, R.A., Barmak, K., Lewis, L.H., Coffey, K.R., Howard, J.K. (1999) J. Appl. Phys. vol 86, pg 4527.

[80]Cullity, B.D. (1978) in : 'Elements of X-ray Diffraction', pg 103, Addison-Wesley Publishing Co. Reading, MA.

[81]Bay, B., Hansen, N., Hughes, D.A., Kuhlmann-Wilsdorf, D. (1992) Acta. Metall. Mater. vol 40, pg 205.

[82]Greenberg, B.A., Sykutkina, V.I., Yakovleva,E.S., (1968) Fiz. Metal. Metalloved. vol 26, pg 17.

[83]Balk, T.J., Hemker, K.J. (2001) Mat. Sci. and Eng A. vol 309-310, pg 108.

[84]Hirsch, P.B., (1962) Phil. Mag. vol 7, pg 67.

[85]Sun,Y.Q., Crimp, M.A., Hazzledine, P.M., Couret, A. (1991b) Phil. Mag. vol 64A,pg.311.

[86]Weertman,J , Weertman, J.R. (1992) in : 'Elementary Dislocation Theory', pg 74, Oxford University Press, Oxford, UK.

[87]Kulovits, A., Soffa, W. A., Puschl, W., Pfieler W. (2003) Materials Research Society Symposium proceedings vol 753, BB5.37.1.

[88]Kulovits, A., Soffa, W. A., Puschl, W., Pfeiler, W. (2002) Proceedings of the Vlll. Seminar, Diffusion and Thermodynamics of Materials, Brno, Czech Republic.

[89]Herzig, C., Divinski, S. (2004) Intermetallics vol 12, pg993.

[90]Meyers, M.A., Murr, L.E. (1978) Acta. Met. vol 26, pg 951.

[91]Al-Ghaferi, A., Mullner, P., Heinrich, H., Kostorz, G., Wiezorek, J.M.K., (2005) Acta mater. in review

[92]Klemmer, T.J., Liu, C., Shukla, N., Wu, X.W., Weller, D., Tanase, M., Laughlin, D.E., Soffa, W.A. (2003) J. Magnetism and Magnetic. Materials. vol 266, pg 79.

[93]Carpenter, H., Tamura, S., (1926) Proc. Royal. Soc. vol A113, pg 161.

[94]Gleiter, H. (1969) Acta. Met. vol 17, pg 1421.

[95]Fullman, R.L., Fisher, J.C. (1951) J. Appl. Phys. vol 22, pg 1350.